

Alma Mater Studiorum Università di Bologna  
Archivio istituzionale della ricerca

Air pollution and meteorology monitoring report (Update). Deliverable 5.2(Update). Project iSCAPE, Grant Agreement number: 689954

This is the submitted version (pre peer-review, preprint) of the following publication:

*Published Version:*

*Availability:*

This version is available at: <https://hdl.handle.net/11585/728750> since: 2020-10-02

*Published:*

DOI: <http://doi.org/>

*Terms of use:*

Some rights reserved. The terms and conditions for the reuse of this version of the manuscript are specified in the publishing policy. For all terms of use and more information see the publisher's website.

This item was downloaded from IRIS Università di Bologna (<https://cris.unibo.it/>).  
When citing, please refer to the published version.

(Article begins on next page)



# Air pollution and meteorology monitoring report (Update)

D5.2

04/2019



*This project has received funding from the European Union's Horizon 2020 research and innovation programme under grant agreement No 689954.*

**Project Acronym and Name**

iSCAPE - Improving the Smart Control of Air Pollution in Europe

<b>Grant Agreement Number</b>	689954	
<b>Document Type</b>	Report	
<b>Document version &amp; WP No.</b>	V0.1	WP5
<b>Document Title</b>	Air pollution and meteorology monitoring report (update)	
<b>Main authors</b>	Silvana Di Sabatino (Lead UNIBO), Erika Brattich (UNIBO), Francesco Barbano (UNIBO), Salem Gharbia (UCD), Francesco Pilla (UCD), Abhijith Kooloth Valappil (UoS), Thor-Bjørn Ottosen (UoS), Sachit Mahajan (UoS), Hamid Omidvarborna (UoS), Prashant Kumar (UoS), Achim Drebs (FMI), Kirsti Jylhä (FMI), Antti Mäkelä (FMI), Olli Saranko (FMI), Luca Torreggiani (ARPA-ER), Carla Barbieri (ARPA-ER)	
<b>Partner in charge</b>	UNIBO	
<b>Contributing partners</b>	UNIBO, ARPA-ER, UCD, UOS, FMI	
<b>Release date</b>	30/04/2019	

The publication reflects the author's views. The European Commission is not liable for any use that may be made of the information contained therein.

Document Control Page	
<b>Short Description</b>	<i>This report is an update of D5.2. Similar to the first version of this report, this updated version documents good quality meteorological and air quality data obtained as result of the experimental field campaigns carried out in the different iSCAPE cities, namely Bologna, Dublin, Guildford and Vantaa. We recall that these cities are those with a focus on “physical” interventions. The data obtained so far were carefully checked for their quality and their usage is twofold. From one hand measured data will be used for the validation of the model simulations run as part of other WPs (e.g. WP4 and WP6) and, on the other hand, they will provide the scientific basis to establish the efficacy of different PCSs including low boundary walls and green infrastructure (trees and hedges), in each city.</i>

Review status	Action	Person	Date
	Quality Check	<i>Coordination Team</i>	
	Internal Review		
Distribution	Public		



Revision history			
Version	Date	Modified by	Comments
V0.1	31/03/2019	Silvana Di Sabatino, Erika Brattich, Francesco Barbano, Salem Gharbia, Francesco Pilla, Abhijith Kooloth Valappil, Thor-Bjørn Ottosen, Sachit Mahajan, Hamid Omidvarborna, Prashant Kumar, Achim Drebs, Kirsti Jylhä, Antti Mäkelä, Olli Saranko, Luca Torreggiani, Carla Barbieri	Complete first draft to be sent for internal revisions
V0.2	20/04/2019	Silvana Di Sabatino, Erika Brattich, Francesco Barbano	Revisions addressing the internal reviewers' comments

**Statement of originality:**

This deliverable contains original unpublished work except where clearly indicated otherwise. Acknowledgement of previously published material and of the work of others has been made through appropriate citation, quotation or both.

# Table of Contents

## Table of Contents

<b>1</b>	<b>Executive Summary</b> .....	<b>- 14 -</b>
<b>2</b>	<b>Introduction</b> .....	<b>- 14 -</b>
<b>3</b>	<b>Methodology for air pollution and meteorology monitoring</b> .....	<b>- 16 -</b>
<b>3.1</b>	<b>Bologna</b> .....	<b>- 17 -</b>
3.1.1	Site description.....	- 17 -
3.1.2	Instrumental setup.....	- 19 -
3.1.3	Experimental protocol and quality check .....	- 20 -
<b>3.2</b>	<b>Lazzaretto</b> .....	<b>- 21 -</b>
3.2.1	Site description.....	- 21 -
3.2.2	Instrumental setup.....	- 22 -
3.2.3	Experimental protocol and quality check .....	- 23 -
<b>3.3</b>	<b>Dublin</b> .....	<b>- 25 -</b>
3.3.1	Site description.....	- 25 -
3.3.2	Instrumental setup.....	- 26 -
3.3.3	Experimental protocol and quality check .....	- 28 -
<b>3.4</b>	<b>Guildford</b> .....	<b>- 28 -</b>
3.4.1	Data processing methods for low-cost sensors .....	- 28 -
3.4.2	Long-term time series measurements on a hedge.....	- 34 -
3.4.3	Field experiments evaluating air pollution reduction of various GI .....	- 35 -
3.4.4	Field investigation of apportionment of deposition and dispersion components of air pollution reduction by GI.....	- 36 -
3.3.3	Quality assurance of citizen sensors .....	- 38 -
<b>3.5</b>	<b>Vantaa</b> .....	<b>- 39 -</b>
3.5.1	Site description.....	- 39 -
3.5.2	Instrumental setup.....	- 41 -
3.5.3	Experimental protocol and quality check .....	- 43 -
<b>4</b>	<b>Environmental impact data</b> .....	<b>- 46 -</b>
<b>4.1</b>	<b>Bologna</b> .....	<b>- 46 -</b>
4.1.1	Boundary Layer Height Analysis .....	- 46 -
4.1.2	Influence of GI on air pollution.....	- 52 -
4.1.3	Vertical mass exchange processes: the Lazzaretto case study .....	- 61 -
<b>4.2</b>	<b>Dublin</b> .....	<b>- 66 -</b>
4.2.1	Meteorology and air pollution: statistical analysis .....	- 66 -
4.2.2	Meteorology and air pollution: preliminary results.....	- 72 -
<b>4.3</b>	<b>Guildford</b> .....	<b>- 76 -</b>
4.3.1	Data processing methods for low-cost sensors .....	- 76 -
4.3.2	Long-term time series measurements on a hedge.....	- 78 -
4.3.3	Field experiments evaluating air pollution reduction of various GI – extended results .....	- 79 -
4.3.4	Field investigation of apportionment of deposition and dispersion components of air pollution reduction by GI.....	- 83 -
4.3.5	Results and observation from citizen sensors quality control measures .....	- 86 -
<b>4.4</b>	<b>Vantaa</b> .....	<b>- 88 -</b>

4.4.1	Meteorological and air quality data .....	- 88 -
<b>5.</b>	<b>Conclusions .....</b>	<b>- 95 -</b>
<b>6.</b>	<b>References / Bibliography .....</b>	<b>- 98 -</b>

## List of Tables

TABLE 1:	OVERVIEW OF THE PCSs EVALUATED, AND OF THE METEOROLOGICAL AND AIR POLLUTION POLLUTANTS VARIABLES MONITORED WITHIN THE MONITORING CAMPAIGNS SETUP IN THE FOUR ISCAPE CITIES.....	- 16 -
TABLE 2:	OVERVIEW OF THE CONTENTS PRESENTED IN THE FIRST AND UPDATE VERSION OF THIS DELIVERABLE FOR THE FOUR ISCAPE CITIES. ....	- 17 -
TABLE 3:	DETAILS ON AIR POLLUTION POLLUTANTS AND TIME RESOLUTION OF THE AIR QUALITY INSTRUMENTATION LOCATED IN THE TWO STREET CANYONS AND AT FIXED AIR POLLUTION MONITORING STATIONS WITHIN THE TWO EXPERIMENTAL BOLOGNA FIELD CAMPAIGNS. ....	- 21 -
TABLE 4:	DESCRIPTIVE STATISTICS (N = NUMBER OF CASES, MEAN, STD = STANDARD DEVIATION, MIN = MINIMUM, MAX = MAXIMUM) FOR NO <sub>x</sub> AND CO POLLUTANT REMOVAL EFFICACY UNDER THE DIFFERENT WIND CONDITIONS IN BOLOGNA, AS MEASURED AT THE BOLOGNA AIRPORT SYNOPTIC METEOROLOGICAL STATION. .	- 56 -
TABLE 5:	DESCRIPTIVE STATISTICS (N = NUMBER OF CASES, MEAN, STD = STANDARD DEVIATION, MIN = MINIMUM, MAX = MAXIMUM) FOR NO <sub>x</sub> , CO AND PM <sub>2.5</sub> POLLUTANT REMOVAL EFFICACY UNDER THE DIFFERENT WIND CONDITIONS IN BOLOGNA, AS MEASURED AT THE BOLOGNA AIRPORT SYNOPTIC METEOROLOGICAL STATION. .	- 58 -
TABLE 6:	ABSOLUTE VALUES OF THE WEIGHTED MASS TRANSPORTS FOR EACH QUADRANT IN CANYON A. ....	- 65 -
TABLE 7:	SUMMARY STATISTICS SHOWING TOTAL AVAILABLE DATA FROM THE FIELD CAMPAIGN. STATISTICAL PARAMETERS SUCH AS MEAN, MEDIAN, STANDARD DEVIATION, MINIMUM AND MAXIMUM POLLUTANT CONCENTRATION ARE TABULATED. ....	- 84 -
TABLE 8:	SUMMARY STATISTICS SHOWING THE STATISTICAL PARAMETERS SUCH AS MEAN, MEDIAN AND STANDARD DEVIATION (SD) FOR PM <sub>1</sub> , PM <sub>2.5</sub> AND PM <sub>10</sub> .....	- 86 -

## LIST OF FIGURES

FIGURE 1:	SCHEMATIC FLOW DIAGRAM OF THE CONNECTIONS BETWEEN THIS REPORT/TASK AND OTHER TASKS IN THE SAME AND IN OTHER ISCAPE WPs. ....	- 15 -
FIGURE 2:	MEASUREMENT SITES FOR AIR POLLUTION AND METEOROLOGICAL VARIABLES WITHIN THE TWO INTENSIVE EXPERIMENTAL FIELD CAMPAIGNS IN BOLOGNA: MARCONI AND LAURA BASSI STREET CANYONS (ASPECT RATIO H/W . = 1.65 AND 0.7, RESPECTIVELY), BOLOGNA URBANA, ASINELLI AND LIPE BOLOGNA AIRPORT METEOROLOGICAL STATIONS; PORTA SAN FELICE AND GIARDINI MARGHERITA ARP AE AIR QUALITY STATIONS; IRNERIO ST., 46 LOCATION OF THE CEILOMETER ON THE ROOFTOP OF THE DEPARTMENT OF PHYSICS AND ASTRONOMY OF THE UNIVERSITY OF BOLOGNA (SOURCE: GOOGLE MAPS). ....	- 18 -
FIGURE 3:	THE VAISALA CEILOMETER CL31 FOR THE MEASUREMENT OF BOUNDARY LAYER HEIGHT IN BOLOGNA CITY CENTER.....	- 20 -
FIGURE 4:	LOCATION OF THE LAZZARETTO AREA AND OTHER MEASUREMENT SITES FOR AIR POLLUTION AND METEOROLOGICAL VARIABLES WITHIN THE INTENSIVE EXPERIMENTAL FIELD CAMPAIGN OF SUMMER 2018: THE TWO STREET CANYONS IN LAZZARETTO AREA (ASPECT RATIO H/W = 1.66 AND 0.89, RESPECTIVELY); BOLOGNA URBANA, ASINELLI AND BOLOGNA AIRPORT (LIPE) METEOROLOGICAL STATIONS; CHIARINI ARP AE AIR QUALITY STATION; IRNERIO ST., 46 WHERE THE CEILOMETER WAS LOCATED (SOURCE: GOOGLE MAPS)...	- 22 -

FIGURE 5: SONIC ANEMOMETER AND LI-COR 7500RS GAS ANALYZER ON THE ROOFTOP OF ONE OF THE TWO CANYONS IN LAZZARETTO AREA. ....	- 24 -
FIGURE 6: (A) EXPERIMENTAL SITE ON PEARSE STREET IN DUBLIN, IRELAND (B) MAP OF THE EXPERIMENTAL MONITORING SITE IN DUBLIN (SOURCE: GOOGLE MAPS).....	- 26 -
FIGURE 7: TELEDYNE CHEMILUMINESCENT NO/NO <sub>2</sub> /NO <sub>x</sub> ANALYZER USED IN DUBLIN EXPERIMENTAL CAMPAIGN. .	- 27 -
FIGURE 8: LEFT FIGURE SHOWS THE RESEARCHER STANDING WITH AM520 TO MEASURE CONCENTRATION IN FRONT OF THE WALL WHILE THE RIGHT FIGURE SHOWS THE DRX8534 STATIONED ON A TRIPOD BEHIND THE WALL.).....	- 28 -
FIGURE 9: STEPS IN THE GENERIC DATA PROCESSING METHODOLOGY. THE GREEN BOXES REPRESENT STEPS INCLUDED IN THE PRESENT STUDY, AND THE GREY BOXES REPRESENT STEPS LEFT FOR FUTURE STUDIES. -	- 29 -
FIGURE 10: AERIAL PHOTO OF THE BUS STOP WHERE THE MEASUREMENTS WERE TAKEN. THE LOCATION OF THE SENSOR IS MARKED WITH A RED DOT. DATA SOURCE: GOOGLE EARTH. FIGURE FROM OTTOSEN AND KUMAR (2019) .....	- 30 -
FIGURE 11: EXAMPLE OF AN ABRUPT CHANGE IN THE SO <sub>2</sub> TIME SERIES IN MAY 2018. ALL DATA IN THE FIGURE CARRY A VALID STATUS TAG. ....	- 31 -
FIGURE 12: EXAMPLE OF AN OUTLIER IN THE CONCENTRATIONS FROM 30 OCTOBER 2017.....	- 32 -
FIGURE 13: OVERVIEW OF THE SAMPLING SITE IN STOKE PARK (TOP), A PHOTO OF THE SENSOR OUTSIDE THE PARK (BOTTOM-LEFT) AND THE SENSOR INSIDE THE PARK (BOTTOM-RIGHT).....	- 34 -
FIGURE 14: TWO MONITORING LOCATIONS ALONG STOKE ROAD, TOP FIGURE SECTION SHOWS HEDGE LOCATION AT STOKE PARK, BOTTOM DISPLAYS CLEAR AREA. RIGHT SECTION SHOWS A PLAN VIEW OF BOTH LOCATIONS.-	- 37 -
FIGURE 15: SCATTERPLOTS OF ONE INSTRUMENTS MEASURING THE SAME POLLUTANT. A) PM <sub>1</sub> MEASUREMENTS BY GRIMM 11-C ON THE X-AXIS AND GRIMM 107 ON THE Y-AXIS, B) PM <sub>2.5</sub> BY GRIMM 11-C ON THE X-AXIS AND GRIMM 107 ON THE Y-AXIS. ....	- 38 -
FIGURE 16: COLOCATION SCENARIO. (A) THE RED DOT ON THE MAP SHOWS THE MEASUREMENT SITE. (B) VIEW OF THE SC KITS COLLOCATED WITH GRIMM. ....	- 39 -
FIGURE 17: THE ISCAPE – VANTAA MONITORING STATIONS ON A MAP: 1 = MALMINIITTY, 2 = HEUREKA, 3 = HELSINKI-VANTAA AIRPORT (METEOROLOGICAL REFERENCE STATION).....	- 40 -
FIGURE 18: AERIAL VIEW OF THE TWO MONITORING STATIONS: MALMINIITTY (LEFT) AND HEUREKA (RIGHT). RED DOTS INDICATE THE LOCATIONS OF THE INSTRUMENTS, GREEN DOT INDICATES THE LOCATION OF THE HSY AIR POLLUTION MONITORING STATION (SOURCE: GOOGLE MAPS).....	- 40 -
FIGURE 19: THE ISCAPE MALMINIITTY MONITORING STATION INSTRUMENTAL SETUP (FROM LEFT TO RIGHT): KIPP&ZONEN, CNR 4 NET-RADIATION METER; VAISALA WEATHER SENSOR WXT536; FMI STANDARD EQUIPMENT FOR AIR TEMPERATURE AND HUMIDITY MEASUREMENTS (ALL PHOTOS BY ACHIM DREBS). ....	- 41 -
FIGURE 20: THE ISCAPE HEUREKA MONITORING STATION INSTRUMENTAL SETUP (FROM LEFT TO RIGHT): FMI STANDARD EQUIPMENT FOR AIR TEMPERATURE AND HUMIDITY MEASUREMENTS; THE FMI MOUNTING TEAM AND ISCAPE RESEARCHERS AT THE TIME OF THE INSTALLATION; THE OBSERVATION MAST WITH THE KIPP&ZONEN, CNR 4 NET-RADIATION METER AND VAISALA WEATHER SENSOR WXT536 AT 10 M HEIGHT (ALL PHOTOS BY ACHIM DREBS).....	- 42 -
FIGURE 21: THE HELSINKI REGION ENVIRONMENTAL SERVICES AUTHORITY (HSY) AIR POLLUTION AND ENVIRONMENTAL MONITORING STATION AT TIKKURILA, 150 METER NORTH OF THE SCIENCE CENTER HEUREKA, ATTENTION: NOT ALL SENSORS WERE MOUNTED AT THE TIME OF THIS PICTURE, SEE ALSO FIGURE 17; (ALL PHOTOS BY ACHIM DREBS, 2015). ....	- 42 -
FIGURE 22: HSY AIR POLLUTION STATION NETWORK. ....	- 43 -
FIGURE 23: ISCAPE MALMINIITTY BUILT-UP AREA, LEFT 2-D MODEL, RIGHT 3-D MODEL, RED DOT: ISCAPE – MONITORING STATIONS (MODELS BY ACHIM DREBS AND ENVI-MET V4). ....	- 43 -
FIGURE 24: ISCAPE HEUREKA OPEN AREA, LEFT 2-D MODEL, RIGHT 3-D MODEL, RED DOT: ISCAPE – MONITORING STATIONS (MODELS BY ACHIM DREBS AND ENVI-MET V4). ....	- 44 -
FIGURE 25: SUMMARY OF THE STATISTICS OF THE 3-DAY HEUREKA SUMMER CAMP QUESTIONNAIRE, 31/07 – 2/8/2018.....	- 45 -
FIGURE 26: HOURLY MEAN TEMPERATURE (TEMP, °C), RELATIVE HUMIDITY (RH, %) AND WIND (M/S) FOR THE HEUREKA CAMPAIGN DAYS JULY 31 (UPPER) AND AUG 2 (LOWER).....	- 46 -
FIGURE 27: DIURNAL CYCLE OF THE PLANETARY BOUNDARY LAYER OVER LAND IN CONDITION OF LARGE-SCALE HIGH PRESSURE (MODIFIED FROM: STULL, 1988). ....	- 47 -

FIGURE 28: STRUCTURE OF THE URBAN BOUNDARY LAYER (SOURCE: 2002, ORIGINALLY OKE ET AL., 1997). .	- 48 -
FIGURE 29: BOUNDARY LAYER HEIGHT RETRIEVED FROM CEILOMETER DATA AT IRNERIO ST. 46. SUMMER DAILY CYCLE, 23/08/2017. ....	- 49 -
FIGURE 30: DIURNAL CYCLE OF BOUNDARY LAYER HEIGHT RETRIEVED FROM CEILOMETER DATA AT IRNERIO ST. 46. WINTER DAILY CYCLE, 31/01/2018. ....	- 50 -
FIGURE 31: DIURNAL CYCLE OF NO <sub>x</sub> HOURLY MEANS CONCENTRATIONS MEASURED IN THE TWO BOLOGNA STREET CANYONS (MARCONI AND LAURA BASSI) AND AT ARPAE URBAN TRAFFIC (PORTA SAN FELICE) AND URBAN BACKGROUND (GIARDINI MARGHERITA) AIR QUALITY STATIONS ON 31/01/2018. ....	- 51 -
FIGURE 32: DIURNAL CYCLE OF ESTIMATED PM (PM <sub>10</sub> AND PM <sub>2.5</sub> ) CONCENTRATIONS DERIVED FROM THE OBSERVATIONS OF THE TWO OPTICAL PARTICLE COUNTERS DEPLOYED AT THE TWO STREET CANYONS DURING THE WINTER 2018 EXPERIMENTAL CAMPAIGN IN BOLOGNA. ....	- 52 -
FIGURE 33: NO <sub>x</sub> AND CO CONCENTRATIONS OBSERVED WITH A 1-MIN TIME RESOLUTION IN THE 2 STREET CANYONS IN BOLOGNA DURING THE INTENSIVE THERMOGRAPHIC SUMMER CAMPAIGN (22-23/08/2017). .	- 53 -
FIGURE 34: 30-MINUTES AVERAGED NO <sub>x</sub> AND CO CONCENTRATIONS IN THE 2 STREET CANYONS IN BOLOGNA DURING THE INTENSIVE THERMOGRAPHIC SUMMER CAMPAIGN (22-23/08/2017).....	- 53 -
FIGURE 35: 1-HOUR AVERAGED NO <sub>x</sub> AND CO NORMALIZED CONCENTRATIONS IN THE 2 STREET CANYONS IN BOLOGNA DURING THE INTENSIVE THERMOGRAPHIC SUMMER CAMPAIGN (22-23/08/2017). ....	- 55 -
FIGURE 36: 30-MIN AVERAGED NO <sub>x</sub> AND CO NORMALIZED CONCENTRATIONS IN THE 2 STREET CANYONS IN BOLOGNA DURING THE 20-26/09/2017 PERIOD OF WEAK SYNOPTIC FORCING WITHIN THE SUMMER 2017 EXPERIMENTAL FIELD CAMPAIGN. ....	- 55 -
FIGURE 37: NO <sub>x</sub> AND CO POLLUTANT REMOVAL EFFICACY CALCULATED AS THE DIFFERENCE IN NORMALIZED 30-MIN AVERAGED NO <sub>x</sub> AND CO NORMALIZED CONCENTRATIONS IN THE 2 STREET CANYONS IN BOLOGNA DURING THE 20-26/09/2017 PERIOD OF WEAK SYNOPTIC FORCING WITHIN THE SUMMER 2017 EXPERIMENTAL FIELD CAMPAIGN. ....	- 56 -
FIGURE 38: POLAR PLOTS SHOWING NO <sub>x</sub> AND CO POLLUTANT REMOVAL EFFICACY, AS OBTAINED FROM THE DIFFERENCE IN THE RATIO BETWEEN NORMALIZED CONCENTRATIONS AT LAURA BASSI AND MARCONI AND NORMALIZED CONCENTRATION IN MARCONI, AS A FUNCTION OF WIND SPEEDS AND DIRECTIONS IN BOLOGNA MEASURED AT THE BOLOGNA AIRPORT METEOROLOGICAL STATION IN THE WEEK OF 19-26/09/2017. ....	- 57 -
FIGURE 39: RELATIONSHIP BETWEEN PM <sub>2.5</sub> REMOVAL EFFICACY AND WIND DIRECTION IN BOLOGNA, AS MEASURED AT THE BOLOGNA SYNOPTIC METEOROLOGICAL STATION. ....	- 58 -
FIGURE 40: POLAR PLOTS SHOWING NO <sub>x</sub> , CO AND PM <sub>2.5</sub> POLLUTANT REMOVAL EFFICACY, AS OBTAINED FROM THE DIFFERENCE IN THE RATIO BETWEEN NORMALIZED CONCENTRATIONS AT LAURA BASSI AND MARCONI AND NORMALIZED CONCENTRATION IN MARCONI, AS A FUNCTION OF WIND SPEEDS AND DIRECTIONS IN BOLOGNA MEASURED AT THE BOLOGNA AIRPORT METEOROLOGICAL STATION DURING THE WINTER THERMOGRAPHIC CAMPAIGN ON 8-9/02/2018. ....	- 59 -
FIGURE 41: TEMPERATURE EVOLUTION WITHIN THE DAY OF THE WINTER INTENSIVE THERMOGRAPHIC CAMPAIGN IN BOLOGNA (08-09/02/2018), MEASURED BY THE THERMO-HYGROMETERS, THE ARPA-ER INSTRUMENTATION IN ONE URBAN (SILVANI ST.) AND ONE RURAL METEOROLOGICAL STATION (MEZZOLARA) AND OF BUILDING FAÇADES OF BUILDINGS LOCATED ON THE WEST AND EAST SIDE OF THE 2 STREET CANYONS (MARCONI ST. ON THE LEFT AND LAURA BASSI ST. ON THE RIGHT) AS RETRIEVED FROM THE THERMAL IMAGES ACQUIRED WITH THE TWO THERMAL CAMERAS. ....	- 60 -
FIGURE 42: THERMAL COMPOSITE MODIS TERRA 21 KM SATELLITE IMAGES FOR 08/02/2018 AT 20:20 (LEFT) AND 22:00 UTC (RIGHT) (IMAGES COURTESY OF THE NASA LEVEL-1 AND ATMOSPHERE ARCHIVE & DISTRIBUTION SYSTEM (LAADS) DISTRIBUTED ACTIVE ARCHIVE CENTER (DAAC), GODDARD SPACE FLIGHT CENTER, GREENBELT, MD). ....	- 61 -
FIGURE 43: KINEMATIC CO <sub>2</sub> (LEFT) AND H <sub>2</sub> O (RIGHT) FLUXES FOR THE WHOLE PERIOD SELECTED FOR ANALYSIS (04-06/08/2018) DURING THE LAZZARETTO SUMMER 2018 CAMPAIGN. DATA ARE 5-MINUTES AVERAGED. .	- 62 -
FIGURE 44: SCHEME OF THE QUADRANT ANALYSIS APPLIED TO THE MASS TRANSPORT. C' STANDS FOR A GENERIC POLLUTANT CONCENTRATION (SOURCE: DI BERNARDINO ET AL., 2018).....	- 63 -
FIGURE 45: QUADRANT ANALYSIS APPLIED TO THE LONGITUDINAL WIND DIRECTIONS. VERTICAL VELOCITY FLUCTUATIONS AS A FUNCTION OF CO <sub>2</sub> CONCENTRATION FLUCTUATIONS. ....	- 64 -
FIGURE 46: QUADRANT ANALYSIS APPLIED TO THE PERPENDICULAR WIND DIRECTIONS. VERTICAL VELOCITY FLUCTUATIONS AS A FUNCTION OF CO <sub>2</sub> CONCENTRATION FLUCTUATIONS. ....	- 64 -
FIGURE 47: DISTRIBUTION PLOT OF WIND SPEED DATA ACCORDING TO THE DIFFERENT WIND DIRECTION CATEGORIES. ....	- 67 -

FIGURE 48: WIND ROSE PLOT FOR THE DUBLIN SITE. ....	- 67 -
FIGURE 49: MINIMUM, MAXIMUM AND AVERAGE WIND SPEED DATA. ....	- 68 -
FIGURE 50: DISTRIBUTION PLOT OF NO <sub>x</sub> (PPB) IN FRONT (F) OF THE LBW. ....	- 69 -
FIGURE 51: DISTRIBUTION PLOT OF NO <sub>x</sub> (PPB) BEHIND (B) THE LBW. ....	- 69 -
FIGURE 52: TIME SERIES PLOT FOR THE NO <sub>x</sub> CONCENTRATIONS (PPB) RECORDED ON BOTH SIDES OF THE LBW....	- 70 -
FIGURE 53: (A) HISTOGRAM REPRESENTING THE FREQUENCY OF DIFFERENT PERCENTAGE CHANGE FOR PM <sub>2.5</sub> IN PRESENCE OF LBW (B)HISTOGRAM REPRESENTING THE FREQUENCY OF DIFFERENT PERCENTAGE CHANGE FOR PM <sub>2.5</sub> IN ABSENCE OF LBW (C) HISTOGRAM REPRESENTING THE FREQUENCY OF DIFFERENT PERCENTAGE CHANGE FOR PM <sub>10</sub> IN PRESENCE OF LBW (D)HISTOGRAM REPRESENTING THE FREQUENCY OF DIFFERENT PERCENTAGE CHANGE FOR PM <sub>10</sub> IN ABSENCE OF LBW. ....	- 71 -
FIGURE 54: NO <sub>x</sub> CONCENTRATION (PPB) IN (F) & (B) OF THE LBW PER WIND DIRECTION. ....	- 72 -
FIGURE 55: MEDIAN NO <sub>x</sub> (PPB) REDUCTION BEHIND LBW. ....	- 73 -
FIGURE 56: STANDARD DEVIATION OF NO <sub>x</sub> (PPB) REDUCTION BEHIND LBW. ....	- 74 -
FIGURE 57: RELATIVE CONCENTRATION OF PM <sub>10</sub> IN FRONT AND BACK OF THE WALL IN THE PRESENCE OF THE LBW. ....	- 75 -
FIGURE 58: RELATIVE CONCENTRATION OF PM <sub>10</sub> IN FRONT AND BACK OF THE WALL IN THE ABSENCE OF THE LBW. ....	- 75 -
FIGURE 59: STACKED BAR CHART OF THE STATUS TAG FOR THE SO <sub>2</sub> CONCENTRATION MEASUREMENTS AS A FUNCTION OF CONCENTRATIONS. THE TWO NUMBERS UNDER EACH BAR REPRESENT THE INTERVAL. THE INTERVALS ARE CHOSEN TO HIGHLIGHT THE INTERVAL COVERED BY DATA WITH A VALID STATUS TAG. ....	- 76 -
FIGURE 60: A SHORT SECTION OF THE AQMESH TIME SERIES FOR NO. OUTLIERS ARE DETECTED USING THE K-NN METHOD. ....	- 77 -
FIGURE 61: A SHORT SECTION OF THE AQMESH TIME SERIES FOR NO. OUTLIERS ARE DETECTED USING THE ARIMA METHOD. THE BLUE POINTS REPRESENT THE ARIMA MODEL FITTED TO DATA. ....	- 77 -
FIGURE 62: EXAMPLE OF A GAP IN THE TIME SERIES BEING FILLED BY THE THREE UNIVARIATE METHODS IN THE PRESENT STUDY. ....	- 78 -
FIGURE 63: PM <sub>2.5</sub> FROM RESPECTIVELY THE SENSOR OUTSIDE THE PARK AND THE SENSOR INSIDE THE PARK. THE HORIZONTAL “STRIPES” ARE CAUSED BY THE MEASUREMENTS BEING ROUNDED TO INTEGER VALUES BY THE SENSOR. ....	- 78 -
FIGURE 64: THE PERCENTAGE DIFFERENCES IN VARIOUS POLLUTANTS UNDER ALONG-ROAD, CROSS-ROAD AND CROSS-VEGETATION WIND CONDITIONS. THE POSITIVE AND NEGATIVE DIFFERENCES INDICATED REDUCED AND INCREASED CONCENTRATIONS BEHIND THE GI AT THE CLOSE- AND AWAY-ROAD SITES (ABHIJITH AND KUMAR, 2019). ....	- 80 -
FIGURE 65: THE FRACTION OF VARIOUS PM TYPES AT ALL THE SIX SITES UNDER DIFFERENT WIND DIRECTIONS. THE INNER CIRCLE SHOWS PM FRACTIONS BEHIND THE GI; THE OUTER CIRCLE SHOWS PM FRACTIONS IN-FRONT/CLEAR AREAS. BLUE, ORANGE AND GREY COLOURS DENOTE PM <sub>1</sub> , PM <sub>1-2.5</sub> AND PM <sub>2.5-10</sub> , RESPECTIVELY. LINE SHADING REPRESENTS A LACK OF DATA AVAILABLE IN PARTICULAR SITUATIONS (ABHIJITH AND KUMAR, 2019). ....	- 82 -
FIGURE 66: PERCENTAGE OF SAMPLES IDENTIFIED IN EACH ELEMENTAL COMPOSITION GROUP IN TOTAL PARTICLES ON THE PTFE FILTERS (A) BEHIND, AND (B) IN-FRONT/CLEAR OF GI (ABHIJITH AND KUMAR, 2019). ....	- 83 -
FIGURE 67: BOXPLOTS OF PM CONCENTRATION BEHIND (RED) AND IN FRONT (GREEN) MEASUREMENT POINTS AT GI SITE AND CLEAR AREA. PM <sub>10</sub> , PM <sub>2.5</sub> AND PM <sub>1</sub> ARE SHOWN FROM LEFT TO RIGHT. CLR AND GI DENOTE CLEAR AREA AND GI SITES, RESPECTIVELY. ....	- 84 -
FIGURE 68: PERCENTAGE CHANGE IN CONCENTRATION OF PM AT BEHIND MEASUREMENT POINT COMPARED TO THAT OF IN FRONT, AT CLEAR AREA AND GI SITE $\{[PM_{INF}-PM_{BHD}] \times 100 / PM_{INF}\}$ . ....	- 85 -
FIGURE 69: THE RATIOS OF (LEFT) PM <sub>1</sub> /PM <sub>2.5</sub> AND (RIGHT) PM <sub>2.5</sub> /PM <sub>10</sub> AT THE STUDIED GI AND CLEAR AREA SITES. ....	- 86 -
FIGURE 70: CORRELATION PLOT BETWEEN THE GRIMM AND TEN SC KITS FOR PM <sub>2.5</sub> MEASUREMENT. ....	- 87 -
FIGURE 71: CORRELATION PLOT BETWEEN THE GRIMM AND TEN SC KITS FOR (A) PM <sub>1</sub> MEASUREMENT AND (B) PM <sub>10</sub> MEASUREMENT ....	- 87 -
FIGURE 72: PLOT SHOWING PM <sub>2.5</sub> MEASUREMENT BY THE GRIMM AND TEN SC KITS. ALMOST SIMILAR TRENDS IN THE PM <sub>2.5</sub> LEVEL FLUCTUATIONS CAN BE OBSERVED FROM THE FIGURE. ....	- 88 -
FIGURE 73: COMPARISON OF DAILY AIR TEMPERATURE AVERAGES (T), HIGHEST AIR TEMPERATURES (TMAX), AND LOWEST AIR TEMPERATURES (TMIN) OF THE STATIONS MALMINIITY, HEUREKA, AND HELSINKI-VANTAA AIRPORT (AIRPORT) FOR THE PERIOD JULY 14TH - 26TH 2018. ....	- 89 -

FIGURE 74: 1-MINUTE AVERAGE OF SOLAR INCOMING SHORTWAVE RADIATION (BLUE) AND REFLECTED SHORTWAVE RADIATION (RED) AT iSCAPE MONITORING STATION MALMINIITTY (LEFT) AND HEUREKA (RIGHT) FOR THE PERIOD JULY 14TH - 26TH 2018. ....	- 89 -
FIGURE 75: MEAN WIND SPEED (LEFT) AND DAILY MAXIMUM WIND SPEED (RIGHT) AT iSCAPE MONITORING STATION MALMINIITTY (BLUE) AND HEUREKA (RED) FOR THE PERIOD MAY 1ST - JULY 26 <sup>TH</sup> 2018. ....	- 90 -
FIGURE 76: RESULTS FROM THE HSY AIR POLLUTION NETWORK MONITORING STATIONS, LEFT: WEEKLY PM <sub>2.5</sub> MEASUREMENTS FROM 12 AIR POLLUTION STATIONS (HSY AND LOHJA), JULY 16TH - 22ND 2018; RIGHT: DETAIL OF 24-HOUR PM <sub>2.5</sub> MEASUREMENTS FROM 7 STATIONS IN THE METROPOLITAN AREA, JULY, 25TH 2018 (SOURCE: HSY). ....	- 90 -
FIGURE 77: RESULTS FROM THE HSY AIR POLLUTION NETWORK MONITORING, LEFT: WEEKLY NITROGEN DIOXIDE MEASUREMENTS FROM 12 AIR POLLUTION STATIONS (HSY AND LOHJA), JULY 16TH - 22ND 2018; RIGHT: DETAIL OF 24-HOUR NITROGEN DIOXIDE MEASUREMENTS FROM 8 STATIONS IN THE LARGER METROPOLITAN AREA, JULY 25TH 2018 (SOURCE: HSY). ....	- 91 -
FIGURE 78: HOURLY NO <sub>2</sub> AND PM <sub>2.5</sub> CONCENTRATIONS IN VANTAA (CITY CENTER, UPPERMOST; RURAL, LOWERMOST) AND IN THE CENTER OF HELSINKI (MIDDLE) IN THE PERIOD 01/01-31/12/2018. ....	- 92 -
FIGURE 79: THE MONTHLY MEAN NO <sub>2</sub> (UPPER) AND PM <sub>2.5</sub> CONCENTRATIONS IN VANTAA AND HELSINKI IN 2018....	- 93 -
FIGURE 80: THE MEAN HOURLY NO <sub>2</sub> (UPPER) AND PM <sub>2.5</sub> (LOWER) CONCENTRATIONS IN VANTAA AND HELSINKI IN 2018. ....	- 94 -
FIGURE 81: HOURLY DISTRIBUTION OF NO <sub>2</sub> AND PM <sub>2.5</sub> CONCENTRATIONS AND 2M-TEMPERATURE IN THE VANTAA CENTRE ON 22 FEB 2018. THIS DAY PRESENTED THE HIGHEST HOURLY NO <sub>2</sub> AND PM <sub>2.5</sub> CONCENTRATIONS IN 2018. LOCAL TIME IS UTC+2 IN WINTER. ....	- 94 -
FIGURE 82: HOURLY CONCENTRATIONS OF NO <sub>2</sub> AND PM <sub>2.5</sub> IN 2018 WITH RESPECT TO 2M-TEMPERATURE (UPPER ROW) AND WIND SPEED (LOWER ROW). ....	- 95 -

## List of abbreviations

ACI:	Automobile Club d'Italia
ARIMA:	AutoRegressive Integrated Moving Average
ARPAE:	Agenzia Regionale per la Prevenzione, l'Ambiente e l'Energia dell'Emilia-Romagna
B:	Backside
BC:	Black-Carbon
BHD:	BeHinD
BTEX:	Benzene, Toluene, Ethylbenzene and Xylenes
CBL:	Convective Boundary Layer
CFD:	Computational Fluid Dynamics
CO:	Carbon Monoxide
CO <sub>2</sub> :	Carbon Dioxide
D:	Deliverable
DAAC:	Distributed Active Archive Center
EEA:	European Environment Agency
EMEP:	European Monitoring and Evaluation Programme
F:	Front Side
FIR:	Far Infrared Radiation
FMI:	Finnish Meteorological Institute
GI:	Green Infrastructure
H <sub>2</sub> O:	Water Vapor
H <sub>CB</sub> :	Hedge only in clear vs behind
H <sub>IB</sub> :	Hedge only in clear vs in-front
HSY:	Helsinki Region Environmental Services Authority
IAAC:	Institute of Advanced Architecture of Catalunya
INF:	IN Front
ISL:	Inertial Sublayer
k-NN:	k-Nearest Neighbor
LAADS:	Level-1 and Atmosphere Archive & Distribution System
LAI:	Leaf Area Index
LBW:	Low Boundary Wall



Lidar:	Light Detection And Ranging
NASA:	National Aeronautics and Space Administration
NN:	Neural Networks
NO:	Nitric Oxide
NO <sub>2</sub> :	Nitrogen Dioxide
NO <sub>x</sub> :	Nitrogen Oxides
NOAA:	National Oceanic and Atmospheric Administration
O <sub>3</sub> :	Ozone
ONA:	Optimised Noise-reduction Averaging
PBL:	Planetary Boundary Layer
PCS:	Passive Control System
PELT:	Pruned Exact Linear Time
PM:	Particulate Matter
PM <sub>1</sub> :	Particulate Matter with aerodynamic diameter less or equal to 1 µm
PM <sub>2.5</sub> :	Particulate Matter with aerodynamic diameter less or equal to 2.5 µm
PM <sub>10</sub> :	Particulate Matter with aerodynamic diameter less or equal to 10 µm
PNC:	Particle Number Concentration
RL:	Residual Layer
RSL:	Roughness Sublayer
SBL:	Stable Boundary Layer
SC:	Smart Citizen
SEM:	Scanning Electron Microscope
SL:	Surface Layer
SO <sub>2</sub> :	Sulphur Dioxide
T:	Task
T <sub>CB</sub> :	Tree only in clear vs behind
T <sub>IB</sub> :	Tree only in clear vs in-front
TH <sub>CB</sub> :	Tree with Hedge case in clear vs behind
TH <sub>IB</sub> :	Tree with Hedge case in clear vs in-front
TPER:	Trasporto Passeggeri Emilia-Romagna
UBL:	Urban Boundary Layer
UCL:	Urban Canopy Layer

WP:        Work Package

# 1 Executive Summary

This is the updated version of D5.2, whose aim is to document good quality meteorological and air pollution data obtained in the various experimental field campaigns carried out in the different iSCAPE cities, namely Bologna, Dublin, Guildford and Vantaa. Experimental field campaigns were setup and carried out in those iSCAPE cities with a specific focus on the evaluation of the impacts on Passive Control Systems (PCSs) on the mitigation of air pollution and the enhancement of urban thermal comfort (i.e., Bologna in Italy, Dublin in Ireland, Guildford in United Kingdom and Vantaa in Finland), while the other two iSCAPE cities (Bottrop in Germany and Hasselt in Belgium) focused instead on infrastructural and behavioral interventions only, and no dedicated experimental field campaign was setup within the iSCAPE project.

As mentioned in the first version of this Deliverable, the campaigns were ad-hoc setup with two preliminary purposes:

1. To provide the scientific basis to evaluate the impact of different PCSs and other meteorological factors on air pollution in each city;
2. To gather data useful to verify the model simulations run as part of other WPs (e.g., WP4 and WP6) with the aim of evaluating the impact of infrastructural and behavioral interventions at larger scales (neighborhood and urban).

Similar to the first version of this report, before presenting the specific results obtained in each city, the updated version presents the instrumental setup and methodologies adopted in the various field campaigns, summarizing and updating those previously presented in D3.3 (*'Report on footprint of PCSs'*) and in the first version of this Deliverable.

Notwithstanding the difference in the experimental setups adopted in the various experimental campaigns, a common general result obtained is the strong dependency of the impact of the different PCSs on the local morphology of the analyzed urban environment and on the local meteorological conditions, among which in particular wind direction plays a dominant role, leading potentially to both mitigation and deterioration effects of air pollution. In addition, in Guildford colocation experiments of low-cost sensors with reference instrumentation were carried out to develop algorithms to analyze the data from low-cost sensors and to investigate the performance of low-cost sensors.

## 2 Introduction

Numerous human health studies have linked air pollution exposure with adverse health effects (Bell et al., 2013; Shang et al., 2013; Beelen et al., 2014; Wang et al., 2014).

Within the iSCAPE project, mitigations of air pollution and climate change impacts are achieved with real-world physical interventions on the urban tissue to alter ventilation rates and dispersion patterns in the selected cities, namely Bologna in Italy, Dublin in Ireland, Guildford in United Kingdom and Vantaa in Finland. In order to monitor air pollution and meteorological levels in the selected iSCAPE cities, numerous experimental field campaigns were setup and carried out within the project lifetime. As such, the aim of the campaigns is twofold: while on one hand they provide experimental data to be used for the calibration and validation of the simulations conducted at larger spatial and temporal scales as part of WP4 and WP6, they also give the possibility to

---

<sup>1</sup> The report is available on the [iSCAPE results webpage](#).

evaluate the potential of different PCSs, including low boundary walls (Dublin), photocatalytic coatings (Lazzaretto site in the outskirts of Bologna) and various forms of green infrastructure (Bologna, Guildford and Vantaa).

This report is the updated version of D5.2, which, as output of Task 5.2, involves the monitoring of the interventions deployed as part of WP3 and WP4 in order to optimize them. As such, this report contains the new results obtained in the monitoring campaigns after the submission of the first version of the Deliverable. In particular, both stationary and mobile stations monitoring stations installed as part of WP3 and WP5 collected environmental data to be used as input and feedback for the simulations run as part of WP4 and WP6. Figure 1 presents an overview of all the activities interconnected with the present report/task, in the same WP as well as in other iSCAPE WPs.

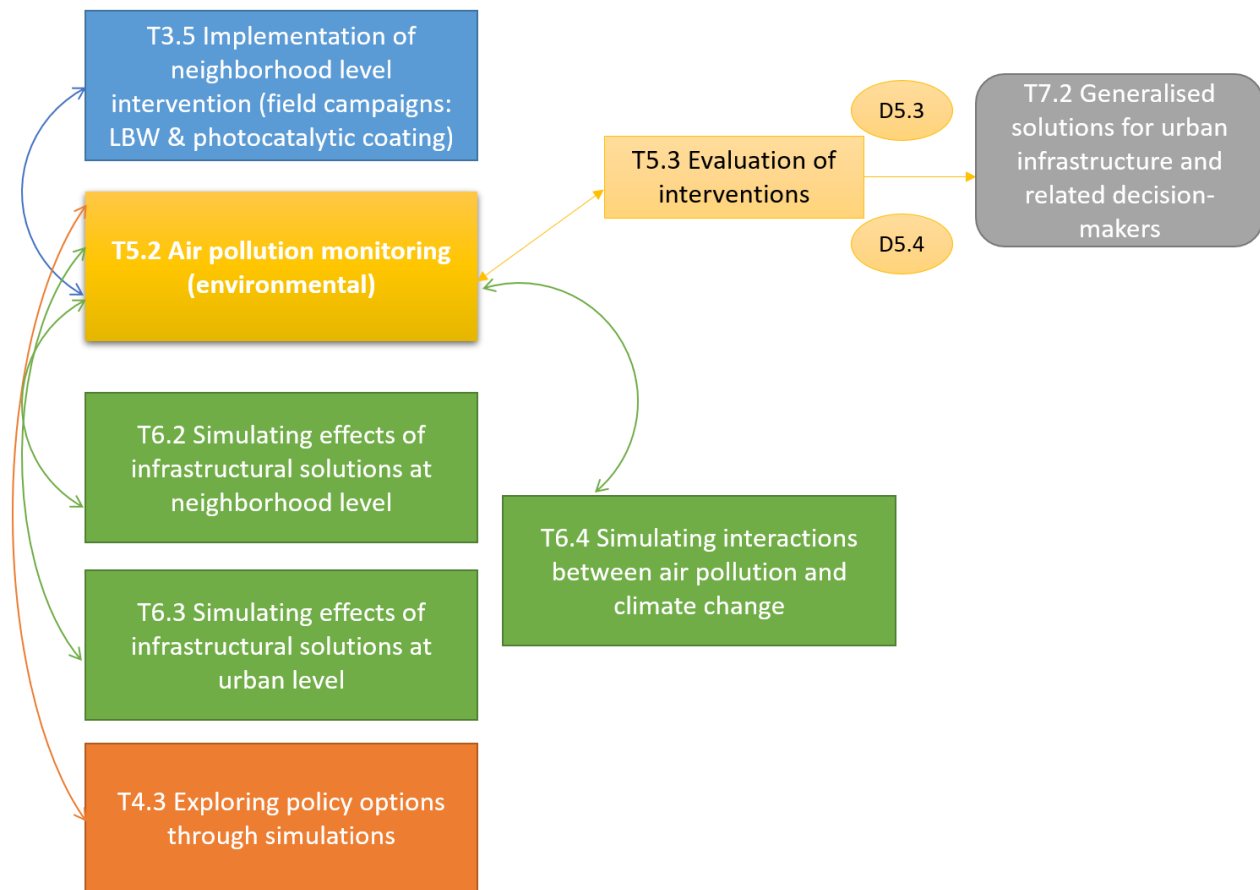


Figure 1: Schematic flow diagram of the connections between this report/task and other tasks in the same and in other iSCAPE WPs.

As such, as the first version, this report intends to document good quality meteorological and air pollution data obtained so far at the monitoring stations set in the different iSCAPE cities. In addition, new results obtained about the efficacy of various PCSs in contrasting air pollution and improving urban thermal comfort are also presented. The structure of the report is as follows: first, the methodology, instrumental setup and experimental protocol adopted within the different monitoring stations is described in Section 3; Section 4 presents the environmental data collected within the experimental campaigns at the 4 pilots. Finally, the main conclusions of this work are drawn.

### 3 Methodology for air pollution and meteorology monitoring

This section is dedicated to the description of the methodologies adopted within the experimental field campaigns conducted in the iSCAPE cities. With respect to the first version of this Deliverable, here the methodology and instrumental setup are summarized, in order to highlight more clearly the relevant updates and changes with respect to the first version of this Deliverable.

Table 1 presents an overview of the PCSs evaluated within the different monitoring campaigns, and of the collected meteorological and air pollution pollutants at the four iSCAPE cities. The campaigns and the results obtained are thoroughly described in this Deliverable (first and second updated version) and in D3.8 (*'Report on neighborhood level interventions'*) as concerns the photocatalytic coatings campaign conducted at Lazzaretto site in the outskirts of Bologna.

City	PCSs	Meteorological variables	Air pollutants
<b>Bologna</b>	Green infrastructure	wind speed, wind direction, high-frequency 3-d wind field (including turbulence), air temperature, relative air humidity, four-energy radiation components, atmospheric pressure	NO <sub>x</sub> , NO, NO <sub>2</sub> , CO, SO <sub>2</sub> , O <sub>3</sub> , PM <sub>10</sub> , PM <sub>2.5</sub> , BTEX, CO <sub>2</sub> and H <sub>2</sub> O fluxes; PNC and BC (only during the winter campaign),
<b>Lazzaretto (Bologna)</b>	Photocatalytic coating	wind speed, wind direction, high-frequency 3-d wind field (including turbulence), air temperature, relative air humidity, four-energy radiation components, atmospheric pressure	NO <sub>x</sub> , NO, NO <sub>2</sub> , CO, SO <sub>2</sub> , O <sub>3</sub> , PM <sub>10</sub> , PM <sub>2.5</sub> , BTEX, CO <sub>2</sub> and H <sub>2</sub> O fluxes
<b>Dublin</b>	Low Boundary Walls	wind speed, wind direction	NO <sub>x</sub> , NO, NO <sub>2</sub>
<b>Guildford</b>	Green infrastructure	air temperature, relative air humidity, wind speed, wind direction	PM <sub>1</sub> , PM <sub>2.5</sub> , PM <sub>10</sub> , PNC, BC, CO, NO, NO <sub>2</sub> , CO, O <sub>3</sub> , SO <sub>2</sub> , chemical characterization of PM particles sampled with optical particle counters
<b>Vantaa</b>	Green infrastructure embedded on high stores buildings	wind speed, wind direction, air temperature, relative air humidity, four-energy radiation components, atmospheric pressure, rain intensity	NO <sub>x</sub> , NO, NO <sub>2</sub> , PM <sub>2.5</sub>

Table 1: Overview of the PCSs evaluated, and of the meteorological and air pollution pollutants variables monitored within the monitoring campaigns setup in the four iSCAPE cities.

Specifically, Table 2 contains an overview of the contents of the first and of this version of this Deliverable for the four iSCAPE cities.

City	1 <sup>st</sup> version	Update version
<b>Bologna</b>	Overview of meteorological, turbulence and air quality data collected within 2 experimental campaigns; UHI effect at neighborhood level and effect of GI on urban thermal comfort; Diurnal pattern of pollutant concentrations	Analysis of boundary layer height and connection with pollutant concentrations; Influence of GI on air pollution and dependence on wind direction
<b>Lazzaletto</b>	/	Vertical air mass exchange processes in street canyons and their dependence on wind direction
<b>Dublin</b>	Statistical analysis of meteorology and effect of LBW on NO <sub>x</sub> concentrations (phase I campaign); dependence of NO <sub>x</sub> concentrations on wind direction	Statistical analysis of meteorology and effect of LBW on PM concentrations (phase II campaign); dependence of PM concentrations on wind direction
<b>Guildford</b>	Effect of different hedge and hedge-tree configurations on air quality; influence of wind direction on concentrations	Algorithms to analyse data from low-cost sensors; elemental composition of individual particles behind and clear/in-front of GI; Apportionment of deposition and dispersion components of air pollution reduction by GI
<b>Vantaa</b>	Preliminary analysis of meteorology and air quality data at two monitoring stations	Investigation of the effect of meteorology on pollutant concentrations

Table 2. Overview of the contents presented in the first and update version of this Deliverable for the four iSCAPE cities.

## 3.1 Bologna

Due to its location in the Po Valley in Southern Europe, Bologna is located in a well-known hotspot in terms of air pollution and climate change. Within the iSCAPE project, the pilot in Bologna is aimed to analyze the effectiveness of GI (Green Infrastructure) in contrasting and those two issues. The monitoring of the effect of GI on air pollution and urban thermal comfort was carried out within two intensive experimental field campaigns in two different urban areas, thoroughly described in the first version of this Deliverable, summarized in the following. Data gathered within the two experimental campaigns, besides being used for the evaluation of turbulence, meteorology and air pollution in real urban street canyons, were also used for the verification of simulations conducted in WP4 (D4.5 ‘*Report on policy options for AQ and CC*’) and WP6 (D6.2 ‘*Microscale CFD evaluation of PCS impacts on air quality*’ & D6.3 ‘*Detailed report on numerical simulations of the effect of PCSs at the urban level*’).

### 3.1.1 Site description

In Bologna, air pollution and meteorological variables were monitored within two intensive experimental field campaigns, one in summer 2017 (10/08-24/09/2017) and one winter 2018 (16/01-14/02/2018), in two parallel urban street canyons, Marconi and Laura Bassi Sts. (Figure 2).



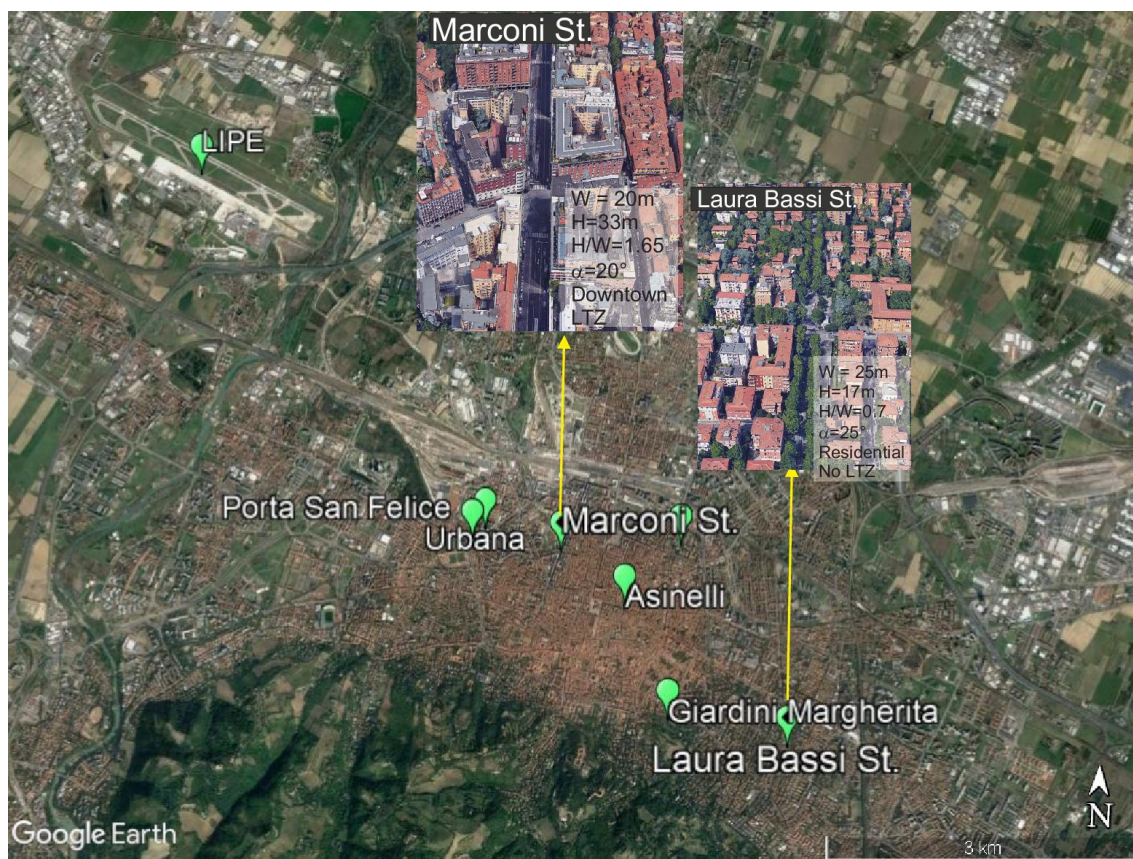


Figure 2: Measurement sites for air pollution and meteorological variables within the two intensive experimental field campaigns in Bologna: Marconi and Laura Bassi street canyons (aspect ratio  $H/W = 1.65$  and  $0.7$ , respectively), Bologna Urbana, Asinelli and LIPE Bologna airport meteorological stations; Porta San Felice and Giardini Margherita ARPAE air quality stations; Innerio St., 46 location of the ceilometer on the rooftop of the Department of Physics and Astronomy of the University of Bologna (source: Google Maps).

As detailed in the first version of this Deliverable, apart from high-time resolution good quality air pollution and meteorological measurements in the two street canyons, observations taken at other ARPAE (Emilia Romagna Environmental Protection Agency, Agenzia Regionale per la prevenzione, l'ambiente, e l'energia dell'Emilia-Romagna; new acronym for ARPA-ER) air pollution (Porta San Felice urban traffic and Giardini Margherita urban background air quality stations) and meteorological stations located in the city of Bologna ("Urbana" urban meteorological station and Bologna airport "LIPE" and Torre Asinelli synoptic meteorological stations) were also used to better evaluate the local observations in the two street canyons. In addition, a Lidar (light detection and ranging) ceilometer was also installed at Innerio St., 46, on the rooftop of the Department of Physics and Astronomy, with the aim to analyze the boundary-layer height in the city.

Briefly, the two street canyons are characterized by a similar N-S configuration and similar traffic volumes, but a major difference in the presence of vegetation: in particular, while Marconi is an almost tree-free urban street canyon located in the city center, Laura Bassi St. is an urban street canyon located in a residential area in the outskirts of Bologna, characterized by the presence of a line of deciduous trees on both sides of the street.

### 3.1.2 Instrumental setup

The instrumental setup adopted within the two Bologna intensive experimental field campaigns is thoroughly described in the first version of this Deliverable. Briefly, two ARPAE mobile laboratories equipped for air pollution and meteorological measurements were deployed in each of the two street canyons.

The two mobile laboratories were equipped for continuous 1-minute measurements of air pollutants such as nitrogen oxides ( $\text{NO}_x$ ,  $\text{NO}_2$  and  $\text{NO}$ ), carbon monoxide ( $\text{CO}$ ), sulphur dioxide ( $\text{SO}_2$ ), ozone ( $\text{O}_3$ ), and daily averages of  $\text{PM}_{10}$  and  $\text{PM}_{2.5}$ . The mobile laboratory located in Marconi St. was further equipped for the measurements of hourly averages of BTEX (Benzene, Toluene, Ethylbenzene, and Xylenes).

During the winter experimental campaign, ARPAE air pollution measurements were complemented with two further instruments (Met One Model 212 Ambient Particulate Counters and AethLabs microAeth AE51) for the high-time resolution measurement of particles' size distribution and of black carbon (BC; soot, or optically-absorbing component of aerosols) concentrations were also deployed in the two street canyons.

ARPAE mobile laboratories were also equipped for measuring basic meteorological variables such as: cup anemometer and wind vane for measuring wind speed and direction; barometer for measuring atmospheric pressure; thermohygrometers for measuring air temperature and relative humidity.

Those meteorological measurements were further complemented with: GILL Windmaster sonic anemometers for accurate and fast measurements of the 3-d wind field and for estimating a range of turbulence parameters and fluxes using eddy covariance methods; HCS2S3 Rotronic temperature and relative humidity probes for measuring accurately air temperature and humidity; Vaisala Barometer PTB110 for accurate barometric pressure measurements at room temperature and for general environmental pressure monitoring over a wide temperature range; CNR4 net radiometer (Kipp & Zonen) for measurement of the energy balance between incoming short-wave and long-wave Far Infrared Radiation (FIR) versus surface-reflected shortwave and outgoing long-wave radiation).

A Vaisala Ceilometer CL31 (Figure 3) was installed on the roof of the Department of Physics and Astronomy of the University of Bologna (Irnerio St., 46 in Figure 2) for measuring and analyzing the boundary-layer height at a location adequate to characterize the atmospheric structure of the whole city and as such of both the investigated sites.





*Figure 3: The Vaisala Ceilometer CL31 for the measurement of boundary layer height in Bologna city center.*

During both the summer and winter experimental campaigns, two intensive thermographic campaigns were carried out with two high-performance thermal cameras to analyze the thermal characteristics of physical elements in the two urban street canyons.

In addition, 5-minutes traffic counts in the two street canyons and their vicinity were available by means of inductive loops from the Bologna Municipality.

### **3.1.3 Experimental protocol and quality check**

The experimental protocol and the quality checks conducted to eliminate spikes from fast-sampled raw high-resolution measurements are fully described in the first version of this Deliverable. In synthesis, both street canyons were equipped with high-time resolution instrumentation at three height levels, i.e. at ground level, at mid-level inside the canyon and above the canyon on the rooftop of the highest building. This setup allowed to characterize turbulent structures within and above the two street canyons. In particular, all sonic anemometers were setup to collect measurements with a 50ms time resolution, to allow for a high-resolution determination of turbulent features, such as momentum and sensible heat fluxes; thermo-hygrometers acquired measurements at 1s time basis.

Table 3 provides information on the kind and time resolution of the air pollution measurements within the two experimental field campaigns.

Time resolution												
	Daily		Hourly					Minute				
	PM <sub>10</sub>	PM <sub>2.5</sub>	NO <sub>x</sub>	CO	O <sub>3</sub>	SO <sub>2</sub>	BTEX	NO <sub>x</sub>	CO	O <sub>3</sub>	PNC	BC
<b>Marconi St.</b>	✓	✓	✓	✓	✓	✓	✓	✓	✓	✓	✓ (winter)	✓ (winter)
<b>Laura Bassi St.</b>	✓	✓	✓	✓	✓	✓		✓	✓	✓	✓ (winter)	✓ (winter)
<b>Porta S. Felice</b>	✓	✓	✓	✓			✓					
<b>Giardini Margherita</b>	✓	✓	✓		✓							

Table 3: Details on air pollution pollutants and time resolution of the air quality instrumentation located in the two street canyons and at fixed air pollution monitoring stations within the two experimental Bologna field campaigns.

The ceilometer was installed during the summer experimental campaign on the roof of the Department of Physics and Astronomy of the University of Bologna in order to estimate the urban boundary layer height especially during events of special interest occurred within the experimental field campaigns.

## 3.2 Lazzaretto

Within the iSCAPE project, the Lazzaretto area in the outskirts of Bologna was chosen as the site where to conduct the evaluation of the effectiveness of the photocatalytic coatings to mitigate NO<sub>x</sub> air pollution in urban areas. The intensive experimental campaign deployed at Lazzaretto is extensively described in D3.8 ('Report on deployment of neighborhood level interventions'), while data gathered within the campaign were used to verify the setup of CFD simulations conducted to evaluate the effectiveness of photocatalytic coatings in the different seasons (D3.6 'Report on photocatalytic coating').

### 3.2.1 Site description

An intensive experimental field campaign was carried out in two parallel street canyons at the Lazzaretto site in the outskirts of Bologna during August 2018 (04-08-28/08/2018) to monitor air pollution and meteorology. The Lazzaretto area, part of the campus of the University of Bologna campus, is located about 3 km north-west of the Bologna city center close to a busy road linking the Bologna suburbs with the city center. Figure 4 shows the location of the Lazzaretto area and of other air pollution and meteorological stations in the city of Bologna, namely: Porta San Felice urban traffic and Chiarini St. suburban background air quality stations; the 'Guglielmo Marconi' Bologna airport (LIPE in Figure 4; 44.53°N, 11.3° E; 38m asl height) and Torre Asinelli synoptic meteorological stations; the Bologna Urbana urban meteorological station; Irnerio St., 46, location of the Department of Physics and Astronomy where the ceilometer for measuring was installed boundary-layer height.

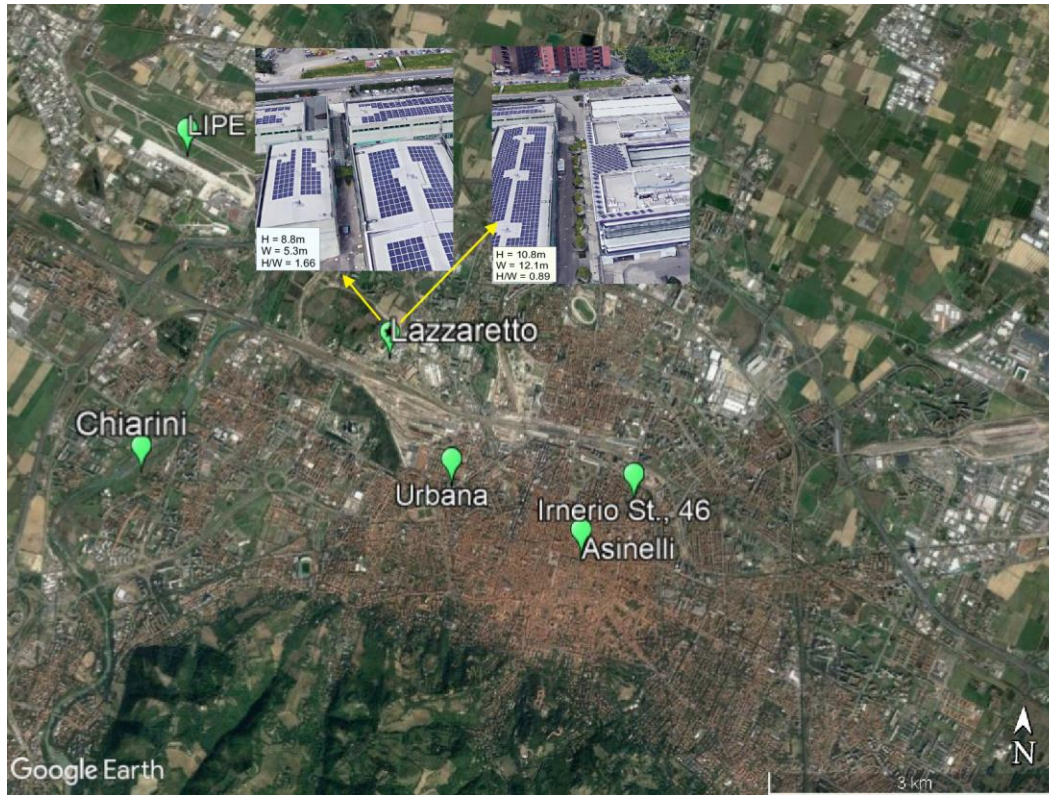


Figure 4: Location of the Lazzaretto area and other measurement sites for air pollution and meteorological variables within the intensive experimental field campaign of summer 2018: the two street canyons in Lazzaretto area (aspect ratio  $H/W = 1.66$  and  $0.89$ , respectively); Bologna Urbana, Asinelli and Bologna airport (LIPE) meteorological stations; Chiarini ARPAE air quality station; Innerio St., 46 where the ceilometer was located (source: Google Maps).

Similar to the Bologna experimental field campaigns, two similar and parallel street canyons with the same NW orientation were identified. For the purpose of evaluating the effectiveness of photocatalytic coatings, one of the two canyons was painted with the photocatalytic coating while the other one was left untouched and was used as reference. However, besides being useful for the evaluation of the effectiveness of the coatings in real street canyons, data gathered within the summer 2018 experimental campaign at Lazzaretto are also useful to better elucidate processes governing flow dynamics and turbulence in two real street canyons. As such, measurements conducted within the pilot at Lazzaretto can be used to derive or confirm scaling laws and parameterizations of turbulent flows in real canyons.

### 3.2.2 Instrumental setup

Similar to the Bologna experimental field campaigns, two ARPAE mobile laboratories equipped for the measurements of air quality pollutants  $\text{NO}_x$ ,  $\text{NO}$ ,  $\text{NO}_2$ ,  $\text{CO}$ ,  $\text{O}_3$ ,  $\text{SO}_2$  at 1-minute time resolution, and of daily averages of  $\text{PM}_{10}$  and  $\text{PM}_{2.5}$  were deployed in the two Lazzaretto street canyons. The two ARPAE vans were also equipped for the measurements of basic meteorological variables such as wind speed and direction, air temperature and relative humidity.

Additionally, two height levels, one within and one above the two canyons, were instrumented with sonic anemometers, temperature and relative humidity probes, and one barometer to retrieve fast, high-precision and high temporal resolution measurements of the three components of wind velocity, air temperature, relative humidity and air. The highest level was also instrumented with a

CNR4 (Kipp & Zonen) net radiometer, consisting of a pyranometer pair, one facing upward and the other facing downward, and a pyrgeometer pair with a similar configuration to measure long-wave radiation; as such, this instrument allows to evaluate the energy balance Far Infrared Radiation (FIR) versus surface-reflected shortwave and outgoing long-wave radiation. Two temperature sensors, a Pt-100 and a Thermistor, are integrated for compatibility with every data logger. The temperature sensor is used to provide information to correct the infrared readings for the temperature of the instrument housing. Besides providing rapid response 3D wind field data, sonic anemometers allow estimating a range of turbulence parameters and fluxes using eddy covariance techniques. Additionally, on the rooftop of one of the two canyons, a high-performance, non-dispersive, open-path infrared CO<sub>2</sub>/H<sub>2</sub>O analyzer (LI-COR LI-7500 RS) designed for use in eddy covariance flux measurement systems, providing simultaneous, high-speed measurements of CO<sub>2</sub> and H<sub>2</sub>O in the free atmosphere an open path CO<sub>2</sub>/H<sub>2</sub>O gas analyzer was installed to determine CO<sub>2</sub> and water vapour fluxes using eddy correlation techniques when coupled with sonic anemometers air turbulence data. In the open-path design, the instrument samples the air that is moved through the open cell of the gas analyzer by the wind.

The sampling cell of the instrument is usually positioned near the sonic anemometer, with a horizontal separation of no more than about 10-20 cm. Although it is important that the two instruments are close enough, the separation should be maintained so that not to significantly distort the natural air flow through the anemometer by the analyzer head. The head can be slightly tilted to minimize the amount of precipitation accumulating on the windows. The LI-7500 RS is designed for eddy covariance flux measurements, but it is also suitable for profile measurements or any other application that depends on high-speed CO<sub>2</sub> gas or water vapor measurements.

The LI-7550 Analyzer Interface Unit is an additional component to the LI-7500RS housing the gas analyzer electronics and a connector for the USB flash drive where all the data are stored. Inside the interface unit three Ethernet connectors allow the connection of the interface to the SmartFlux 2 System, a component of LI-COR eddy covariance system, and to the PC to download the data. The SmartFlux2 System accepts digital input from a sonic anemometer and combines the anemometer data with gas concentrations or densities to time-synchronized files, basically allowing the coupling of the WindMaster sonic anemometer directly to the LI-COR LI-7500RS gas analyzer.

Finally, the Lidar ceilometer installed on the roof of the Department of Physics and Astronomy of the University of Bologna (Irnerio St., 46) remained there also during the summer 2018 experimental campaign, therefore providing the boundary-layer height and the possibility to characterize the urban structure even within this monitoring campaign.

### **3.2.3 Experimental protocol and quality check**

Similar to the two field campaigns in Bologna, one ARPAE mobile measuring station was located in each street canyon at Lazzaretto, while additional air quality measurements from the fixed ARPAE monitoring sites located nearby in Bologna (Porta San Felice and Chiarini St., respectively one urban traffic and one suburban background station) were provided by ARPAE for comparison.

In addition, both street canyons were equipped with high-frequency meteorological and turbulence instrumentation at two different height levels, one inside and the other above the canyon, i.e. at ground level on the roof of the ARPAE van and above the canyon on the rooftop of the highest building. In particular, on the rooftop of each street canyon, one sonic anemometer, one temperature and relative humidity probe and one CNR4 net radiometer were installed, with a slightly different installation heights of the rooftop instrumentation due to the different height of the two canyons. On the rooftop of one of the two canyons an open path CO<sub>2</sub>/H<sub>2</sub>O gas analyzer was installed. Figure 5 shows the instrumental setup of the coupled anemometer and LI-COR 7500RS gas analyzer. In particular, the coupling of sonic anemometers with other field instrumentation as



described here allows the determination of not only rapid response 3D wind field data, but also the estimation of a range of turbulence parameters and fluxes, including in this case CO<sub>2</sub> and H<sub>2</sub>O fluxes, with the Eddy Covariance method.



*Figure 5: Sonic anemometer and LI-COR 7500RS gas analyzer on the rooftop of one of the two canyons in Lazzaretto area.*

All sonic anemometers had a sampling rate of 20 Hz (50 ms time resolution), to determine turbulent features with a high-resolution. The LI-COR 7500RS was also set to sample at 50 ms time resolution.

Time series obtained from data sampled at 1 Hz or lower resolution must be “cleaned” before computing covariances in eddy correlation, by means of despiking and rotation into a different coordinate system. In particular, in this work such “cleaning” was accomplished first by eliminating all the spikes and after using the procedure suggested by McMillen (1988). The despiking procedure assumes a Gaussian distribution inside a stationary set of data (30 minutes interval in the data series). Values falling outside three standard deviations from the mean are rejected. Despiked wind components are then rotated to align the reference system to the canyon direction so that  $u$  is the cross-canyon,  $v$  is the along-canyon and  $w$  is the vertical wind component, respectively. The McMillen method consists in (1) ‘detrending’ (by use of running mean removal), (2) calculation of the entire stress tensor (which allows a three-dimensional coordinate rotation to be performed on the covariances), (3) software-adjustable timing delays for each instrument channel. Once data have been despiked and rotated according to the canyon orientation, both

mean flow and turbulent quantities are computed at the three levels inside and above the canyons. To ensure general robustness of the analysis, without losing small scales processes, all quantities have been averaged in time over 5 minutes.

### 3.3 Dublin

Low-Boundary walls (LBWs) can provide a solution to enhance localized dispersion and improving air pollution in distinct street canyons settings.

Within iSCAPE, Dublin city in Ireland has been chosen as the location for examining LBWs in the built environment. LBWs are a type of physical PCSs and have been shown to effectively impact on air flow and pollutant dispersion in low-rise street canyons (Gallagher et al., 2012; King et al., 2009; McNabola et al., 2008, 2009). Therefore, Dublin provides an experimental setup and location to examine the implications of the LBW on personal exposure to air pollution as a type of PCS.

This report explores the potential of using LBWs as an effective intervention to reduce the personal exposure to air pollution in the built environment through a real-world field experiment.

The report provides results relating to the effects of the LBWs on the dispersion of NO<sub>x</sub> gases, PM<sub>10</sub> and PM<sub>2.5</sub> based on different sets of wind directions in a street canyon geometry.

#### 3.3.1 Site description

Two phases comprehensive air pollution monitoring campaign was implemented in Dublin. A four-week phase 1 campaign was implemented in 2018 based on two weeks of winter monitoring (March 2018) and the other two weeks of monitoring during summer (July 2018). This campaign takes place on Pearse Street, which is located in the city center (Figure 6**Errore. L'origine riferimento non è stata trovata.**). This street canyon is characterized by a high traffic volume. Pearse Street has 4 lanes all going in the same direction with a total width of 16 m and it has a North-South alignment. An LBW 18 m long and 1m high has been installed along the edge of the footpath on one side of the street, see Figure 6. Two monitoring points have been installed on the LBW, one at each side of the wall, Front side (F) and Backside (B).

The Phase II of the field experiment includes a three-week campaign starting from July 9, 2018, to July 27, 2018. It was carried out near the same location at Pearse Street, Dublin, as the previous phase (Figure 6). However, in this phase, PM<sub>2.5</sub> and PM<sub>10</sub> were used as a reference pollutant with PM<sub>2.5</sub> being for the first two weeks while PM<sub>10</sub> for the third week of the experiment. Similar to Phase I, this part of field experiment also consists of setting up of the LBW on the existing bollards. However, in this phase, LBWs were made more continuous and longer than the previous one.

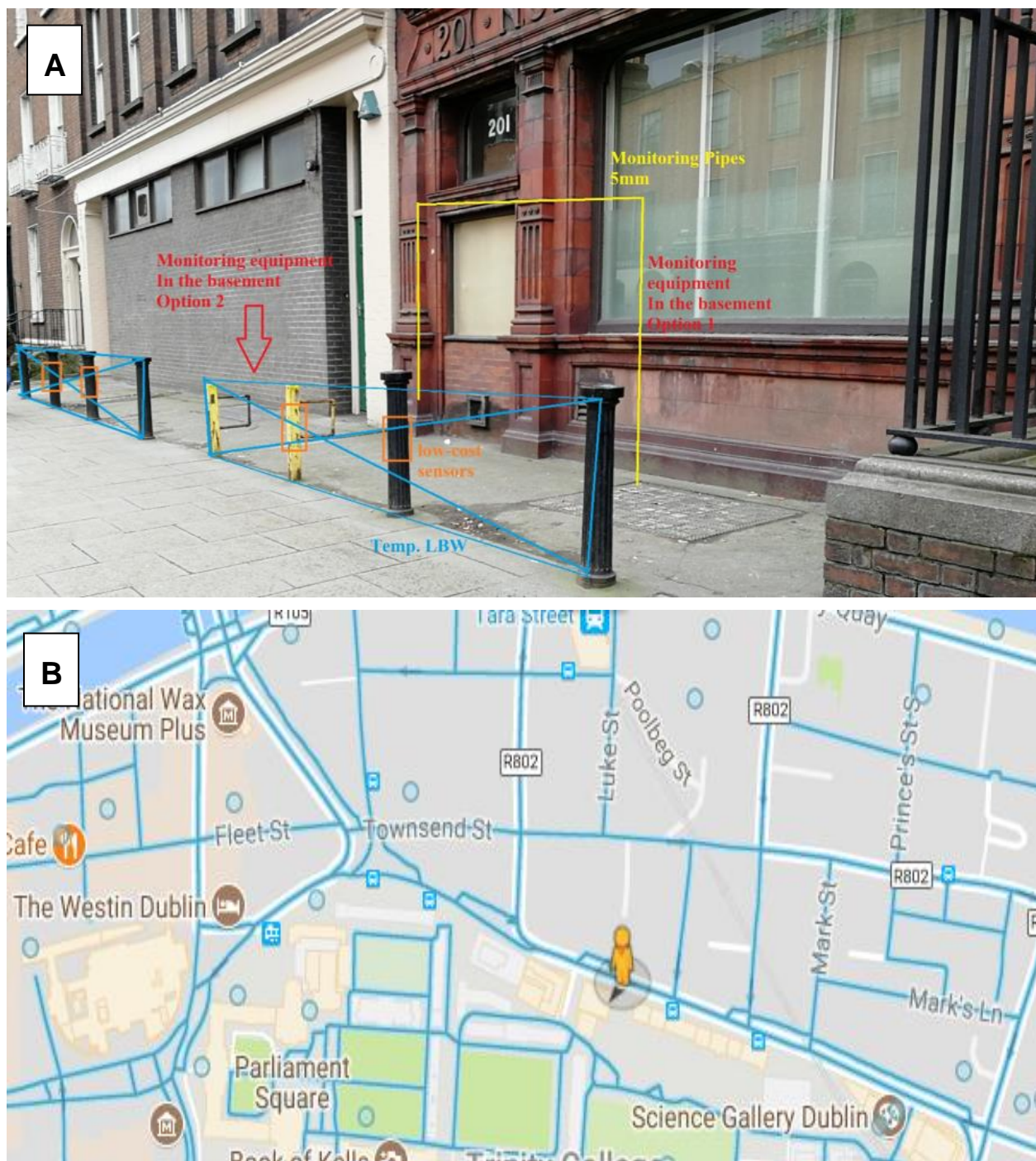


Figure 6: (A) Experimental site on Pearse Street in Dublin, Ireland (B) Map of the experimental monitoring site in Dublin (source: Google Maps).

### 3.3.2 Instrumental setup

In phase 1, Two Teledyne Chemiluminescent NO/NO<sub>2</sub>/NO<sub>x</sub> Analyzers (Model 200E and 200EU) (Figure 7) have been used to monitor the NO<sub>x</sub> gases in the two monitoring points (F) and (B) (the



two sides of the LBW). A wind vane (Cabled Vantage Pro2™ with Standard Radiation Shield) was installed on the rooftop of the adjacent building to monitor the wind speed and wind direction. Data presented in this report for phase 1 were collected from the fortnight period during working hours (08:00 to 19:00) and 5 days per week.

Data were collected using the following equipment and time resolution:

- NO/NO<sub>2</sub>/NO<sub>x</sub> concentrations (ppm) (5-minute averaged values) from the NO<sub>x</sub> analyzer (N2CNC1-AVG, NXCNC1-AVG and NoCNC1-AVG).
- Wind Speed and wind direction (5-minute averaged values).

For Phase 2, two portable aerosol analyzers by TSI were used. The first analyzer was model SIDEPAK AM520 and the second analyzer was DUSTTRAK DRX8534, see Figure 8. The Phase 2 of the field experiment includes a three-week campaign starting from July 9, 2018, to July 27, 2018. It was carried out near the same location at Pearse Street, Dublin, as the previous phase (Figure 6). However, in this phase, PM<sub>2.5</sub> and PM<sub>10</sub> were used as a reference pollutant, in particular focusing on PM<sub>2.5</sub> for the first two weeks and on PM<sub>10</sub> for the third week of the experiment. Similar to Phase I, this part of field experiment also consists of setting up of the LBW on the existing bollards. However, in phase 2, LBWs were made more continuous and longer than the previous one.



Figure 7: Teledyne Chemiluminescent NO/NO<sub>2</sub>/NO<sub>x</sub> Analyzer used in Dublin experimental campaign.



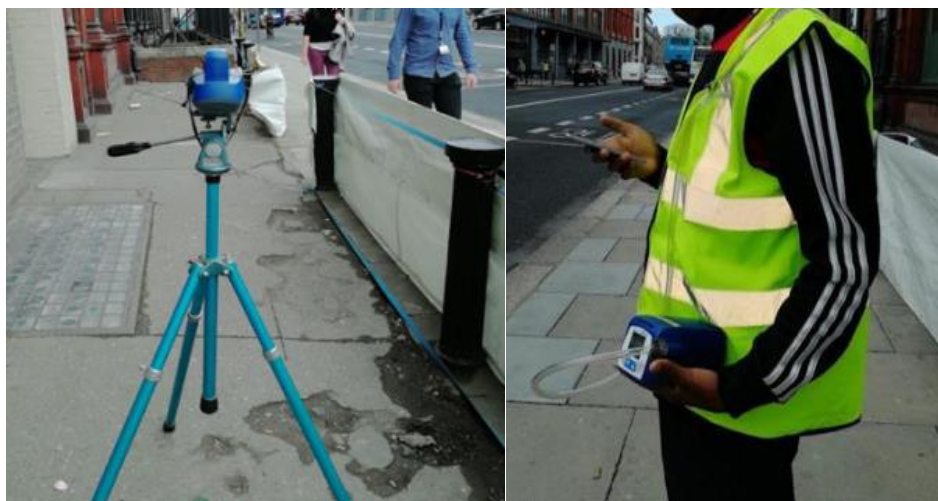


Figure 8: Left figure shows the researcher standing with AM520 to measure concentration in front of the wall while the right figure shows the DRX8534 stationed on a tripod behind the wall.)

### 3.3.3 Experimental protocol and quality check

The Pearse Street monitoring site has a bright area (without any disturbance to air flow) adjacent to the LBW.

The field measurement is started and ended around 08.00 and 18.00 (local time) each day, respectively. This enables to collect 8 to 10 hours of data every day. Inter-calibration between each set of instruments is achieved by running instruments side by side for 20 to 30 min prior beginning and after finishing the measurements. Inter-calibration between each set of instruments is achieved by running instruments side by side for 20 to 30 min prior beginning and after finishing the measurements.

## 3.4 Guildford

### 3.4.1 Data processing methods for low-cost sensors

#### Introduction

The air quality improvements resulting from PCSs such as LBWs, photocatalytic coatings, trees and hedges depends on a range of factors. These include wind speed, wind direction, pollutant concentration, leaf area index (LAI – a dimensionless metric of leaf area per unit ground area  $\text{m}^2 \text{m}^{-2}$ ) of the vegetation, etc. As it is difficult to create controlled conditions for these factors, the solution most often opted for is to measure the air quality improvements over a long time and subsequently using statistical analysis to separate the influence of the different factors.

A large amount of data generated in long time series measurements of air quality requires automatic data logging and network transfer of data to central repositories. Unfortunately, this type of system is prone to errors that can result in lost data or poor data quality (Campbell et al., 2013). The emergence of low-cost sensors over the last couple of years (Kumar et al., 2015), has enhanced this issue. This is due to the increased temporal resolution of these sensors and the

possibility of obtaining greater spatial coverage within the same financial constraints. In traditional air quality monitoring programs, this problem is alleviated through extensive quality control and data cleaning procedures often carried out manually, with associated high costs (Ottosen et al., 2016). The growing data amounts from low-cost sensors mean that manual quality control is no longer feasible (Alavi-Shoshtari et al., 2018). Based on the framework proposed by van Zoest et al. (2018), we propose that a generic data cleaning methodology could be broken down in the steps illustrated in Figure 9. To limit the scope of the present study, the focus is solely on the steps marked with green in Figure 9, i.e. quality control and outlier detection as well as gap filling. These are related since the removal of poor-quality data and outliers leads to gaps that subsequently have to be filled.

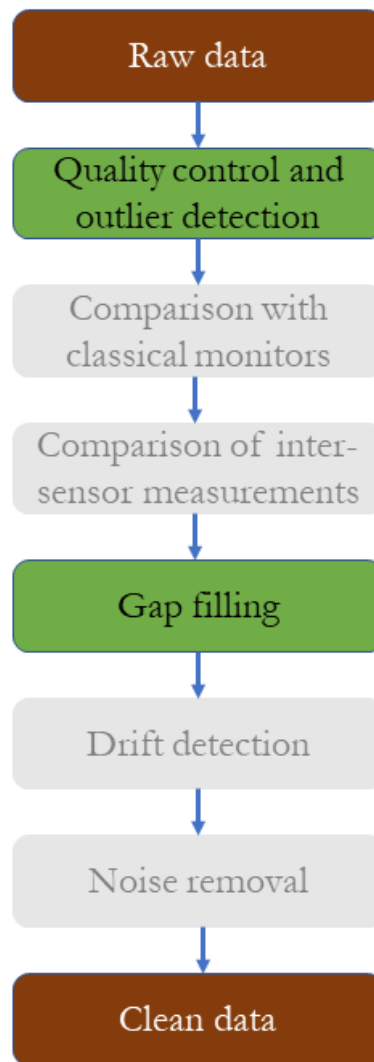


*Figure 9: Steps in the generic data processing methodology. The green boxes represent steps included in the present study, and the grey boxes represent steps left for future studies.*

In the present study, we have reviewed the available methodologies for these steps, applied a selection of commonly adopted methods to a case study (consisting of an 11-month long time

series of primary data from a low-cost sensor) and discussed the applicability of each methodology. This section (3.4.1) is a summary of Ottosen and Kumar (2019), where more details are available.

## Measurements

The data for the development and validation of the data processing methods were obtained from a time series measurement from 10 July 2017 to 26 June 2018 with a single AQMesh sensor (Environmental Instruments LTD, UK). The sensor measured five gaseous pollutant species, i.e., NO, NO<sub>2</sub>, SO<sub>2</sub>, CO and O<sub>3</sub> at 15-minute temporal resolution. The sensor pod also measured temperature and relative humidity, and a proprietary algorithm was used for correcting the effect of these meteorological parameters.

The low-cost sensor was mounted at 2.7 m above ground, as a balance between measuring at a relevant height for health applications and preventing vandalism, on the stand of a bus stop in the University of Surrey (Guildford, Surrey, UK) campus area. An aerial photo of the location is shown in Figure 10. The bus stop contains two bays in parallel and is being serviced six times per hour during day time for the stand immediately next to the sensor, and twelve times per hour during day time for the stand further away from the sensor.

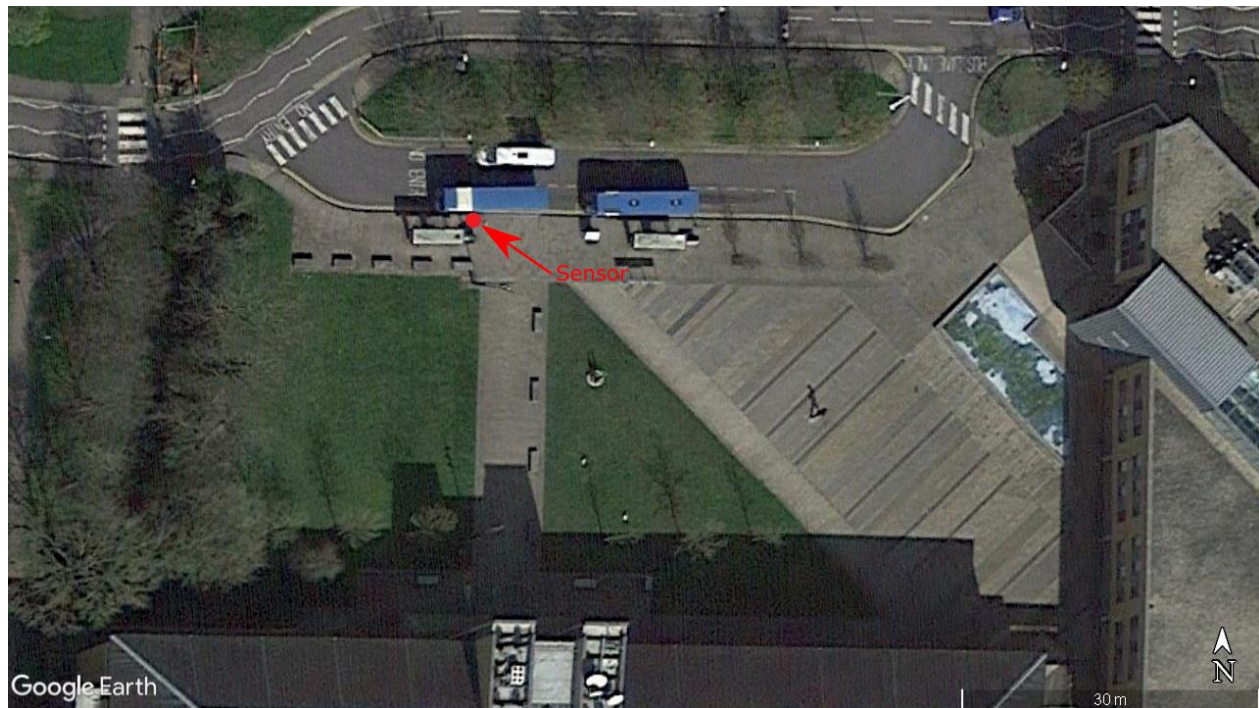


Figure 10: Aerial photo of the bus stop where the measurements were taken. The location of the sensor is marked with a red dot. Data source: Google Earth. Figure from Ottosen and Kumar (2019)

## Data processing methodology

### Quality control

The AQMesh sensor comes with an internal quality control procedure. This procedure outputs a status tag for each species for each data point. The status tag can take on six values being

*Stabilizing, Rebasing, Greater Than Upper Limit, Less than Lower Limit, Valid and N/A.* The first step in the quality control procedure was thus to only retain data with a *Valid* status tag, which was conducted both on a species by species level and for all species in one operation.

A visual inspection of the data revealed that the built-in quality control did not capture all the erroneous data. An example of this is shown in Figure 11. In this figure, it is evident that some kind of error occurs shortly after May 14, as marked by the arrow. Comparing the time series before and after this point reveals that the variance has increased by almost a factor of 100. An additional algorithm to detect these changes were therefore developed.

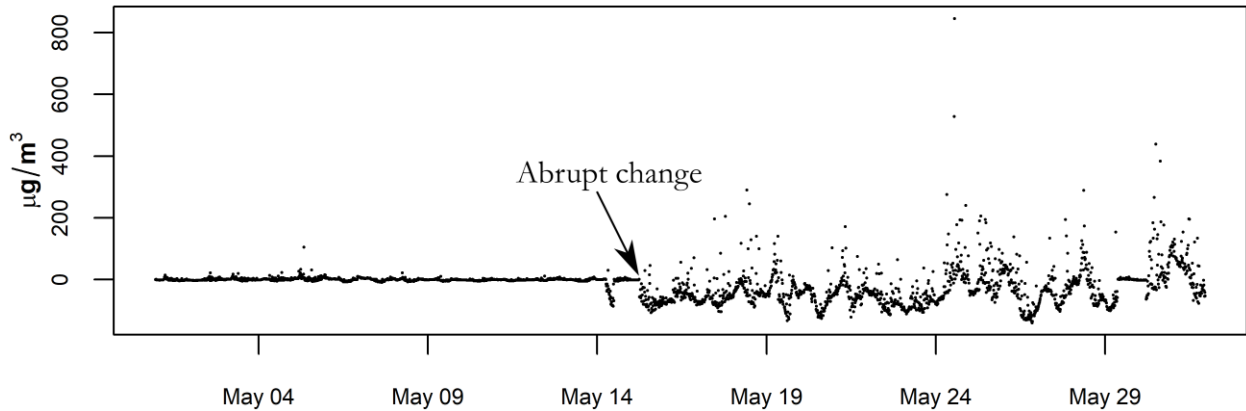


Figure 11: Example of an abrupt change in the SO<sub>2</sub> time series in May 2018. All data in the figure carry a valid status tag.

To this end, the Pruned Exact Linear Time (PELT) (Killick et al., 2012) algorithm was used to divide the time series into segments of homogeneous mean and variance. Since air quality time series naturally contain large variations in both mean and variance, a minimum segmentation length of 1000 data points and a penalty factor of 1000 was used to limit the changes to the erroneous data. For the mean values of the different segments, the error score was calculated as the absolute difference between the mean value of the segment and the mean value of the entire time series normalised with the mean value of the entire time series. The erroneous segments were then found by a *k*-means clustering methodology with two clusters of the error scores of the respective segments. For the variance, the procedure proceeded in two steps. Firstly, a reference variance was found by running a PELT segmentation with a penalty factor of 1000 and a minimum segment length of 10000 data points. The variance of the longest segment of this procedure was then used as a reference variance. Secondly, the PELT algorithm was run again with the same settings as for the mean value and erroneous measurements were assigned to segments with a variance larger than ten times the reference variance. The measurements classified as erroneous was assigned their own status tag called *Error*. The principles of the PELT algorithm are explained below.

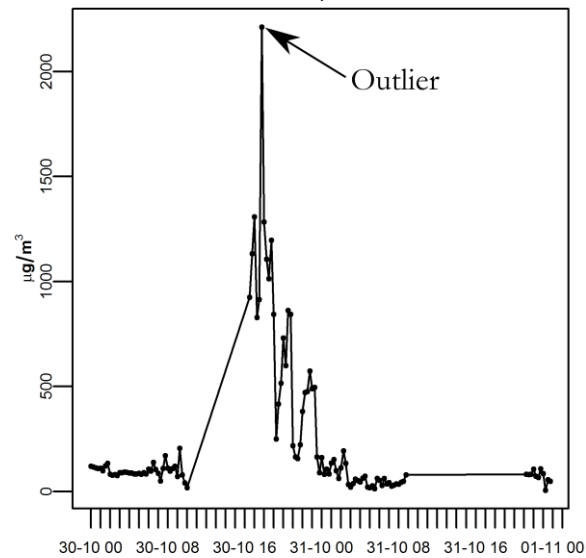
Given an ordered sequence of data (in this case air quality measurements),  $y_{1:n} = (y_1, \dots, y_n)$ , the aim of the algorithm is to find the number of changepoints  $m$  with positions  $\tau_{1:m} = (\tau_1, \dots, \tau_m)$ . To this end, the following expression is minimised:

$$\sum_{i=1}^{m+1} [C(y_{(\tau_{i-1}+1):\tau_i})] + \beta f(m) \quad (1)$$

Where  $C$  is a cost function for segment  $i$  and  $\beta f(m)$  is a penalty function to prevent overfitting.

## Outlier detection

Apart from the erroneous data points detected in the section above, low-cost sensors frequently contain outliers as well (van Zoest et al., 2018). An example of an outlier is shown in



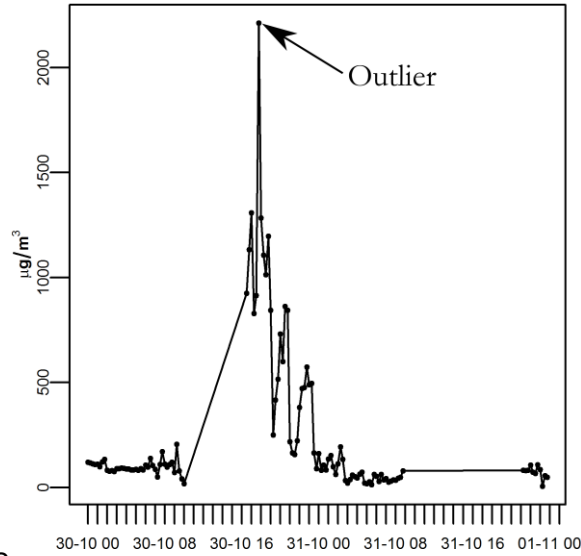


Figure 12  
Figure 12.

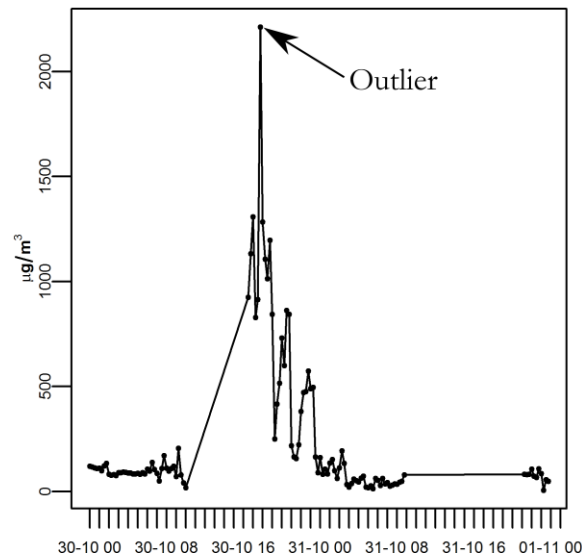


Figure 12: Example of an outlier in the concentrations from 30 October 2017.

Whereas errors are characterized by being large groups of data points with extreme values or extreme statistical properties, outliers are single data points that deviate markedly from the rest of the data. In the present study, two outlier detection methodologies were compared:

- *k*-Nearest Neighbor (*k*-NN) is one of the simplest outlier detection methodologies and serves as an example of a point outlier detection method. This has the advantage that it utilizes the fact that data are multivariate. In *k*-NN outlier detection, the anomaly score of a data instance is defined as its distance to its  $k^{\text{th}}$  nearest neighbor in a given data set. In the present study the Euclidian distance is used:



$$d(\vec{p}, \vec{q}) = \sqrt{(q_1 - p_1)^2 + (q_2 - p_2)^2 + \dots + (q_n - p_n)^2} \quad (2)$$

Where  $\vec{p}$  and  $\vec{q}$  are two air quality measurements with the species representing the components of the vectors.

- Regression-based outlier detection is an example of a contextual outlier detection method. This approach has the advantage to take the temporal aspect of the data into account. A model which has been extensively used in regression-based techniques is AutoRegressive Integrated Moving Average (ARIMA), which is also used in the present study. The equation for the ARIMA model is:

$$\phi(B)(1 - B^d)y_t = c + \theta(B)\varepsilon_t \quad (3)$$

Where  $y_t$  is the time series of air quality measurements,  $B$  is the backshift operator,  $\phi(z)$  and  $\theta(z)$  are polynomials of order  $p$  and  $q$ , respectively. The outlier score is subsequently defined as the residual between the fitted model and the measurements.

### Gap filling

Removal of erroneous measurements and outliers creates gaps in the time series. To preserve the statistical properties of the original data gap filling techniques can be used. In the present study, cross-validation was used to assess the performance of specific gap filling techniques following the approach of Junninen et al. (2004).

Given that the impact of a specific gap depends on the length of the gap, the position of the gap in the time series and the total proportion of missing data (Junninen et al., 2004), testing all potential combinations of these properties was deemed infeasible. Instead, a cross-validation dataset designed to be particularly challenging to the gap filling technique was designed as follows:

- In the first step, all potential gap locations were found by looping through the time series. For multivariate gap filling methods, only measurements where all four species had measurements were included in this step.
- The probability of sampling each gap location was assigned to the mean of the relative difference between the mean, standard deviation, skewness and kurtosis of the original dataset, and a dataset with a gap at this particular location. In this way, gap locations with large effects on the resulting distribution had a disproportionately high probability of being selected.
- For each combination of gap length and gap proportion, we selected 100 samples of the possible locations in the time series.

The maximum gap length of 100 data points corresponds to 25 hours. It was selected as a balance between having as large as possible a gap length and still having a substantial number of gap locations to choose from.

To validate the performance of the individual gap filling technique, the following statistical indicators were used: Difference in mean, standard deviation, skewness, and kurtosis, correlation coefficient, index of agreement, root mean square error and mean average error between the filled time series and the original time series.

The following gap filling methods were included in the present study:

- **Univariate linear interpolation.** This method was selected in the present study as one of the simplest gap filling methods.
- **Cubic spline fitting.** This method was included as an example of a slightly more complicated method, including more data points on each side of the gap.
- **Univariate Neural Networks.** The most complicated gap filling method is Neural Networks (NN); in this case, a feed-forward neural networks with a single hidden layer and lagged inputs.
- **Multivariate linear regression.** For multivariate gap filling, multivariate linear regression was selected, as this is one of the simplest multivariate approaches. This was implemented such that the missing species was fitted as a linear function of the remaining four species.
- **Multivariate Neural Networks.** As an example of a more complicated multivariate approach, the same approach as for univariate neural networks was used, but this time with the remaining species as input.



### 3.4.2 Long-term time series measurements on a hedge

#### Site description



Figure 13: Overview of the sampling site in Stoke Park (top), a photo of the sensor outside the park (bottom-left) and the sensor inside the park (bottom-right).

The sampling site for the present study was Stoke Park, Guildford, UK. An aerial photo of the site is shown in Figure 13. This location was chosen since it contains an unobstructed hedge next to

a busy road, and thus poses an ideal location for evaluating the effect of the hedge on the air pollution concentrations. The hedge is shielding a children's playground in the park, which also contributes to the relevance of the location. Besides, the location has been used in two previous field campaigns (Abhijith and Kumar, 2019; Abhijith and Kumar, in prep.) and thus allows for comparison of results.

The hedge is of species Horn beam (*Fagus sylvatica*) and has a width of 1.2 m and a height of 2 m and a distance to the road of 2 m. The LAI was measured in June-September 2018 equal to 4.47 m<sup>2</sup>/m<sup>2</sup>. The road next to the park has two lanes and two-way traffic, with an average hourly traffic volume of 1200 vehicles. The opposite side of the road is lined with trees and behind the trees is a row of two-story detached houses.

### Instrumental setup and experimental protocol

Two living lab stations were attached to respectively a lamp column and a fence pole on each side of the hedge. The two stations were located close to the hedge to measure the maximum signal from the hedge. The mounting height corresponds to the adult breathing height of ~170cm to 180 m above ground. The living lab stations have been developed in the iSCAPE project by IAAC (Institute of Advanced Architecture of Catalunya). They measure NO<sub>2</sub>, CO and O<sub>3</sub> as well as PM<sub>1</sub>, PM<sub>2.5</sub> and PM<sub>10</sub> at 1-minute temporal resolution. Further details of the stations can be found in Camprodon et al. (2019).

The aim of the research is to measure the expected reduction in air pollution concentration between the two stations because of the hedge. It is the hypothesis of the study that the air quality reduction depends on the wind speed, the wind direction and the leaf density of the hedge. In the present study, meteorological data will be obtained from the NOAA (National Oceanic and Atmospheric Administration) Integrated Surface Database ([www.ncdc.noaa.gov/isd](http://www.ncdc.noaa.gov/isd)) for the measurements from Farnborough Airport. The change in LAI for the hedge over the season will also be measured using an AccuPAR LP-80 ceptometer. Subsequently the aim of the study is to relate the reduction in air pollution concentration to these environmental parameters via a mathematical model. Methods for quality control, outlier detection and gap filling as described in section 3.4.1 will also be applied.

### 3.4.3 Field experiments evaluating air pollution reduction of various GI

We studied the influence of roadside GI on the concentrations of particulate matter  $\leq 10 \mu\text{m}$  (PM<sub>10</sub>),  $\leq 2.5 \mu\text{m}$  (PM<sub>2.5</sub>),  $\leq 1 \mu\text{m}$  (PM<sub>1</sub>), black carbon (BC) and particle number concentrations (PNC) under three GI configurations – (i) hedges only, (ii) trees only, and (iii) a mix of trees and hedges/shrubs – separately in close (<1m) and away (>2m) road conditions. The changes in concentrations of PM<sub>10</sub>, PM<sub>2.5</sub>, PM<sub>1</sub>, BC and PNC at all these six sites were estimated by comparing simultaneous measurements behind and in-front/clear area of GI. A portable battery-operated experimental set-up was designed for measuring the pollutant concentrations for 30 full days over a period of the three-month field campaign. Each day about 10 hours of continuous data were recorded simultaneously before and after the GI, capturing both morning and evening traffic peaks. Details of the monitoring location, instrument setup, experimental protocol, quality assurance and preliminary results were provided in the previous version of this Deliverable. Here, we present a key summary of the work in this report, but a thorough analysis and findings can be found in Abhijith and Kumar (2019).

### ***3.4.4 Field investigation of apportionment of deposition and dispersion components of air pollution reduction by GI***

The GI improves air quality by modifying the airflow around the canopy and facilitating deposition and absorption of the pollutant on leaves as well as other plant body parts. A previous experimental campaign has effectively quantified the overall reduction of air pollution exposure behind the various types of GI (Abhijith and Kumar, 2019). Nevertheless, the quantitative analysis of dispersion and deposition contributions of the total improvement in air quality improvement behind the GI is yet to be carried out. In this follow-up field campaign, we aim to experimentally quantify the dispersion and deposition components in overall air pollution exposure reduction by GI. For this investigation, we have selected one of the six previous monitoring sites, Stoke Park. This site is one of the living lab stations which ensures extended data availability and optimizing our data collection efforts. In this work, there were two monitoring locations along Stoke road, one location was Stoke Park with a hedge fencing a children's playground and a clear area without any obstructions to wind flow (further details are provided in the following section). At GI location, the pollutant concentrations in front of and behind the GI were measured. Conversely, in clear area, there were two monitoring points, with the first being equivalent to in front of GI point on the footpath while the second measurement point was away from the road keeping same distance corresponding to that behind GI. Comparing pollutant concentrations at two measurement points (the GI site and the clear area) provides the difference in dispersion component. The deposition of particles on leaves was quantified by image processing of collected micrographs from a scanning electron microscope. Details are provided in the following sections.

#### **Site Description**

Figure 14 shows the Stoke Park with hedge and a clear area along Stoke road selected for our campaign, previously described. This experimental site had a well-maintained hedge of 2 m height on the boundary of a children's play area adjacent to a two-lane busy road connecting two major towns Woking and Guildford (Road number A323). The hedge was 36 m long and 1.5 m thick all along the road. LAI was measured from changes in photosynthetically active radiation passing through overlaying foliage measured by a handheld Ceptometer (Meter Environment, ACCUPAR LP80). The hedge had a LAI of  $6.64 \text{ m}^2 \text{ m}^{-2}$ . The clear area lied along the same road with no obstructions to wind flow from the road, and housing layout was similar to the hedge location. Blue and yellow points in Figure 14 show the measurement locations on both sites.





Figure 14: Two monitoring locations along Stoke road, top figure section shows hedge location at Stoke Park, bottom displays clear area. Right section shows a plan view of both locations.

## Experimental setup and protocol

In this work,  $PM_1$ ,  $PM_{2.5}$ ,  $PM_{10}$ , and BC were monitored. Specifically, two GRIMM aerosol monitors, model EDM 107 and 11-C measured  $PM_1$ ,  $PM_{2.5}$ , and  $PM_{10}$ . The instrument provides PM concentrations on 31 different channels at 6 seconds time resolution. In addition, particles collected on PTFE filters inside the GRIMM monitor can be used for chemical and morphological characterization. BC concentrations were collected using a couple of MicroAeth AE51 (Aeth Labs) with time averaging period of 10 seconds. Attenuation generated due to instrumental optical and electronic noise was rectified by post-processing the data with Optimised Noise-reduction Averaging algorithm (ONA; Hagler, et al. 2011). Local meteorological conditions (air temperature, relative humidity and wind speed and direction) were logged by a portable weather station (Kestrel 4500) at 1-min resolution. All instrument data was averaged to 1-minute to match with the wind data. Manual traffic counting was performed every 20 minutes of an hour. LAI was estimated from changes in photosynthetically active radiation passing through overlaying foliage by a handheld ceptometer Accu-PAR LP80.

Both sets of instruments (including GRIMM, and MicroAeth) were mounted on a tripod stand at a typical breathing height of about 1.5 m and one set was kept in front of the GI and other behind GI. At clear area, both tripods were located equidistant from the road as in GI location. The campaign monitored 6 days at GI location and 5 days at clear area site. The field measurement was started and ended around 08:00 h and 18:00 h (local time), respectively. This enables to collect 8 to 10 hours of data every day. This measurement methodology was adopted due to difficulties in conducting long-term campaigns such as lack of power supply for instruments, health and safety constrains and limited human resources. Inter-calibration between each set of instruments was achieved by running instruments side by side for 20 to 30 min prior to the beginning and after finishing the measurements. Similar quality control measures were taken in the previous measurement campaign.

To estimate the accuracy of pollutant concentrations among similar instruments, the following quality control activity was implemented. Both sets of monitors were kept side by side for at least 30 minutes prior to and after finishing the air quality measurements. Similar inter-comparison method was performed in previous studies (Lin et al. 2016; Brantley et al., 2014; Abhijith and Kumar, 2019). All instruments set performed well and obtained good agreement on estimating concentration levels (Figure 15). As shown in Figure 15, GRIMMs showed an inter-relation in estimates with  $R^2$  values of 0.84, 0.97, and 0.96 for  $PM_{10}$ ,  $PM_{2.5}$  and  $PM_1$ , respectively. This quality control procedure ensured and validated the detection of pollutant concentration changes between the two monitoring points at each monitoring sites.

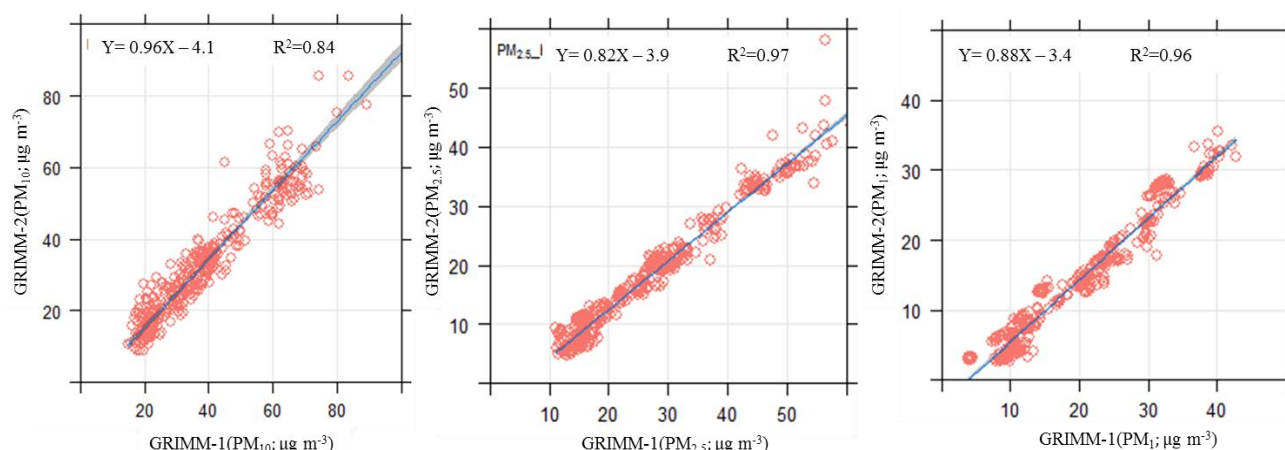


Figure 15: Scatterplots of one instruments measuring the same pollutant. a)  $PM_1$  measurements by GRIMM 11-C on the x-axis and GRIMM 107 on the y-axis, b)  $PM_{2.5}$  by GRIMM 11-C on the x-axis and GRIMM 107 on the y-axis.

### 3.3.3 Quality assurance of citizen sensors

A field study was performed to validate the performance of low-cost sensors by performing a colocation experiment with the high-end instrument at the same site where other filed studies were carried out. For this task, ten Smart Citizen (SC) kits (low-cost sensors; Deliverable 3.1 ‘*High end and low-cost sensing platforms*’<sup>2</sup>) and one GRIMM (high-end instrument) were used. The field experiments were designed to identify errors that could occur when these sensors are deployed for monitoring  $PM_1$ ,  $PM_{2.5}$  and  $PM_{10}$  in real-world conditions. The sampling time was 6 seconds for GRIMM and 30 seconds for SC kits. To maintain consistency in the experiment, the data from GRIMM was averaged to 30 seconds time. Measurements were made for almost 30 hours from 29 October 2018 to 4 November 2018 in Guildford, UK. Some of the SC kits malfunctioned due to sudden battery discharge and anomalous data. After data pre-processing, five hours of continuous data were used to perform the comparative analysis between the GRIMM and SC kits. Although the data for comparison was limited, it captured concentration trends for peak and off-peak period which provided valuable information and a strong metric for comparison. During the data collection, peak hours and off-peak hours concentrations were recorded.

<sup>2</sup> The report will be available on the [iSCAPE website](#)

## Measurement Site and Instrument Setup

The measurement site (51.246495, -0.571539) is located close to a circular intersection and a traffic signal. The instruments, including ten SC kits and one GRIMM, were mounted on a tripod stand and were placed at a typical breathing height of 1.5 meters, as shown in Figure 16. The instruments were placed close to the roadside with a regular inflow of vehicles. The dominant local emission source at the site is vehicle emissions with occasional truck traffic.

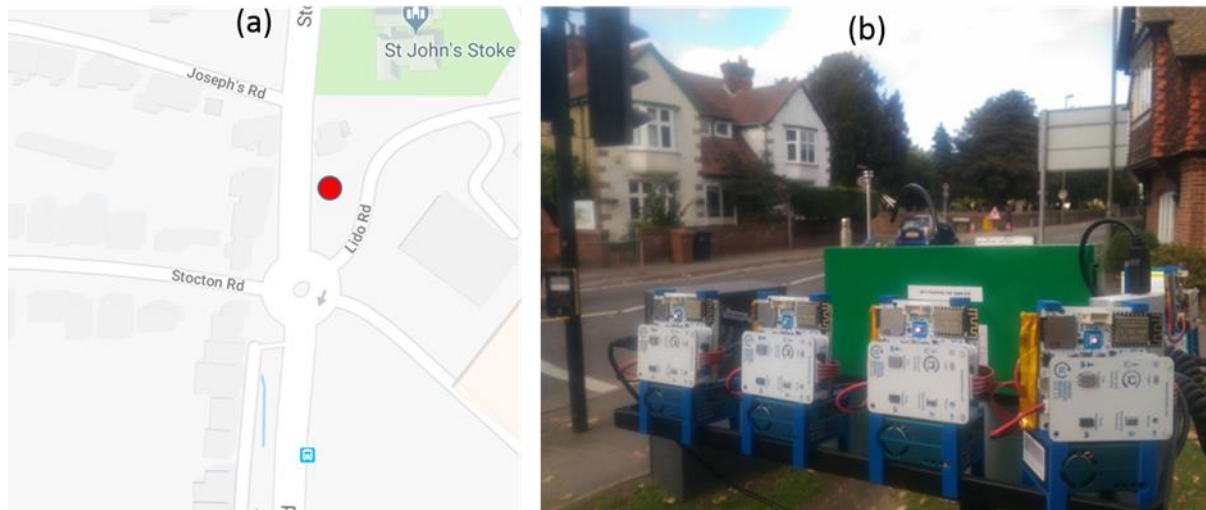


Figure 16: Colocation scenario. (a) The red dot on the map shows the measurement site. (b) View of the SC kits collocated with GRIMM.

## 3.5 Vantaa

The development of GIs embedded on high stores buildings can help both in terms of air pollution mitigation and thermal regulation, enhancing the citizen comfort. It could influence different sources of pollution not necessarily related with vehicular traffic, which is the main focus of the other cities' campaigns. The city of Vantaa was chosen as test case of those interventions due to the mutual presence of different pollutant sources such as the international airport and the location in the Metropolitan Area of Helsinki.

### 3.5.1 Site description

The Vantaa experimental setup consists of two sites in the proximity of each other. Figure 17 shows their location on a map. The first experiment site, Malminiitty, started the monitoring of meteorological variables in April 2018, and lies at the southwest edge of a conglomeration of 20 up to 8 stories high buildings. The site is surrounded by areas of detached houses. The PCS is located in a yard of four 6-storey houses.



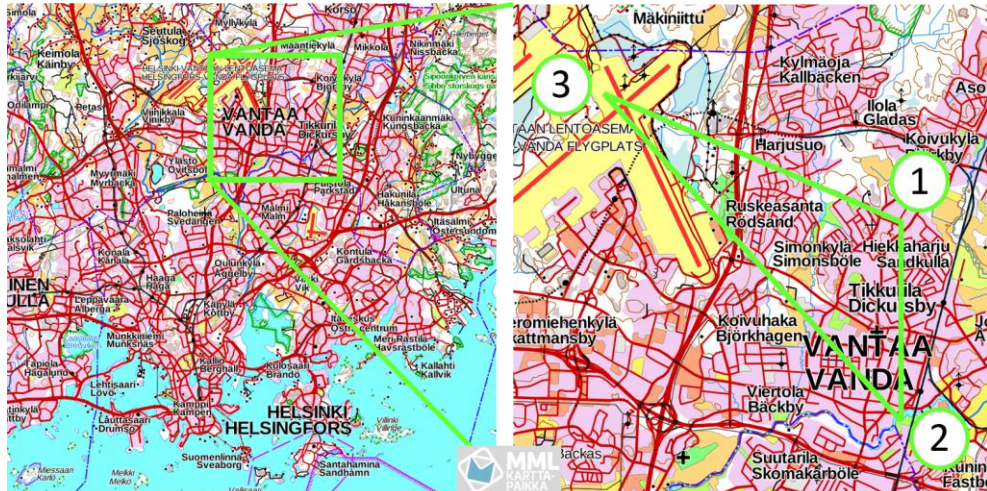


Figure 17: The iSCAPE – Vantaa monitoring stations on a map: 1 = Malminiitty, 2 = Heureka, 3 = Helsinki-Vantaa airport (meteorological reference station).

The courtyard consists of a 1000 square meter green area with a playground for children and 8 different trees and bushes. Some of the trees reach the top of the buildings. This experiment site represents a typical multi-story building Finnish neighborhood. The second site is located at the Finnish Science Center Heureka (<https://www.heureka.fi/?lang=en>) out-door area Galileo, mounted on a 20-meter-high mast, and there the monitoring of meteorological variables started in May 2017.

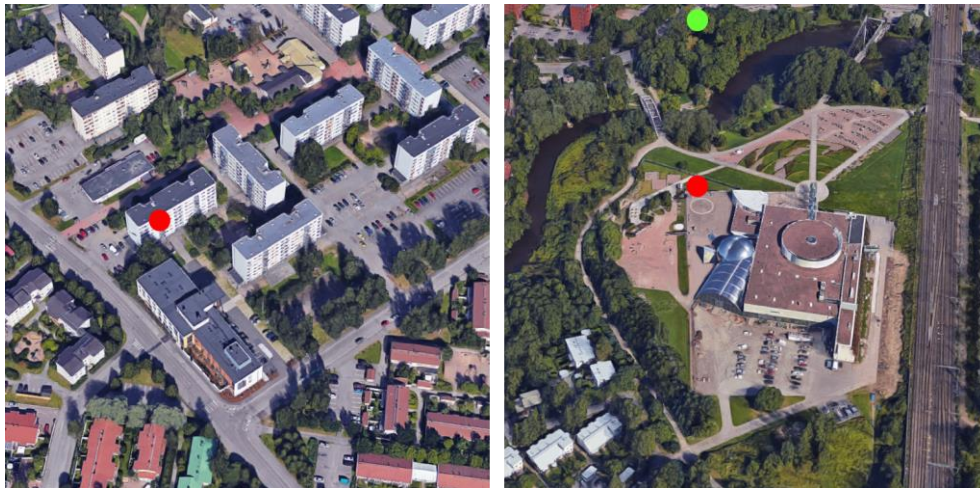


Figure 18: Aerial view of the two monitoring stations: Malminiitty (left) and Heureka (right). Red dots indicate the locations of the instruments, green dot indicates the location of the HSY air pollution monitoring station (source: Google Maps).

The immediate surroundings consist of sand and lawn. The river Kerava flows 50 meters in the north to west. On the riverbank and in the southwest of the experiment site there are deciduous and coniferous trees up to 15 meters height. Beyond the trees, in the southwest, there is an area of detached houses. The next stone multi-story buildings located in north to west are 120 to 150

meters away. The only disturbing building in the proximity is the science center building itself 20 meters to the southeast. Beyond this building lies one of the Finnish main railroads. The experiment site can be considered as an open space park landscape functioning as PCS. The second experiment site is located 2.8 kilometers in the south of the Malminiitty monitoring station. Figure 18 shows the aerial views of both monitoring stations. The densely build-up area of Tikkurila, one of the two mail centers of the City of Vantaa, lies in between the two sites.

### 3.5.2 Instrumental setup

Both sites are equipped with the same instruments (Figure 19). A CNR4 Kipp&Zonen net-radiometer measures the four energy radiation components, the incoming short-wave radiation from the sun, the reflected short-wave radiation from buildings, the ground and other obstacles, the incoming long-wave radiation from the atmosphere, and the out-going long-wave radiation from buildings, the ground, and other obstacles. Wind speed and direction, rain intensity and duration, and air pressure are measured with a Vaisala WXT weather sensor (WXT536). Additionally, air temperature and humidity are measured with thermo-hygrometer sensors according to the standards of the Finnish Meteorological Institute (FMI).

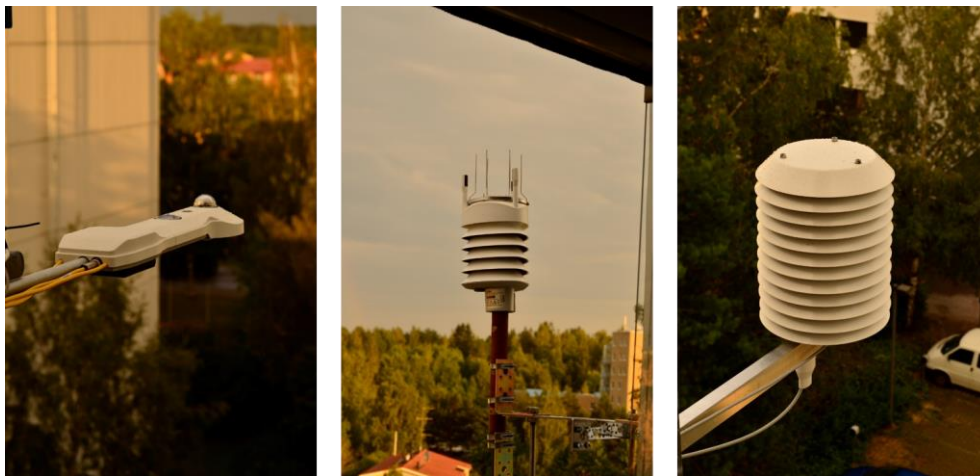


*Figure 19: The iSCAPE Malminiitty monitoring station instrumental setup (from left to right): Kipp&Zonen, CNR 4 net-radiation meter; Vaisala Weather sensor WXT536; FMI standard equipment for air temperature and humidity measurements (all photos by Achim Drebs).*

All instruments are tested and approved for scientific use. At Malminiitty all instruments are mounted at the height of 20 meters on an edge of the outlying balcony to the southeast. The instruments are at least 2 meters away from the wall of the building (Figure 19). At the science center, the net-radiometer and the weather sensor are mounted according to World Meteorological Organization recommendation to the south at the height of 10 meters. Due to the uneven ground, air temperature and humidity are measured at the height of 3 meters (Figure 20). All instruments record their observations every second in real-time to the FMI database. The meteorological data is available for free upon request from the FMI.





Figure 20: The iSCAPE Heureka monitoring station instrumental setup (from left to right): FMI standard equipment for air temperature and humidity measurements; the FMI mounting team and iSCAPE researchers at the time of the installation; the observation mast with the Kipp&Zonen, CNR 4 net-radiation meter and Vaisala Weather sensor WXT536 at 10 m height (all photos by Achim Drebs).

To monitor the quality of the observation data the results were compared on a random basis with the observation of the nearest-by official synoptic weather station of the FMI located at the Helsinki-Vantaa airport. For the air pollution measurements, there is a near-by HSY (Helsinki Region Environmental Service Authority) (<https://www.hsy.fi/en/residents/pages/default.aspx>) official measuring station in Tikkurila, almost 150 meter close to the science center.



Figure 21: The Helsinki Region Environmental Services Authority (HSY) air pollution and environmental monitoring station at Tikkurila, 150 meter north of the science center Heureka, attention: not all sensors were mounted at the time of this picture, see also Figure 17; (all photos by Achim Drebs, 2015).

At this monitoring station, among others, the concentrations of nitrogen dioxide, particles of different sizes and black carbon are measured. The Tikkurila air pollution station belongs to a network of seven permanent and four temporal stations in the Helsinki metropolitan area (Figure 22).

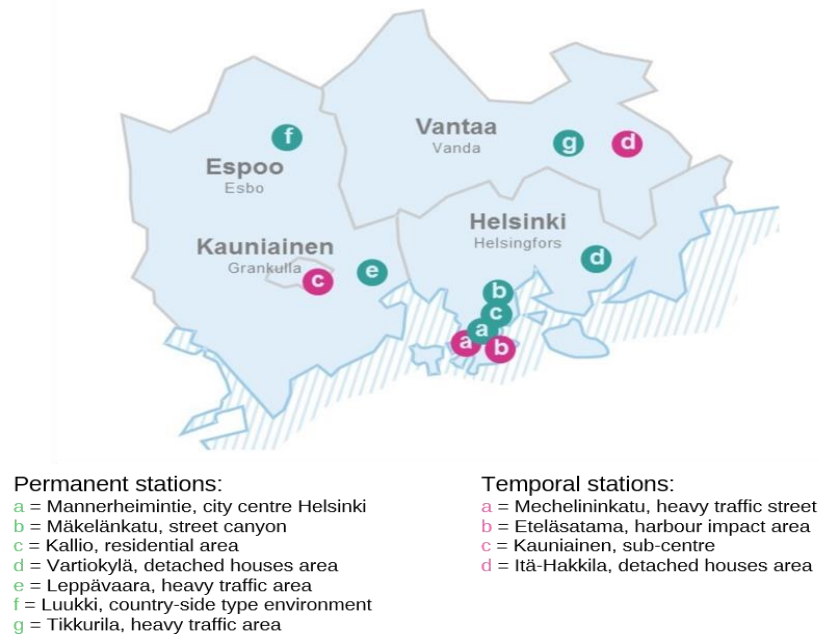


Figure 22: HSY air pollution station network.

### 3.5.3 Experimental protocol and quality check

The use of the same instrumental setup at two experimental sites enabled for cross-comparison of the data collected at the two sites. As for the meteorological observations, it was assumed that the differences between the two sites in the overall averages were negligible. However, in the case of single meteorological parameters like different cloudiness, heavy rain, and strong wind conditions, the differences should be perceptible. All these events need to be cross-checked with the official FMI weather observations. Furthermore, the meteorological observations were compared with modelled results for selected areas in Heureka, Tikkurila, and Malminiitty.

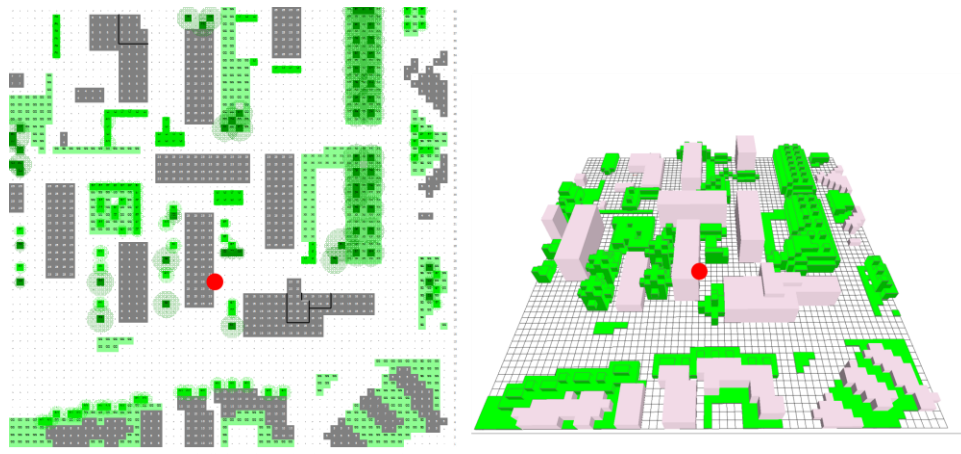


Figure 23: iSCAPE Malminiitty built-up area, left 2-D model, right 3-D model, red dot: iSCAPE – monitoring stations (models by Achim Drebs and ENVI-met v4).

The meteorological and air pollution data were used as an input into the ENVI-met simulation software (<http://www.envi-met.com>) presented in D6.3 and in upcoming D5.3 (*'Evaluation of interventions'*). ENVI-met v4 is a holistic three-dimensional non-hydro static model for simulations of surface-plant-air interactions with a horizontal resolution from 0.5 to 5 meters (Huttner and Bruse, 2009). Simulation runs were executed for the surroundings of the two iSCAPE - monitoring station Malminiitty (Figure 23) and Heureka (Figure 24).

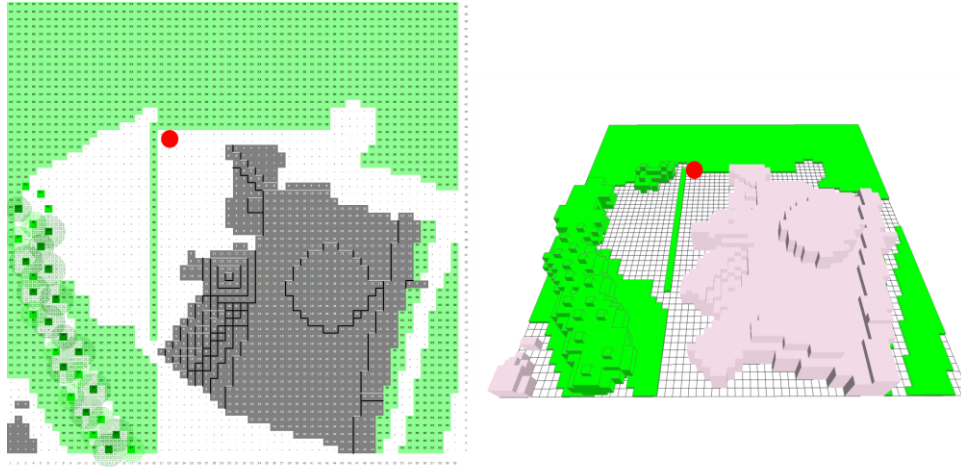


Figure 24: iSCAPE Heureka open area, left 2-D model, right 3-D model, red dot: iSCAPE – monitoring stations (models by Achim Drebs and ENVI-met v4).

During three Heureka summer camp weeks in July/August 2018 a thermal sensation questionnaire was carried out to find out about the children impressions of their environmental surroundings. During these weeks, one day with more or less clear sky conditions was chosen for the questionnaire. The questionnaire was executed twice during the day selected.

The main findings achieved by the questionnaire are shown in Figure 25 and Figure 26. The science campaign period was dominated by hot summer days, with mostly clear skies. The majority of the answers regarding thermal sensations fall in the categories of “Fair” to “Comfortable”. Interestingly, on Aug 2 an increase in the relative humidity during the local afternoon is observed: this coincides also with a peak in the answers in the thermal comfort falling in the “Really uncomfortable”.

To conclude, this simple demonstration revealed that it is possible and relatively easy to collect comfort-related information from citizens, and that this information can be used to carry on intercomparisons with various kinds of meteorological observations.

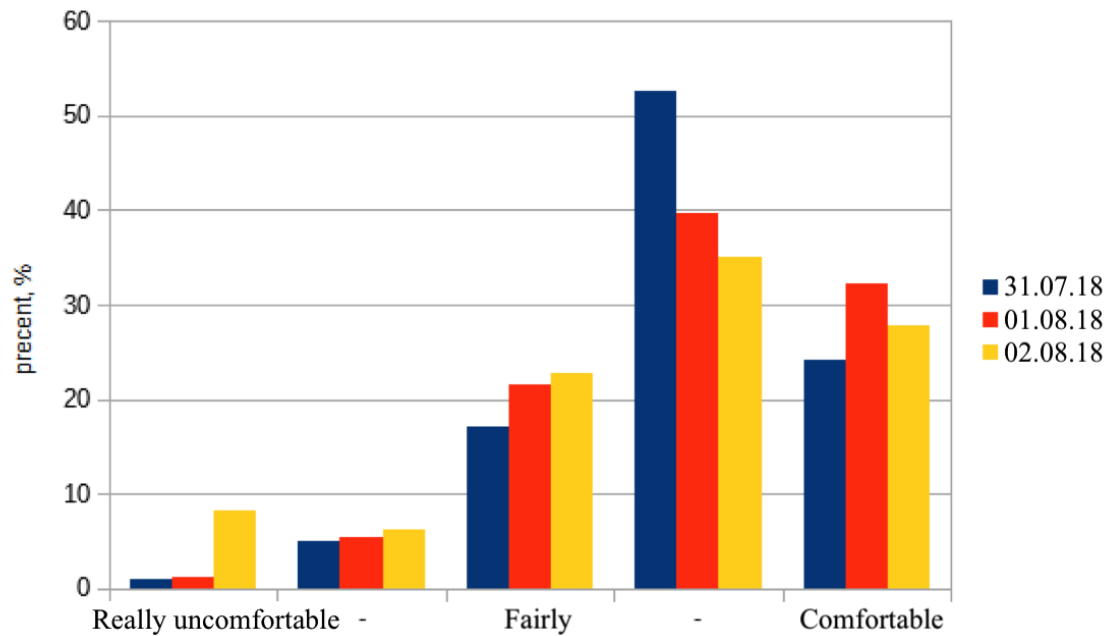
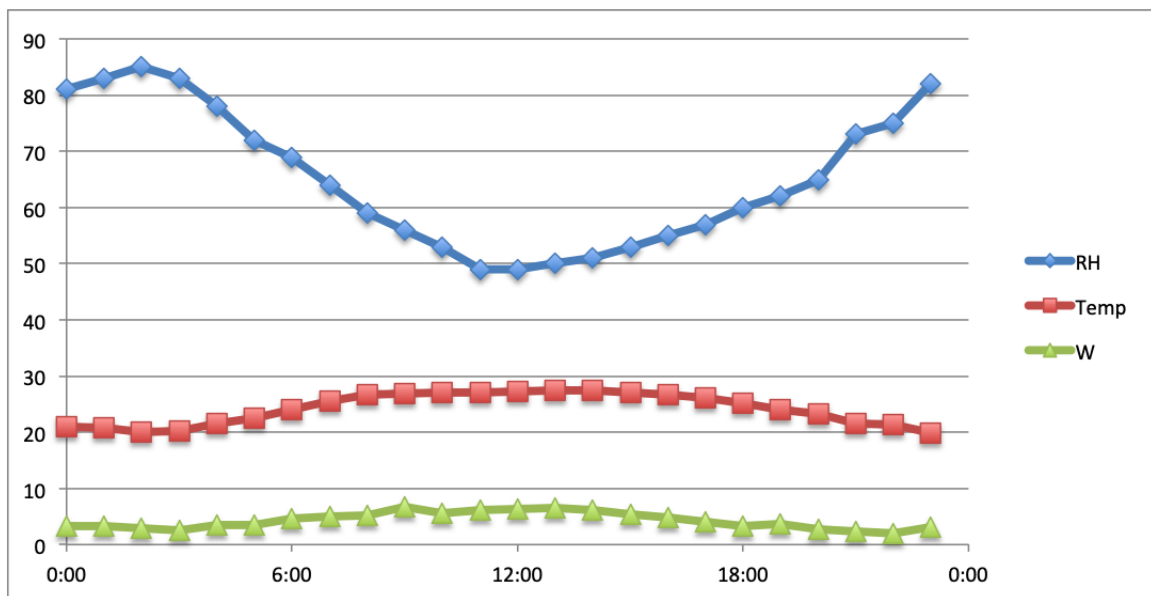


Figure 25: Summary of the statistics of the 3-day Heureka summer camp questionnaire, 31/07 – 2/8/2018.





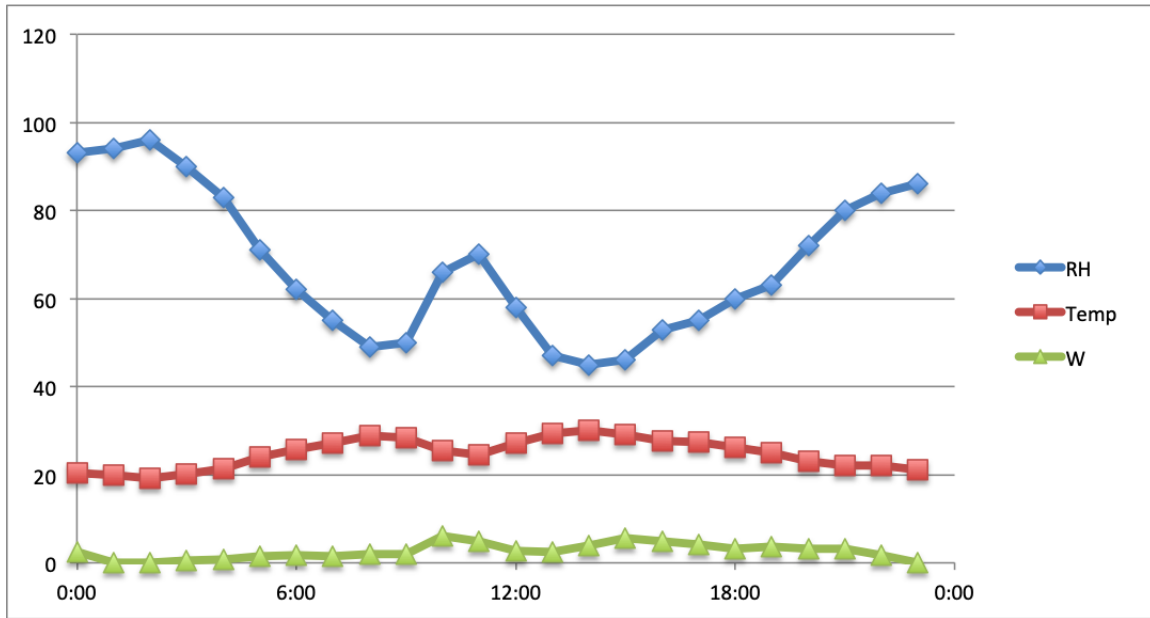


Figure 26: Hourly mean temperature (Temp, °C), relative humidity (RH, %) and wind (m/s) for the Heureka campaign days July 31 (upper) and Aug 2 (lower).

## 4 Environmental impact data

Section 3 described the setup of the various campaign within the project in terms of site description, instrumentations setup and protocol of usage, as well as the data quality check to ensure the reliability of results. All this information defines the baseline to understand the analysis of collected data under the monitoring campaigns reported in the current section. Air quality data are strongly influenced by the environmental conditions: once the site morphology is set, the analysis of meteorological data is crucial to define transport and dispersion phenomena related to pollutant, as well as to identify the most suitable conditions where PCSs might have a mitigating impact. Therefore, in the current section, a detailed analysis of environmental (meteorological and air quality) results obtained so far is reported and described for each pilot city.

### 4.1 Bologna

#### 4.1.1 Boundary Layer Height Analysis

The phenomenon of pollutant dispersion is strictly related to the Planetary Boundary Layer (PBL), or rather the portion of the troposphere that is directly influenced by the presence of the earth's surface and responds to surface forcing with a timescale of about an hour or less (Stull, 1988). The atmospheric level of the interface between PBL and free atmosphere is known as PBL height. This quantity is fundamental especially for atmospheric modelling and weather forecasting, because it defines the height at which the unperturbed large-scale flow begins to be perturbed by the ground. These perturbations affect both momentum and energy associated to the flow, by means of friction forces, heat and humidity release from the surface (soil and ocean). The results of those interactions modify the two-dimensional nature of the flow into a three-dimensional turbulent flow whose mean path depends on the topology of the surface. In this framework the

information and knowledge of the PBL height is therefore fundamental to distinguish these two different flow types.

When dealing with local circulation or pollutant dispersion problems, the knowledge of the PBL height provides information about the characteristics and intensities of ground-to-atmosphere exchange phenomena and the atmospheric depth available to them. In particular, radiative, latent and sensible heat exchanges between ground and atmosphere determine the characteristics of the boundary layer and therefore its height. The result is a time dependency of the boundary layer characteristics and depth. During daytime, when the ground is warmer than the atmosphere, surface heat transfer warms the boundary layer generating strong mixing which extends up to 2-3 km. During night, the atmospheric cooling tends to lower the boundary layer height to several hundreds of meters, suppressing the turbulence. A schematic representation of the diurnal cycle of the boundary layer is shown in Figure 27.

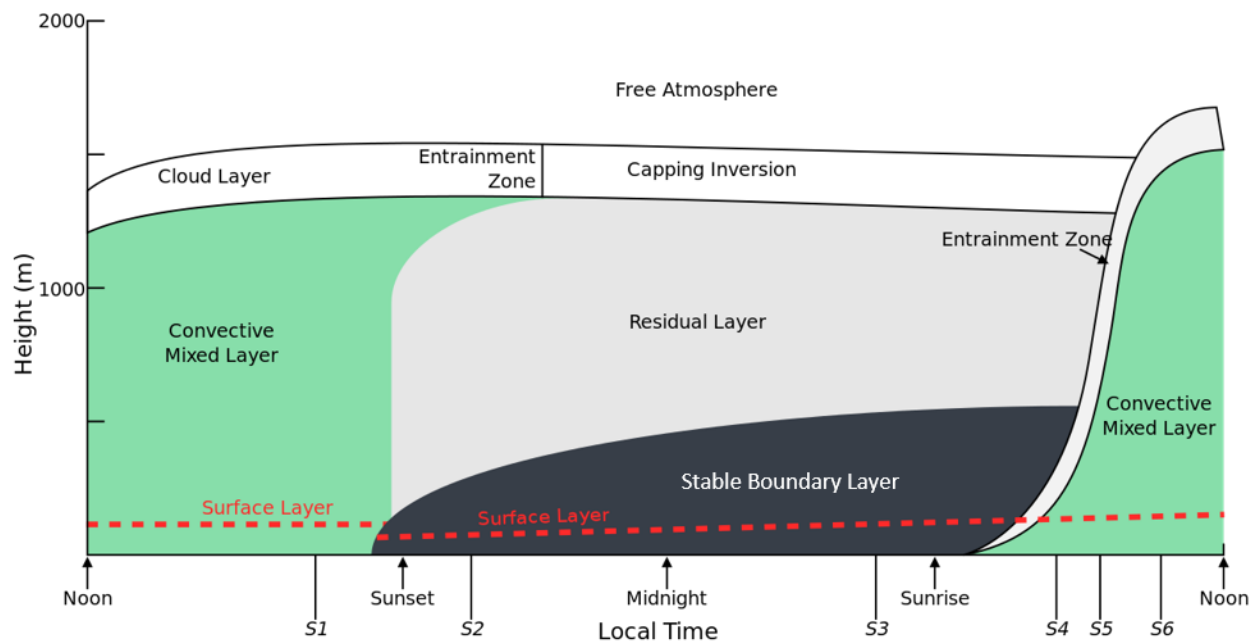


Figure 27: Diurnal cycle of the planetary boundary layer over land in condition of large-scale high pressure (modified from: Stull, 1988).

The major components of the diurnal cycle are the Convective Mixed Layer (or Convective Boundary Layer, CBL), the Stable Boundary Layer (SBL) and the Residual Layer (RL). The CBL is a well-mixed layer due to convection forces. In clear sky conditions, radiative and heat transfers from the ground create a sublayer of warm air rising from the surface while, in the presence of clouds, radiative cooling also enhances mixing by lowering cool air from the cloud top. The result is an unstable layer where heat, moisture, momentum and even mass are uniformly distributed along the vertical by turbulent structures, from above the Surface Layer (SL) to the entrainment zone (or cloud layer if any). The SL is an all-day-long sublayer at direct contact with the ground where the turbulent fluxes vary less than 10% of their magnitude and its depth is almost the 10% of the boundary layer depth (CBL or SBL). The entrainment zone is the interface between the CBL and the free atmosphere above and behaves as a vector for exchange processes with the free atmosphere. In certain conditions, the entrainment zone shows the same characteristics of a stable layer, behaving as a lid to the CBL growth (in fact a stable layer inhibits convection, i.e.

vertical motions), confining air pollution in the lower atmosphere. CBL starts growing after sunrise and, in clear sky conditions, reaches its maximum depth at late afternoon.

Approaching the sunset, the convection becomes less intense until it ceases to support the CBL since there is no more positive thermal forcing from the ground, allowing turbulence to start decaying. This decaying state of the CBL is the RL, which contains all the suspended particles to light to fall for gravitational deposition and too heavy to penetrate the stably stratified layer growing beneath during night. Being a decaying layer, the RL depth is maximum at sunset and decays during the night as the SBL grows beneath it.

The SBL is a stable layer which grows during night as the atmosphere loses heat to the ground, becoming more stably stratified (increasing the vertical temperature gradient in the layer). In this condition, turbulence is suppressed but supergeostrophic winds (flows with velocity larger than geostrophic winds) can develop allowing the formation of intermittent mechanical turbulence. This condition suppresses vertical motions, trapping pollutants in the lower portion of the atmosphere at direct contact to the ground. The SBL starts growing as the CBL cut-off of convection and continuously grows until sunrise when a new CBL starts developing. Nevertheless, as long as the ground is colder than the air, the SBL can also form during daytime, as during winter periods causing severe issues for air quality.

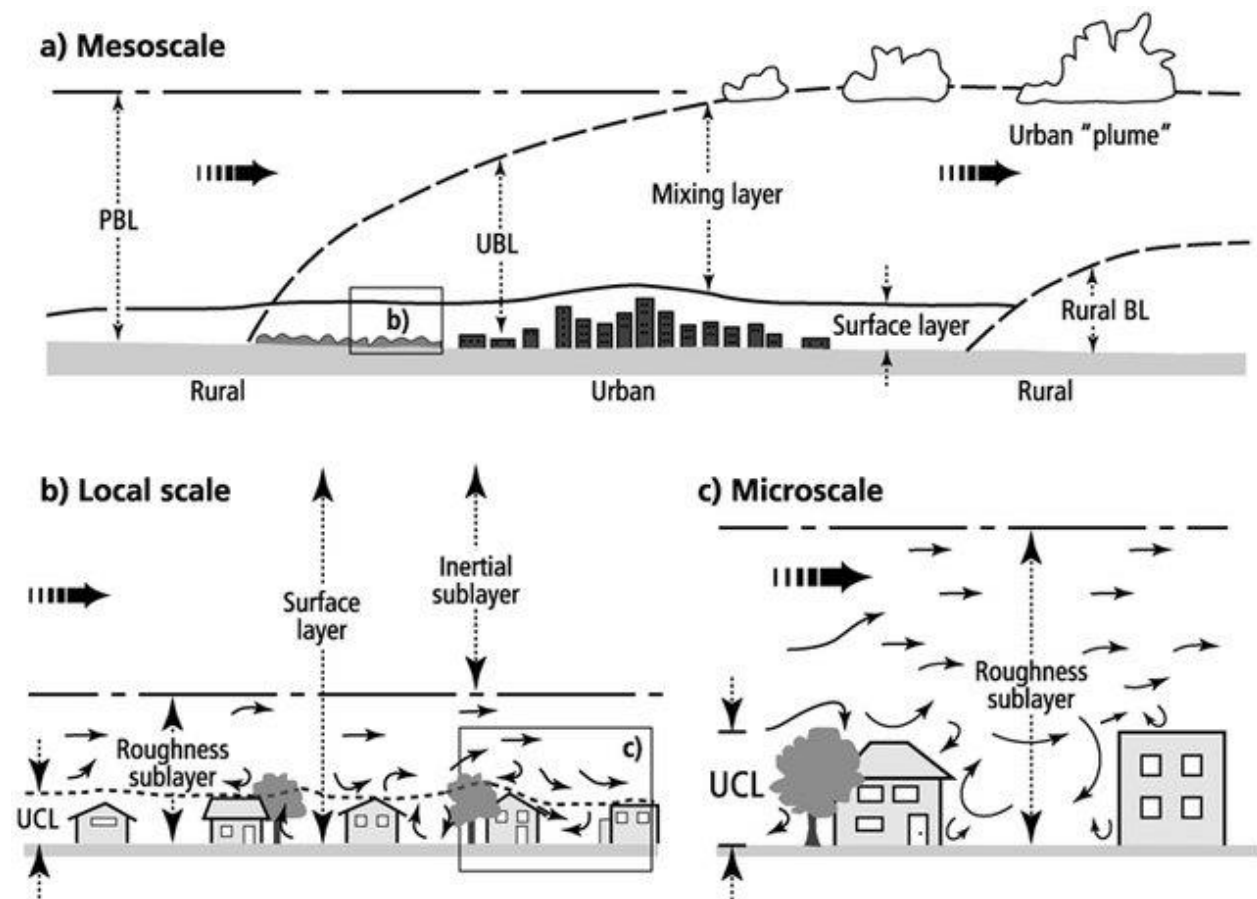


Figure 28: Structure of the urban boundary layer (Source: 2002, originally Oke et al., 1997).

The presence of an urban environment modifies the diurnal cycle of the boundary layer, since it changes the structure of the PBL and therefore the phenomena characterizing it. Both wind profile (Britter and Hanna, 2003) and thermal budget (Grimmond and Oke, 2002) are modified by the presence of obstacles (buildings, vegetations) at surface. This modified boundary layer is called Urban Boundary Layer (UBL), it develops into the whole CBL or SBL (Oke, 1997) and it is composed of three separated sublayers (Rotach et al., 2004): the Urban Canopy Layer (UCL), the Inertial Sublayer (ISL) and the Roughness Sublayer (RSL), shown in Figure 28. The ISL is the boundary layer depth where the atmospheric properties have adapted to the presence of the underlying urban surface and it is treated as an unperturbed boundary layer (Britter and Hanna, 2003). It extends from the top of the SL to the height at which the RSL starts, i.e. where the flow is adjusting from the perturbation generated by the obstacles (Britter and Hanna, 2003). The UCL is the layer where the flow is directly perturbed by the obstacles. It ranges from the ground to the mean height of the obstacles, or more accurately it follows the rooftop shape. Inside the UCL, the mean wind profile behaves differently from the common PBL profile, accounting for the morphological restrictions. Turbulence becomes a fundamental carrier of momentum, heat, moisture and mass transport both vertically and horizontally along and outside the city. Thermal forcing is enhanced by the storing capacity of buildings and streets and modify the thermal budget. Obstacle friction also changes the complexity of turbulent structures by increasing the mechanical turbulence.

In this context it becomes important to retrieve the PBL height in order to indirectly characterize the vertical structure of the atmosphere beneath it to better deal with air quality issues.

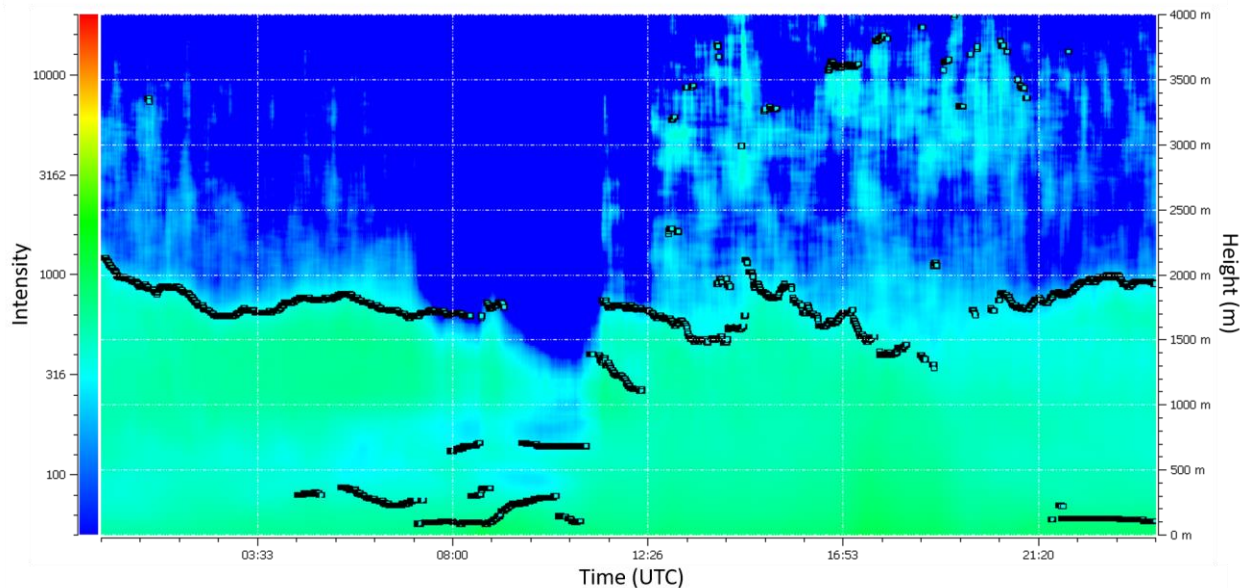


Figure 29: Boundary layer height retrieved from ceilometer data at Irnerio St. 46. Summer daily cycle, 23/08/2017.

Figure 29 shows the diurnal cycle of the boundary layer height measured during the summer campaign by the ceilometer located on the rooftop of the Physics and Astronomy Department of the University of Bologna, Irnerio St., 46 (the instrumental setup is thoroughly described in the first version of this Deliverable). The left label depicts the intensity of the signal retrieved by the

instrument, while the right label shows the PBL height. Basically, this instrument derives the PBL height from the backscatter signal originating from an emitted laser beam.

The diurnal cycle in Figure 29, depicting the diurnal PBL height cycle on the 23<sup>th</sup> August 2017, i.e. during the summer intensive thermographic field campaign in Bologna, shows a completely different behavior with respect to the evolution of the PBL previously described. It depicts an overall steady state condition of the boundary layer, except during the hours around sunrise and sunset. The 2000m depth of the boundary layer is in agreement with what is usually retrieved for the CBL, while at transition times (sunrise and sunset) the behavior corresponds more readily to SBL heights. The larger and steady depth is typical of summer days and especially of high-pressure periods. In fact, under this situation, during night, the heat release from the city allows the vertical mixing which sustains the layer depth. The transitional nature of sunrise and sunset have an impact of the boundary layer depth since ground and atmosphere must adjust to the presence or absence of solar radiation presence or lack.

Figure 30 shows instead a winter daily cycle of the boundary layer height. The time evolution shows the characteristics of the SBL during the whole night and during the morning, due to the presence of a low-level cloud that obscures the vertical signal between 6 am and 12 pm, confining the boundary layer to 500m height. In the afternoon the renewed clear sky conditions allow the CBL to grow until reaching the 1000m height late in the evening. The growth of the CBL only during the afternoon is a common feature of winter periods but its persistence in the late evening is again a consequence of the heat release from the city after sunset.

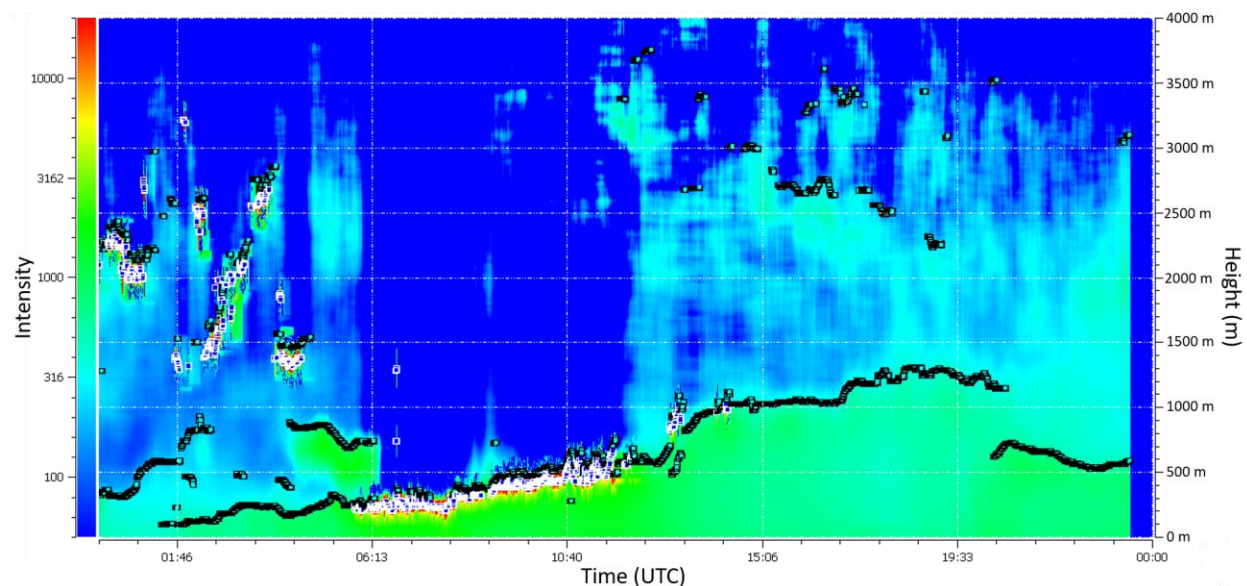


Figure 30: Diurnal cycle of boundary layer height retrieved from ceilometer data at Irnerio St. 46. Winter daily cycle, 31/01/2018.

The conditions depicted in Figure 30 are also disadvantageous for air quality. In fact, the sustained limitation of the boundary layer within the first 500m during the whole night and morning inhibits the vertical dispersion of the pollutants, which remain trapped inside the urban texture and increase their concentrations because of their accumulation also due to the increasing emissions especially during and after the morning rush hours. This is readily shown by Figure 31 depicting

the diurnal cycle of  $\text{NO}_x$  hourly concentrations measured during the same day at the two Bologna street canyons and at ARPAE urban traffic and urban background air quality stations of Porta San Felice and Giardini Margherita. The plot shows the same pattern at all the sampling sites including the urban background, with increasing and particularly high concentrations during rush hours, a condition which is exacerbated during the morning by the limited PBL height previously observed.

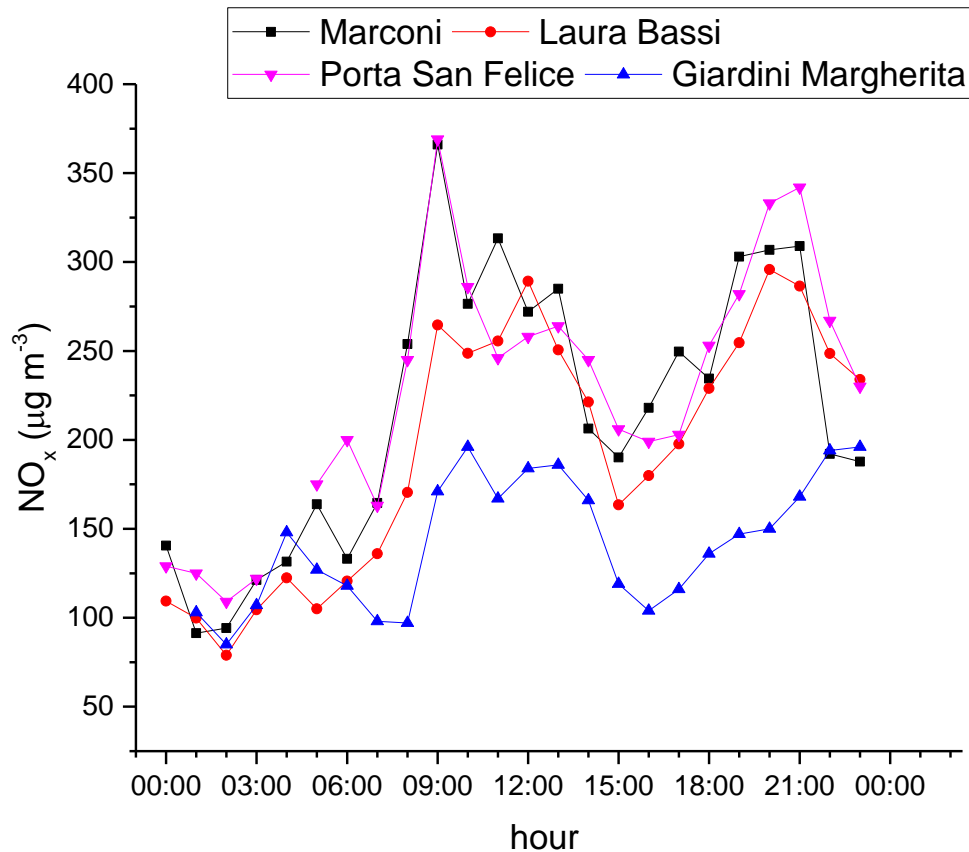


Figure 31. Diurnal cycle of  $\text{NO}_x$  hourly means concentrations measured in the two Bologna street canyons (Marconi and Laura Bassi) and at ARPAE urban traffic (Porta San Felice) and urban background (Giardini Margherita) air quality stations on 31/01/2018.

Conversely, the pattern of hourly estimated  $\text{PM}_{10}$  and  $\text{PM}_{2.5}$  concentrations (Figure 32), retrieved from the data measured with the two optical particle counters in the two street canyons, with a methodology described and verified against daily PM observations in the previous version of this Deliverable, shows that the accumulation of PM, though also linked with the diurnal evolution of the PBL, seems to be driven by other local processes acting simultaneously on both coarse and fine particles leading to different patterns in the two street canyons and to higher accumulations in Laura Bassi than in Marconi street canyon.



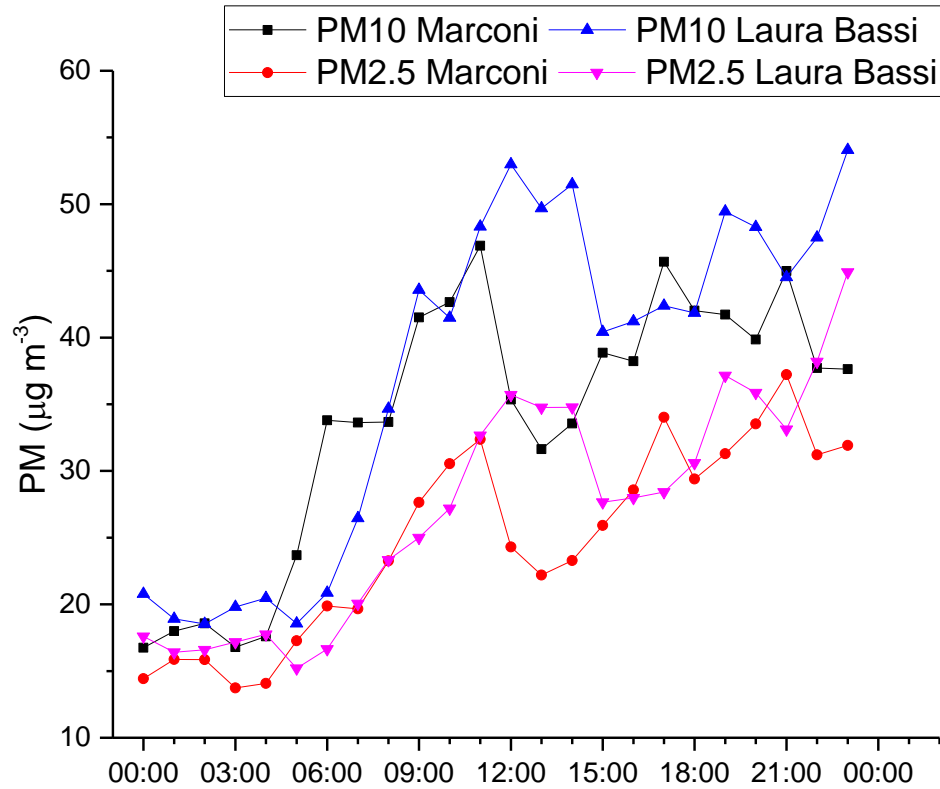


Figure 32. Diurnal cycle of estimated PM ( $PM_{10}$  and  $PM_{2.5}$ ) concentrations derived from the observations of the two optical particle counters deployed at the two street canyons during the winter 2018 experimental campaign in Bologna.

#### 4.1.2 Influence of GI on air pollution

Differently than in the other cities, observations from the summer and winter campaigns in Bologna were primarily utilized to verify the simulations conducted at neighborhood and urban scale in WP4 and WP6. In particular, the evaluation of the effect of GI on air quality and thermal comfort was conducted through the output of these simulations. In this and in the previous version of this Deliverable, however, we present some preliminary indications on the effect of GI on air quality (this version) and on thermal comfort (previous version) in urban street canyons as resulting from the observations of the two experimental campaigns.

As reported in the first version of this Deliverable, the differences in air pollutant concentrations between the two Bologna street canyons, also shown in the previous section, are not only due to the different presence of vegetation but are largely determined by the different morphologies, traffic volumes and vehicle types travelling in the two street canyons.

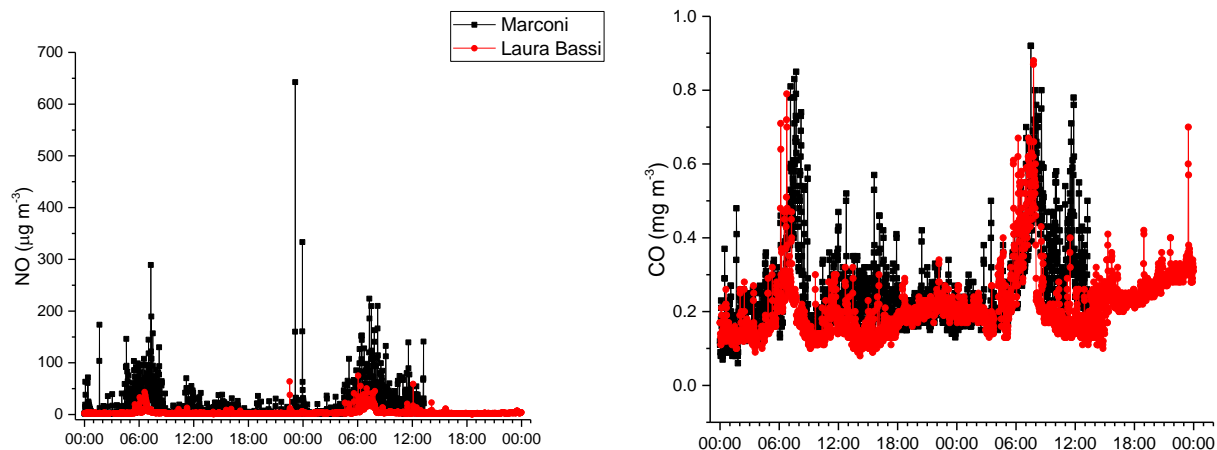


Figure 33:  $\text{NO}_x$  and CO concentrations observed with a 1-min time resolution in the 2 street canyons in Bologna during the intensive thermographic summer campaign (22-23/08/2017).

Figure 33 readily shows that measured concentrations at 1-minute time resolution shows frequent spikes, mostly at Marconi, connected with the transit of vehicles in the canyon. Even averaging data acquired with 1-minute time resolution to 30-minutes time averages (Figure 34), data continue to show common morning spikes, probably linked to traffic rush-hours.

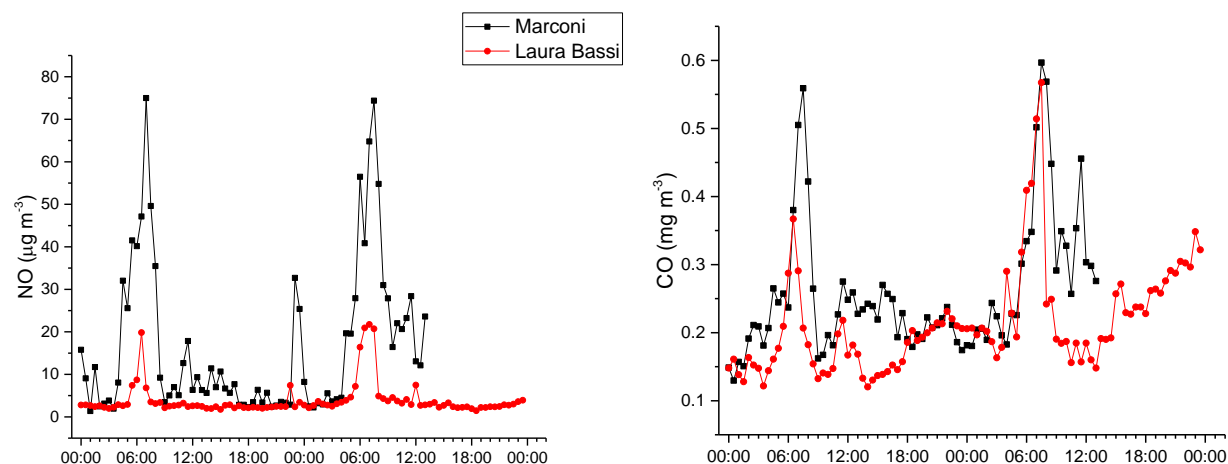


Figure 34: 30-minutes averaged  $\text{NO}_x$  and CO concentrations in the 2 street canyons in Bologna during the intensive thermographic summer campaign (22-23/08/2017).

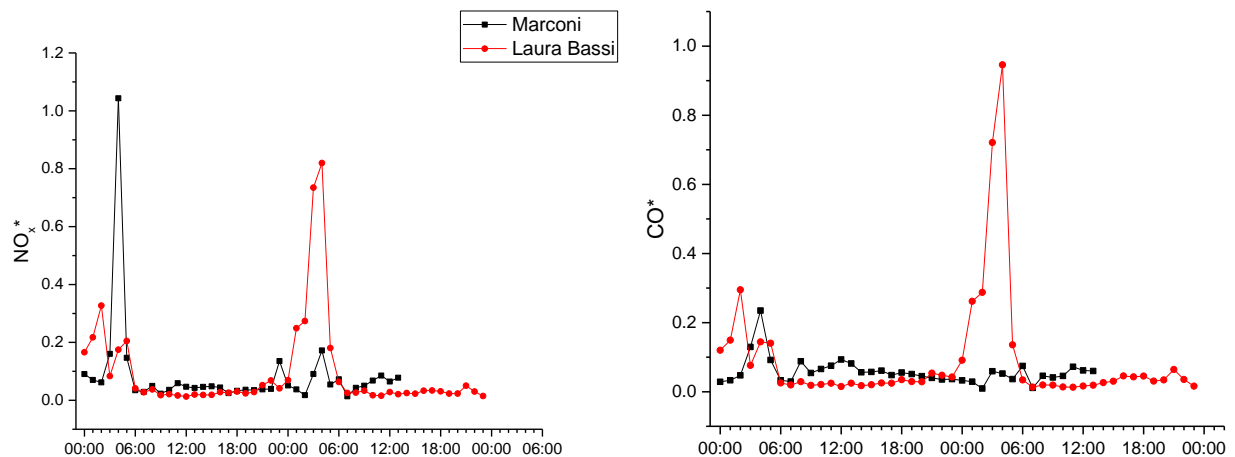
In order to remove the effect of other confounding factors and to analyze the effect of GI on air pollution, an algorithm was developed to normalize the concentrations observed in the two street canyons. The normalization algorithm takes into account the morphology of the two canyons, the wind speed observed above the two canyons (bulk velocity), and the traffic emissions, as estimated by the traffic counts available from the Municipality of Bologna for the two street canyons. In particular, similar to Kubilay et al. (2017), concentrations were normalized with a reference concentration in the two canyons defined as:

$$C_0 = \frac{Q_e}{HWU_b}$$

Where  $Q_e$  = pollutant source rate [g/s],  $U_b$  = bulk velocity [m/s],  $H$  = building height [m],  $W$  = street canyon width [m]. In particular, bulk velocity was derived from the measurements of the sonic anemometers placed on the rooftops in the two street canyons, while the average building height and street canyon width were estimated from detailed digital maps of the two areas.

The development of the normalization algorithm then involved the estimate of the pollutant source rate starting from available traffic counts available as number of vehicles travelling in the two street canyons with a 5-minutes time resolution from inductive loops technology. In particular, it was therefore necessary to derive emissions estimating the traffic counts per each vehicle type (i.e., fuel type, vehicle category and EURO technology). To estimate the pollutant source rate, it was necessary first of all to derive the number of buses travelling in the two street canyons from the bus time schedules in Bologna, available from the regional transport company TPER (Trasporto Passeggeri Emilia Romagna) through their website<sup>3</sup>. The local fleet composition was then extracted from the regional inventory of circulating vehicles, available on the web as open data<sup>4</sup> from the Italian Car Club company (ACI, Automobile Club d'Italia) and was used to disaggregate the difference between the total traffic counts and the number of buses derived from bus schedules into traffic counts per vehicle type. Pollutant emission rates [g/km] were then finally estimated using the joint EMEP/EEA (European Monitoring and Evaluation Programme/European Environment Agency) air pollutant emission inventory guidebook for each vehicle category (EEA, 2017). Finally, pollutant source rate  $Q_e$  was estimated from pollutant emissions using a representative vehicle urban speed of 19km/h (EEA, 2017). This approach was conveniently exploited in Barbano et al. (submitted) to investigate the role of turbulent transport as a key mechanism of ventilation in urban street canyons.

The comparison of normalized  $\text{NO}_x$  and CO concentrations (Figure 35) shows that in general lower concentrations are observed in Laura Bassi, though the existence of contemporary spikes suggests the existence of common forcings acting on the two sites but independent on the traffic source.



<sup>3</sup> <https://www.tper.it/o> (in Italian, last accessed 19/03/2019)

<sup>4</sup> <http://www.aci.it/laci/studi-e-ricerche/dati-e-statistiche/open-data.html> (in Italian, last accessed 19/03/2019)

Figure 35: 1-hour averaged  $\text{NO}_x$  and CO normalized concentrations in the 2 street canyons in Bologna during the intensive thermographic summer campaign (22-23/08/2017).

The comparison of 30-minutes averaged normalized concentrations in the 2 street canyons during the period 21-25/09/2017 of weak synoptic forcing (see first version of this Deliverable) shows common patterns in the two canyons, probably related to boundary layer height dynamics (see previous section), with lower concentrations observed in the Laura Bassi street canyon.

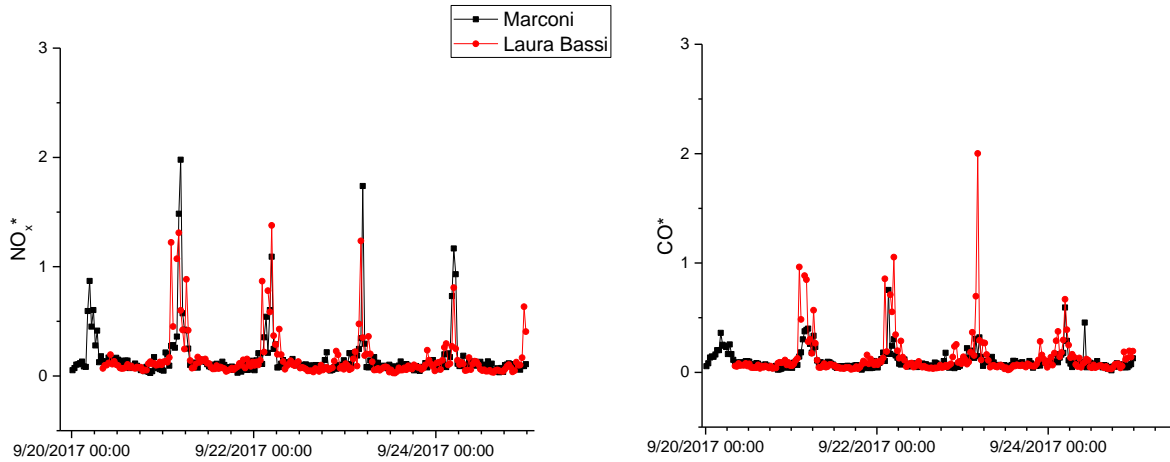


Figure 36: 30-min averaged  $\text{NO}_x$  and CO normalized concentrations in the 2 street canyons in Bologna during the 20-26/09/2017 period of weak synoptic forcing within the summer 2017 experimental field campaign.

On average, the pollutant removal efficacy, as calculated by the difference between normalized concentrations in the two street canyons normalized over the normalized concentration in Marconi street canyon (Figure 37), was equal to -0.23 and -0.10 for  $\text{NO}_x$  and CO, respectively.

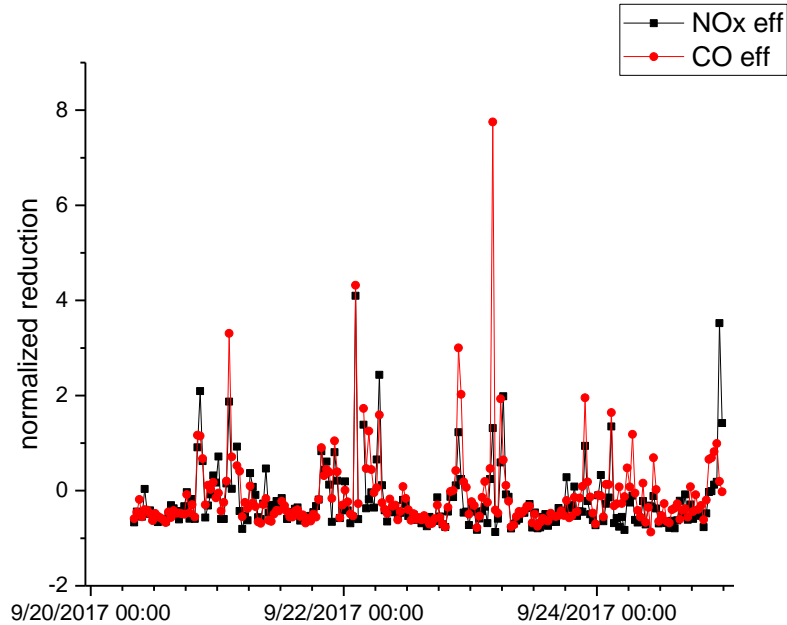


Figure 37: NO<sub>x</sub> and CO pollutant removal efficacy calculated as the difference in normalized 30-min averaged NO<sub>x</sub> and CO normalized concentrations in the 2 street canyons in Bologna during the 20-26/09/2017 period of weak synoptic forcing within the summer 2017 experimental field campaign.

The analysis of the pollutant removal efficacy dependence on wind direction (Table 4) shows that on average reductions during the period considered (19-26/09/2017) were higher under upwind and secondarily parallel anabatic flows; however, it can be noted that parallel katabatic flows, which represent the majority of the flows together with anabatic flows as typical of thermal circulation developing under weak synoptic forcing, were characterized by the largest variabilities and might account for the maximum reductions. This is also readily shown by the two polar plots representing the pollutant removal efficacy as a function of wind speed and directions (Figure 38).

	NO <sub>x</sub> eff					CO eff			
	N	Mean	std	min	max	mean	std	min	max
parallel anabatic	53	-0.49	0.22	-0.79	0.28	-0.46	0.26	-0.87	0.69
parallel katabatic	92	-0.04	0.82	-0.87	4.10	0.25	1.18	-0.78	7.75
upwind	19	-0.54	0.19	-0.79	-0.13	-0.49	0.18	-0.77	-0.02
downwind	53	-0.32	0.43	-0.83	1.42	-0.21	0.50	-0.78	1.64

Table 4. Descriptive statistics ( $N$  = number of cases, mean, std = standard deviation, min = minimum, max = maximum) for NO<sub>x</sub> and CO pollutant removal efficacy under the different wind conditions in Bologna, as measured at the Bologna airport synoptic meteorological station.

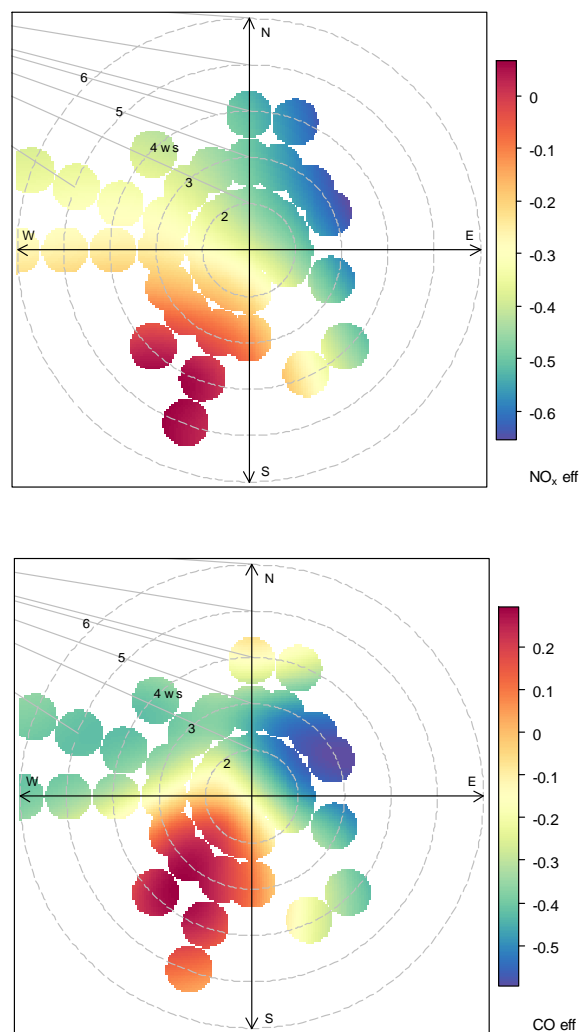


Figure 38. Polar plots showing  $\text{NO}_x$  and CO pollutant removal efficacy, as obtained from the difference in the ratio between normalized concentrations at Laura Bassi and Marconi and normalized concentration in Marconi, as a function of wind speeds and directions in Bologna measured at the Bologna airport meteorological station in the week of 19-26/09/2017.

Winter pollutant removal efficacy, calculated also on 30 minutes averaged normalized concentrations for consistency with the summer case, was instead reduced for  $\text{NO}_x$  and CO pollutants, probably due to the absence of foliage on trees during the cold period and in agreement with, e.g., Nowak et al. (2006) who concluded that trees remove gaseous air pollution primarily by uptake via leaf stomata. However, as previously observed in the winter case the deployment of the two optical particle counters in the two street canyons provided the possibility to estimate also sub-daily variations of PM concentrations, with a methodology presented and verified against PM daily concentrations measured by ARPAE mobile laboratories in the previous version of this Deliverable. As such, in the winter case, also  $\text{PM}_{2.5}$  normalized concentrations could be estimated with the same methodology previously discussed, considering  $\text{PM}_{2.5}$  emission factors reported by the EEA inventory, while PM coarse emissions in exhausts are considered negligible and thus not adequately estimable through this technique. The  $\text{PM}_{2.5}$  removal efficacy, calculated as the ratio between the difference in normalized  $\text{PM}_{2.5}$  concentrations at the two street canyons and that



estimated at Marconi St. during the intensive thermographic experimental campaign was on average equal to -0.59, i.e. far higher than that estimated for NO<sub>x</sub> and CO. Although this exceptional result was obtained only considering 2 days and should be confirmed by other measurements, the higher efficiency of trees to remove particulate than gaseous pollutants clearly depends on the ability of trees to remove particulate pollution by interception, in agreement with previous studies (e.g., Nowak et al., 2006; Beckett et al., 2012; Janhäll et al., 2015).

While PM<sub>2.5</sub> reductions are spread all over the wind directions, it can be noted that PM<sub>2.5</sub> increases are mostly located in the 210-270° range, corresponding to a katabatic SW direction from the hills (Figure 39). The polar plots (Figure 40) show that the largest pollutant reductions are observed under S-SW wind directions.

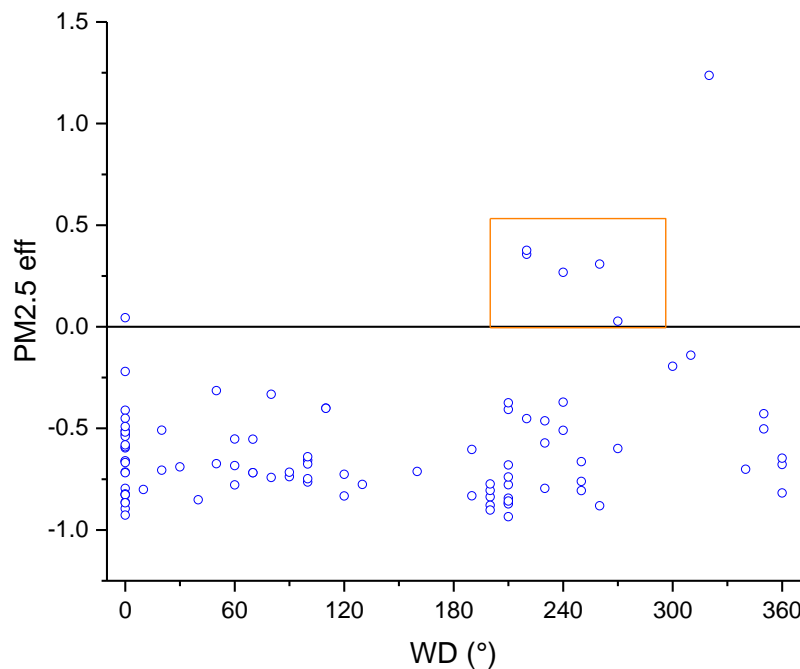


Figure 39. Relationship between PM<sub>2.5</sub> removal efficacy and wind direction in Bologna, as measured at the Bologna synoptic meteorological station.

		NOx eff				CO eff				PM eff			
	N	mean	Std	min	max	mean	std	min	max	mean	std	min	max
<b>parallel anabatic</b>	44	-0.04	0.73	-0.92	3.27	-0.64	0.20	-0.90	0.02	-0.64	0.19	-0.93	0.04
<b>parallel katabatic</b>	30	-0.05	1.08	-0.91	3.24	-0.70	0.14	-0.89	0.38	-0.60	0.36	-0.93	0.38
<b>upwind</b>	17	-0.25	0.31	-0.63	0.43	-0.67	0.16	-0.83	-0.33	-0.64	0.14	-0.78	-0.33
<b>downwind</b>	10	0.50	1.42	-0.86	3.02	-0.56	0.31	-0.81	1.24	-0.25	0.66	-0.88	1.24

Table 5. Descriptive statistics (N = number of cases, mean, std = standard deviation, min = minimum, max = maximum) for NO<sub>x</sub>, CO and PM<sub>2.5</sub> pollutant removal efficacy under the different wind conditions in Bologna, as measured at the Bologna airport synoptic meteorological station.

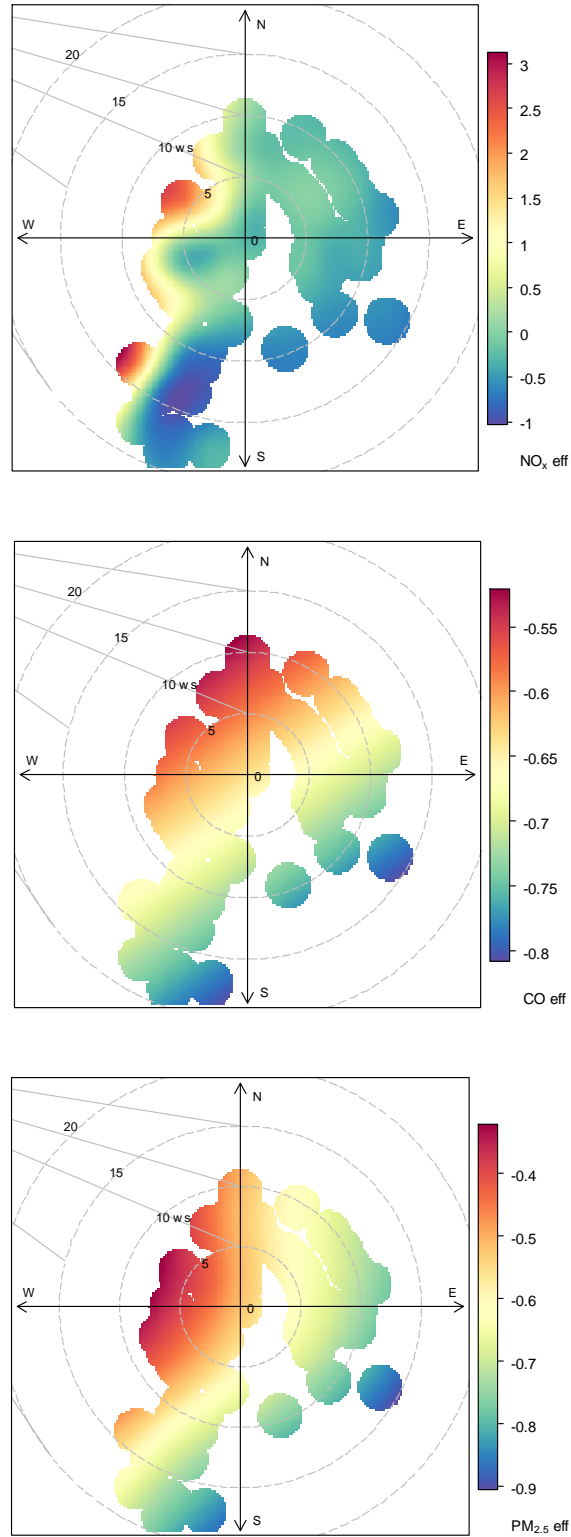


Figure 40. Polar plots showing  $\text{NO}_x$ , CO and  $\text{PM}_{2.5}$  pollutant removal efficacy, as obtained from the difference in the ratio between normalized concentrations at Laura Bassi and Marconi and normalized concentration in Marconi, as a function of wind speeds and directions in Bologna measured at the Bologna airport meteorological station during the winter thermographic campaign on 8-9/02/2018.

Similar to the summer case, also during the analyzed period in winter stronger reductions were observed under the upwind and katabatic cases, even though differences for the different pollutants are resulting (

		NOx eff				CO eff				PM eff			
	N	mean	Std	min	max	mean	std	min	max	mean	std	min	max
<b>parallel anabatic</b>	44	-0.04	0.73	-0.92	3.27	-0.64	0.20	-0.90	0.02	-0.64	0.19	-0.93	0.04
<b>parallel katabatic</b>	30	-0.05	1.08	-0.91	3.24	-0.70	0.14	-0.89	0.38	-0.60	0.36	-0.93	0.38
<b>upwind</b>	17	-0.25	0.31	-0.63	0.43	-0.67	0.16	-0.83	-0.33	-0.64	0.14	-0.78	-0.33
<b>downwind</b>	10	0.50	1.42	-0.86	3.02	-0.56	0.31	-0.81	1.24	-0.25	0.66	-0.88	1.24

Table 5).

In addition, when analyzing the efficacy of GI on air pollution, it is important to consider the reduced energy use caused by trees through lowering air temperatures, and blocking winds in winter as thoroughly analyzed in the first version of this Deliverable. The reduced energy use by buildings caused by trees may further contribute to reduce air pollution generated by residential heating and air conditioning systems both locally as well as at urban level.

With respect to this observation, in the first version of this Deliverable the results of the two intensive thermographic campaigns carried out within the summer and winter Bologna experimental campaigns confirmed clearly the positive effect of GI on the mitigation of the UHI effect, as resulted by the 2°C temperature difference between Laura Bassi and Marconi street canyons. The effect of trees on winter temperatures observed in the two street canyons was instead less clear as due to the nighttime increase in temperature observed at both urban sites and not at the rural ARPAE station of Mezzolara (Figure 41 reported again in the updated version for the sake of clarity).

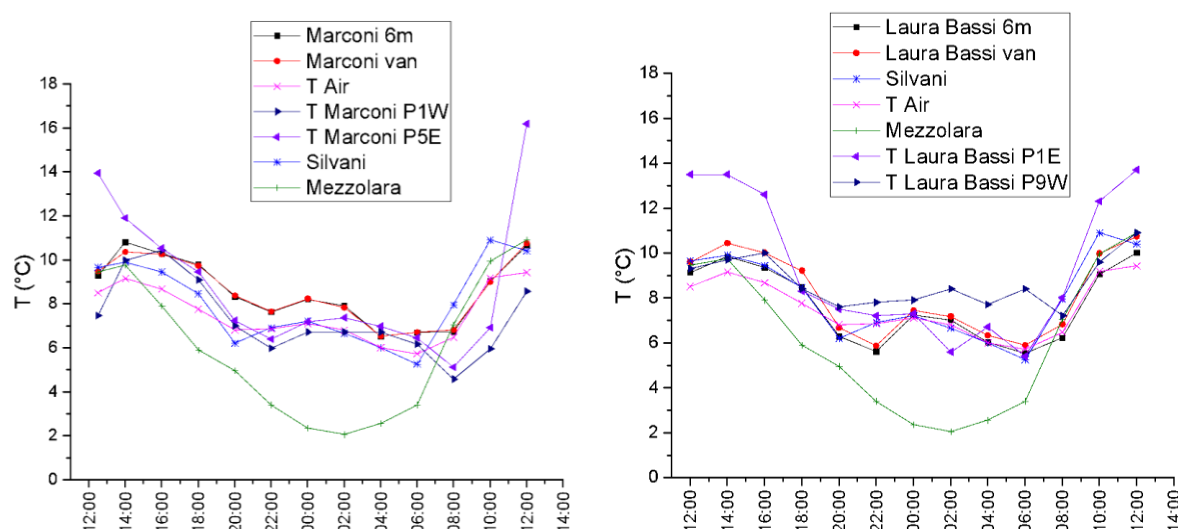


Figure 41: Temperature evolution within the day of the winter intensive thermographic campaign in Bologna (08-09/02/2018), measured by the thermo-hygrometers, the ARPA-ER instrumentation in one urban (Silvani St.) and one rural meteorological station (Mezzolara) and of building façades of buildings located on the West and East side of the 2 street canyons (Marconi St. on the left and Laura Bassi St. on the right) as retrieved from the thermal images acquired with the two thermal cameras.

In the first version of the Deliverable, this behavior during night was tentatively attributed to the presence of a cloud cover which was noted during the thermographic campaign. The presence of the cloud cover limiting the nighttime radiative cooling partially covering the Emilia region and moving during night was indeed confirmed by thermal composite satellite images (Figure 42). In fact, it is known that if clouds are present during night some of the heat emitted from the Earth's surface is trapped by the clouds and reemitted back towards the Earth, which results in a slower temperature decrease than in clear sky.

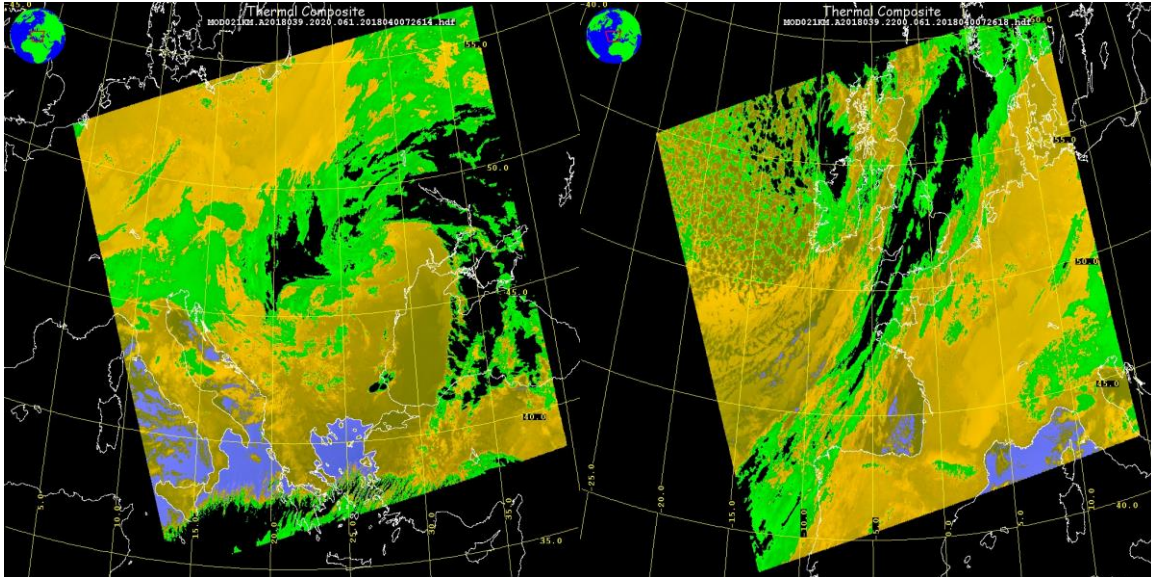


Figure 42. Thermal composite MODIS Terra 21 km satellite images for 08/02/2018 at 20:20 (left) and 22:00 UTC (right) (images courtesy of the NASA Level-1 and Atmosphere Archive & Distribution System (LAADS) Distributed Active Archive Center (DAAC), Goddard Space Flight Center, Greenbelt, MD<sup>5</sup>).

However, the presence of the cloud cover alone cannot fully explain the particular observed for urban air and building temperatures during the night of 08/02/2018. The specific pattern observed in the two street canyons both for air as well as for building façades temperatures can be tentatively attributed to the on and off switching of residential heating: in this case the difference between the patterns observed in Marconi and in Laura Bassi Sts. might be due to the different kinds of buildings in the two street canyons, where Marconi is characterized by block of flats with central heating whereas Laura Bassi is instead characterized by small residential houses with independent heating.

<sup>5</sup> <https://ladsweb.nascom.nasa.gov/>

### 4.1.3 Vertical mass exchange processes: the Lazzaretto case study

Besides testing the efficacy of photocatalytic coatings in removing  $\text{NO}_x$  pollutants (D3.8 and D3.6), the Lazzaretto site gives the opportunity to test different atmospheric processes in a controlled environment. Even though by controlled environment we usually refer to laboratory investigations, due to its particular configuration, the Lazzaretto site is much alike an open-air laboratory inside a real city. In fact, in this area all the buildings are similar in dimension, shape and materials, rooftops are gently sloping with solar panels installed on them and the entire area is built as an array of boxes. In this context, the geometry of the street canyon is almost ideal, with regularly shaped equally tall buildings surrounding the street, allowing to better reproduce laboratory investigations in the real environment.

Among other studies, mass exchange processes between the in-canyon and the free atmosphere have been widely assessed in the recent past, mostly by means of laboratory (Salizzoni et al., 2009; Di Bernardino et al., 2018) and numerical (Cheng et al., 2009a; Liu and Wong, 2014) investigations. The general aim is the evaluation of pollutant removal efficacy operated by local meteorological forcing both related to mean motion or turbulence.

In the context of the Lazzaretto campaign, the mass exchange processes are tackled considering the turbulent transport as the main vehicle for pollutant removal. This assumption as well as the methodology adopted for the identification of the most suitable period to perform the analysis have been extensively discussed in D3.8. Briefly summarizing the results obtained in D3.8, the selected period, spanning from the 4<sup>th</sup> to the 6<sup>th</sup> of August 2018, was characterized by non-synoptic clear sky conditions and by the presence of a local thermal circulation was almost unperturbed by large scale phenomena.

The analysis of mass exchange processes was carried out using data collected by the open path gas analyzer located on the rooftop of canyon A, which, as previously reported, allows to measure  $\text{CO}_2$  and  $\text{H}_2\text{O}$  concentrations at 20Hz sampling rate and to compute their turbulent fluxes using the wind components sampled by the coupled anemometer. Vertical transport of both gases has therefore been evaluated and shown in Figure 43.

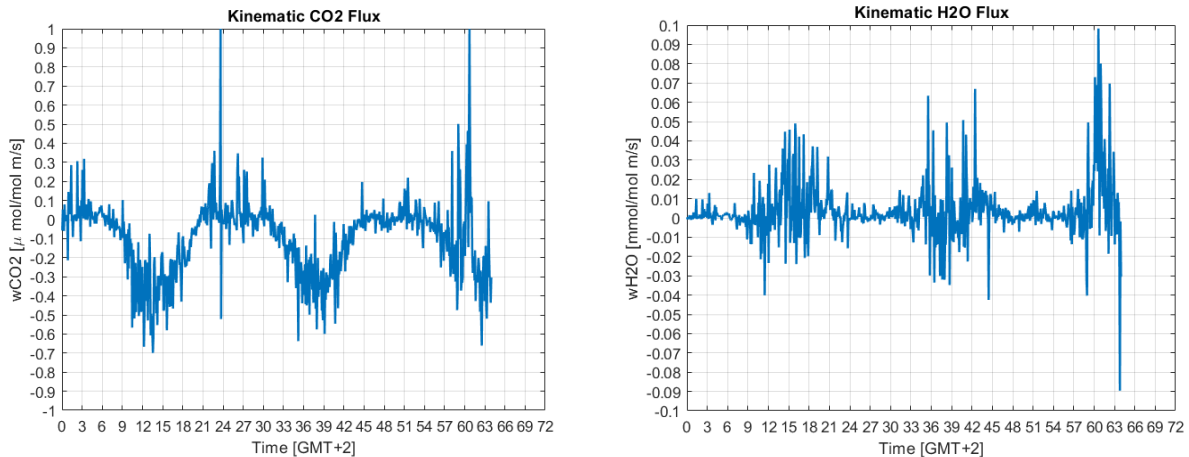


Figure 43: Kinematic  $\text{CO}_2$  (left) and  $\text{H}_2\text{O}$  (right) fluxes for the whole period selected for analysis (04-06/08/2018) during the Lazzaretto summer 2018 campaign. Data are 5-minutes averaged.



Both fluxes show the typical diurnal path of turbulent phenomena, with the majority of the signals intensity and variability spread during the insolated hours, while during night vertical motions are suppressed despite some sporadic episodes. CO<sub>2</sub> behavior is well defined by a vertical transport from the rooftop to the canyon during the daytime, while during night transport is on average reversed. H<sub>2</sub>O shows a more oscillatory behavior, with no net transport direction during the whole period. The difference is probably related to the different nature of the two compounds: while CO<sub>2</sub> is a well-mixed gas in the troposphere as due to its long residence time, H<sub>2</sub>O concentrations present strong space and time variabilities, directly related to ground water evaporation and transpiration, and to the water content of different air masses. Moreover, differently from CO<sub>2</sub>, H<sub>2</sub>O is a chemically reactive gas and therefore its actual concentration in the canyon may depend also from other external factors. For these reasons, the following analysis will focus exclusively on CO<sub>2</sub> whose concentration field perturbations can be entirely attributed to atmospheric processes. The theoretical idea behind this approach is that the same analysis may be extended to all atmospheric compounds, including major pollutants, whose atmospheric lifetime is much larger than the turbulent timescales.

Turbulent fluxes, as computed in Figure 43, allow to determine the direction of the mass transport, but are not sufficient alone to infer conclusive statements on the origin of the considered masses. In particular, a negative mass flux can either account for a CO<sub>2</sub> increase due to particles flowing into the canyon or for a decrease due to outgoing fluctuations. To determine the impact of turbulent ventilation on CO<sub>2</sub> removal, data are treated following the quadrant analysis, firstly introduced by Willmarth (1975). The analysis is based on the determination of the flux ( $w'CO_2'$ ) single components signs. Therefore, four quadrants can be defined as follows:

- the 1<sup>st</sup> quadrant is defined for  $w' > 0$  and  $CO_2' > 0$ . This condition is known as outward interaction, accounting for a net transport of polluted air from the canyon to the free atmosphere.
- the 2<sup>nd</sup> quadrant is defined for  $w' < 0$  and  $CO_2' > 0$ . This condition is known as sweep and it is responsible for the transfer of momentum from the free atmosphere into the canyon. During sweep events the polluted air is trapped and forced to re-circulate inside the canyon, providing a condition of poor ventilation.
- the 3<sup>rd</sup> quadrant is defined for  $w' < 0$  and  $CO_2' < 0$ . This condition is known as inward interaction, accounting for a net transport of clean air inside the canyon.

- the 4<sup>th</sup> quadrant is defined for  $w' > 0$  and  $CO_2' < 0$ . This condition is known as ejection and it represents the upward transport of polluted air from the canyon to the free atmosphere, providing a condition of good ventilation.

This classification is schematized in Figure 44. The inclination of the street canyon to vent is generally correlated to the shape and intensity of the flow and turbulence structures developing inside the canyon. Considering unchanged synoptic conditions, different structures can be retrieved for different geometries and background wind conditions. As the geometry of the canyon is defined by the local morphology, it is important to evaluate the quadrant analysis for different wind regimes. In particular, the classification was carried out considering different wind directions impinging on the canyon. As such, four (two perpendicular and two longitudinal) wind direction scenarios were defined, with a range of 10 degrees around the precise values. Longitudinal directions are called respectively anabatic and katabatic regimes for winds coming from north-north-west and south-south-east. Perpendicular winds are called upwind or downwind depending on the wind impinging firstly on the instrumented building or on the opposite. Actual directions are 90° shifted with respect to the longitudinal. The results of the adjoined quadrant analysis and wind direction classification are presented in Figure 45 and Figure 46.

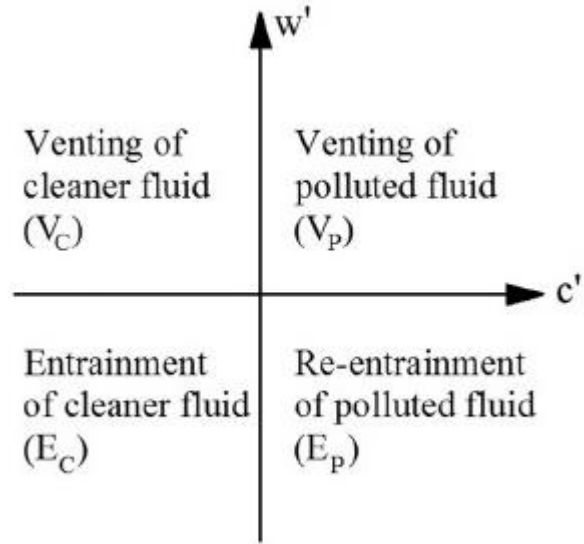


Figure 44: Scheme of the quadrant analysis applied to the mass transport.  $c'$  stands for a generic pollutant concentration (source: Di Bernardino et al., 2018).

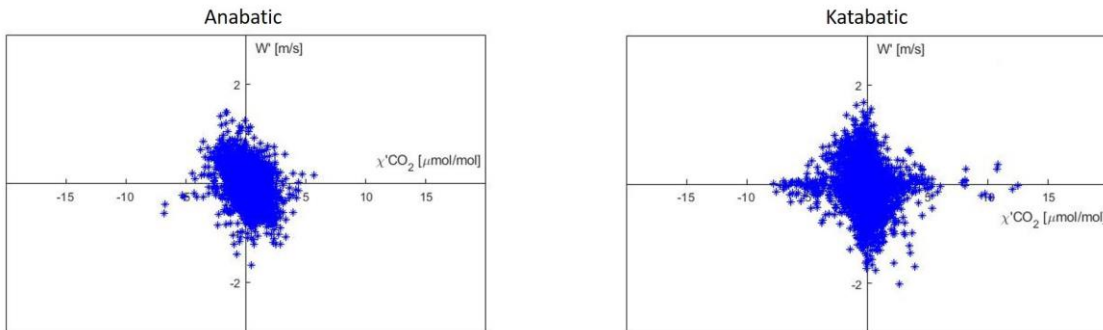


Figure 45: Quadrant analysis applied to the longitudinal wind directions. Vertical velocity fluctuations as a function of  $CO_2$  concentration fluctuations.

Both longitudinal and downwind perpendicular wind directions show a slight predominance of sweep and ejection phenomena over the inward and outward interactions. This result can confirm the basic hypothesis that pollutants are mainly transported by turbulent motions. In fact, both sweep and ejection conditions correspond to a scenario in which the turbulent vertical momentum

flux  $\langle w'u' \rangle$  is negative, which is the most common situation during non-synoptic days, at least at rooftop level (D3.8).

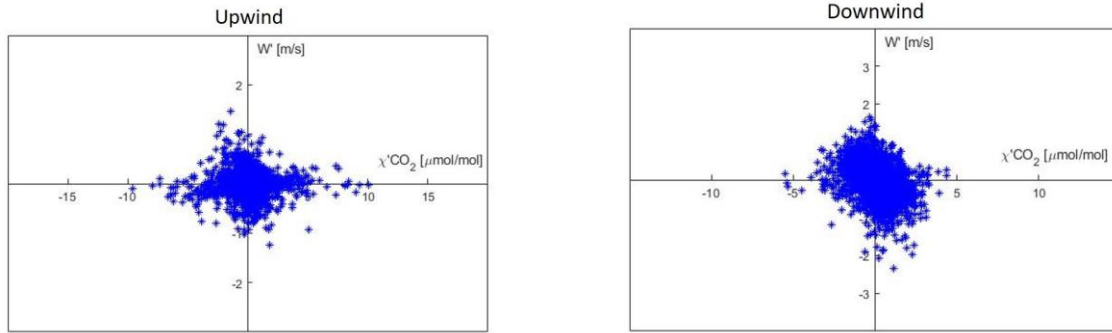


Figure 46: Quadrant analysis applied to the perpendicular wind directions. Vertical velocity fluctuations as a function of CO<sub>2</sub> concentration fluctuations.

The upwind direction is the most chaotic among the four analyzed ones. All the four quadrants present the same frequency of occurrence and no process seems to dominate on others. This variability in the frequency of occurrence might depend on be the location of the sensors. Under this wind direction the instrumentation acquires data directly from the background wind and its related turbulence occurring before has the opportunity to interact with the cavity. This means that the results obtained for the upwind case mainly depend on the mean wind and its turbulence, that is generated from the interaction between the mean flow and the rooftop, rather than on the morphology of the canyon cavity. In this condition, the morphology of the canyon does not contribute to the exchange processes between the in and out flow, so that the upwind wall of the canyon cannot be firmly considered as the site where the canyon can ventilate. This suggestion is also confirmed by the weighted mass transports  $\tau_{w'\chi'CO_2}$  which quantify the mean intensity of the mass transport in each quadrant weighted on the number of occurrences of each exchange phenomenon (Kellnerova et al., 2013):

$$\tau_{w'\chi'CO_2i} = \frac{\langle w'\chi'CO_2 \rangle_i N_i}{N_{tot}}$$

Where  $\langle w'\chi'CO_2 \rangle_i$  is the averaged turbulent CO<sub>2</sub> vertical flux in quadrant  $i$ ,  $N_i$  is the number of occurrences of the turbulent flux in the quadrant  $i$  and  $N_{tot}$  is the total amount of data.

$ \tau_{w'\chi'CO_2}  [m s^{-1} \mu mol mol^{-1}]$				
	Outward interaction	Sweep	Inward interaction	Ejection
Anabatic	0.0026	0.0741	0.0187	0.0509
Katabatic	0.0037	0.0030	0.0062	0.0232
Perpendicular (upwind)	0.0066	0.0082	0.0009	0.0109

<b>Perpendicular (downwind)</b>	0.0005	0.0668	0.0151	0.0629
-------------------------------------	--------	--------	--------	--------

*Table 6: Absolute values of the weighted mass transports for each quadrant in canyon A.*

Table 6 reports the absolute values of the weighted mass transports for each quadrant at canyon rooftop. Conversely from previous studies (e.g. Di Bernardino et al., 2018), sweep and ejection phenomena dominate over the inward or outward interactions, because mass fluxes are mainly negative during the analyzed period. Therefore, mass and momentum fluxes appear to be more strictly related than in other studies, suggesting the turbulent momentum transport as the key mechanism for pollutant removal from steep canyons, where the mean flow is suppressed by the morphology.

Downwind and anabatic cases show the most intense phenomena, since they are generally related to boundary layer conditions or local circulations favorable for vertical motions. During perpendicular conditions, the inertial circulation which settles inside the canyon shapes as a bidimensional vortex which carries fresh air from the free atmosphere into the canyon along the leeward wall, mixes with the street level polluted air and climbs the windward wall. Sweep or ejection will then depend on the efficacy of air trapping and recirculation over escape. In this particular case, sweep and ejection have almost equal efficacies. Largest ejection phenomena are also detected during downwind conditions, causing it to be the most ventilated case, in agreement with Buccolieri et al. (2015).

Anabatic condition presents large value of ejection too, but the dominant phenomenon is the sweep. Due to the evanescent nature of anabatic flows, it is difficult to explain this difference, but several effects can have an impact on it. Firstly, for longitudinal wind conditions, the in-canyon vortex is stretched in a helical shape, reducing the vertical exchange process and enhancing advected recirculation. Secondly, anabatic conditions are typical of daytimes, during which the air at rooftop level can become warmer than that inside the canyon, trapping the polluted air inside it.

To conclude, the behavior of exchange processes during katabatic condition shows some interesting features. In particular, this is the only condition where ejection is clearly dominating over the other phenomena providing venting of fresh air in the canyon, despite its intensity being not as large as for anabatic or perpendicular cases. A possible explanation relies again in the nature of the flow. Katabatic flows are typical of nocturnal periods, when the atmosphere above the canyon is thermally stratified while the air inside the canyon is generally warmer and still well mixed. This scenario is favorable to an efficient venting of fresh and cold air from the rooftop inside the canyon and ejection of warm and polluted air.

## 4.2 Dublin

### 4.2.1 Meteorology and air pollution: statistical analysis

This section presents some preliminary statistical analyses of collected data within the winter experimental campaign with the experimental setup previously described. Figure 47 presents the normal distribution plots for the wind speed data categorized by wind direction groups; the figure illustrates that different wind directions are characterized by different values distribution and magnitudes for wind speed. The wind rose plot represented in Figure 48 shows more properly that even though the east and south-east are the dominant wind directions in the sampling site the

west component is also important, while S and N directions are very rare: this is mainly because of the street canyon orientation as illustrated in the site description. As such, the local wind rose is very different from the local climatological one (see D6.1 Figure 18), characterized by dominant strong west and south-west winds, which clearly depends from the different nature of the two sampling sites (i.e., being Pearse Street an urban site in a street canyon, while data described in D6.1 were collected at the Dublin airport).

Figure 49 shows the time series for the collected maximum, minimum and average wind speeds (m/s): as can be observed, the values fluctuate by time and there are many peak values to be considered and further investigated.

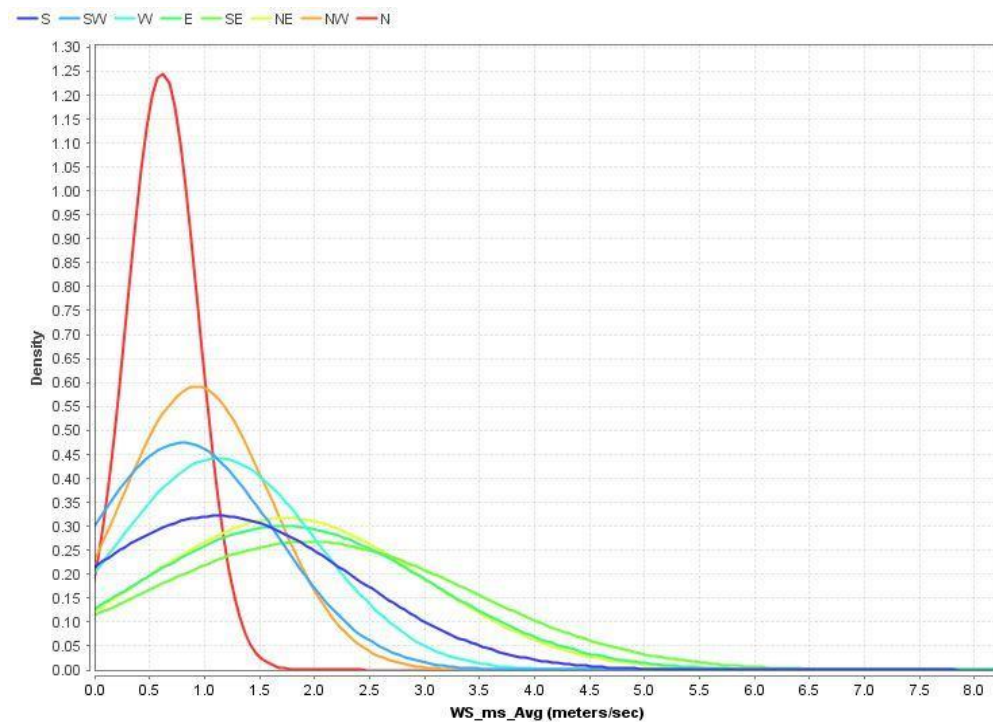


Figure 47: Distribution plot of wind speed data according to the different wind direction categories.



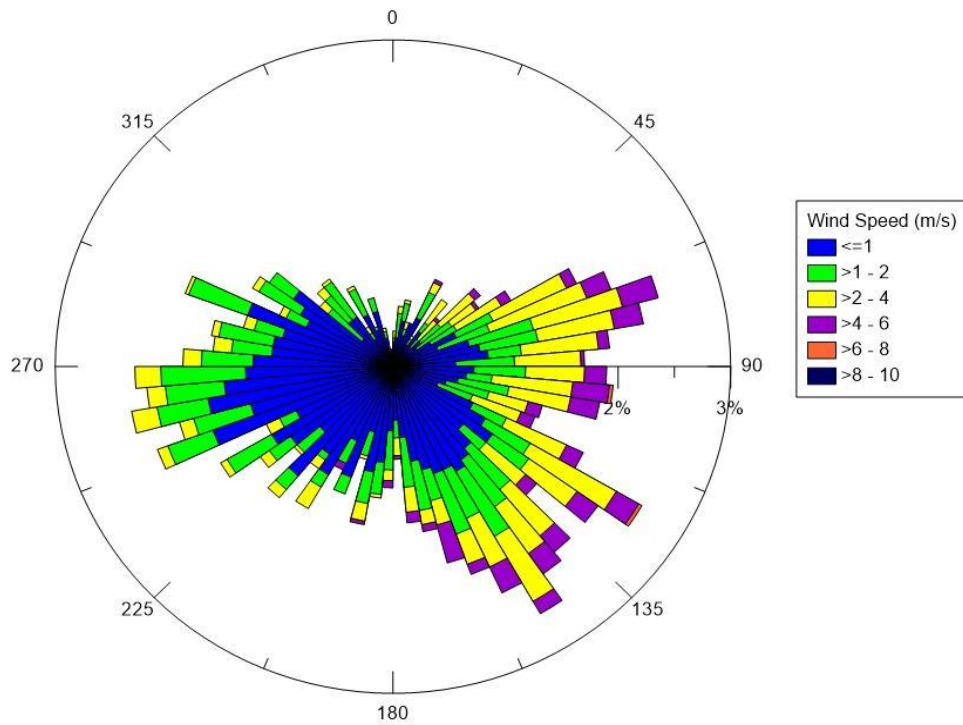


Figure 48: Wind rose plot for the Dublin site.

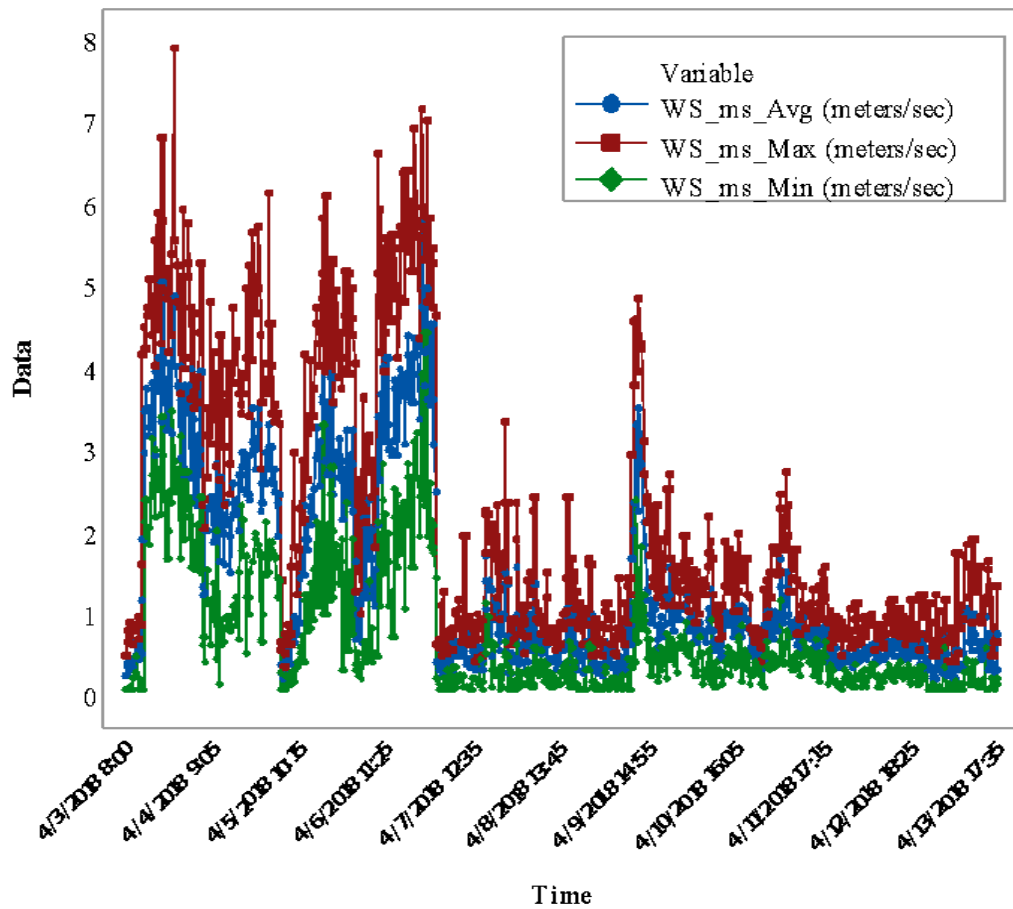


Figure 49: Minimum, maximum and average wind speed data.

Figure 50 and Figure 51 show the normal distribution curves for the  $\text{NO}_x$  concentrations in front of the LBW and behind the LBW, respectively. The normal distributions demonstrate that wind direction produces significant effects on the distribution of  $\text{NO}_x$  concentrations. In particular, the highest concentrations are observed in correspondence with the South-East direction, while the lowest concentrations are connected with East directions.

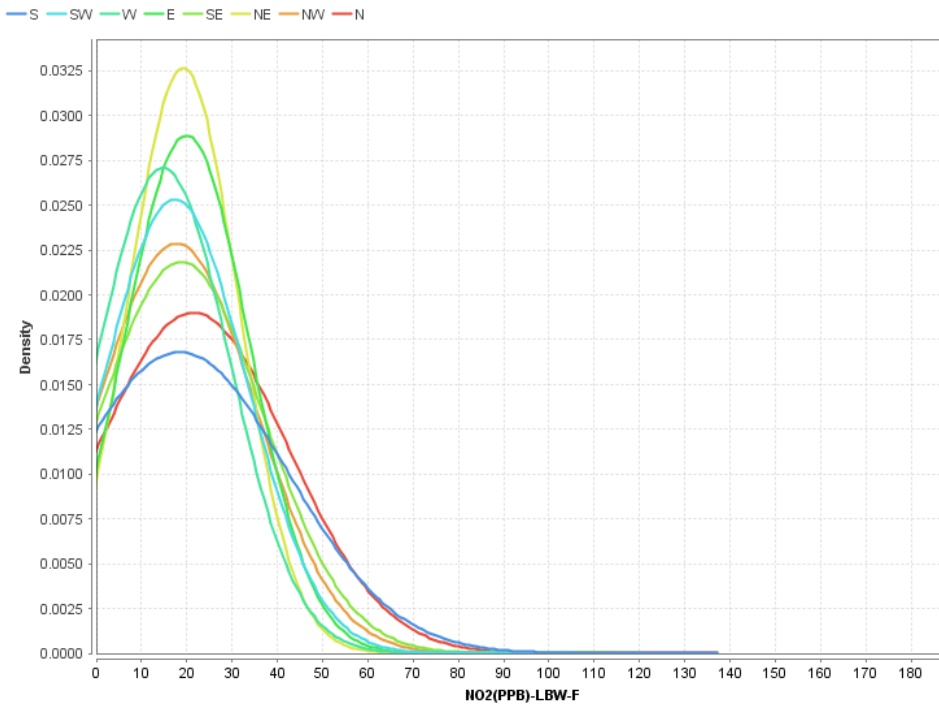


Figure 50: Distribution plot of  $\text{NO}_x$  (ppb) in front (F) of the LBW.

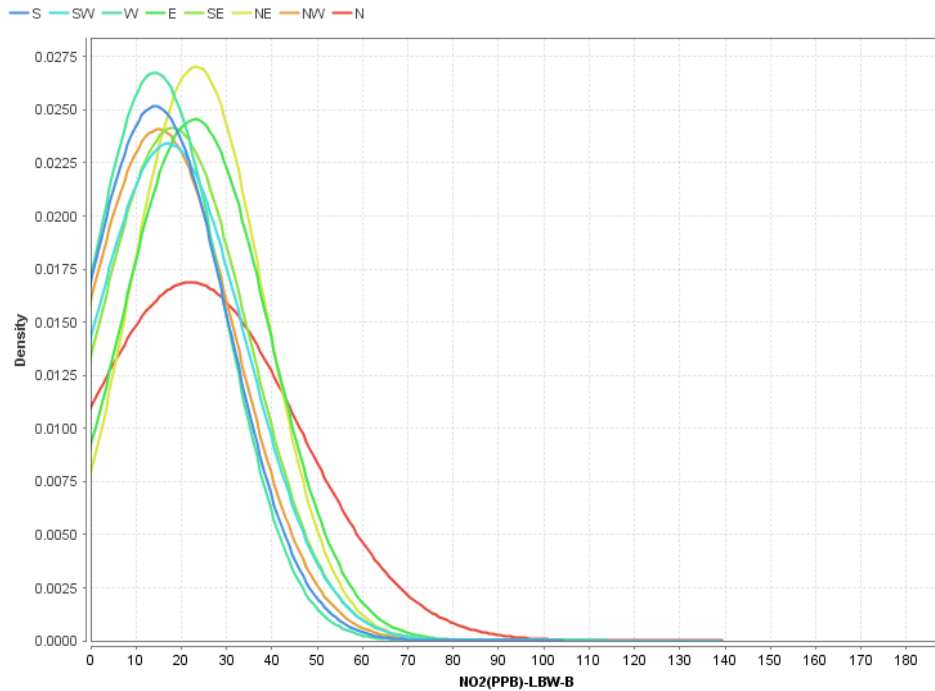


Figure 51: Distribution plot of  $\text{NO}_x$  (ppb) behind (B) the LBW.

Figure 52 further provides a multi-scale time series plot for the  $\text{NO}_x$  concentrations recorded in front of the LBW (red line) and behind the LBW (blue line). As such, Figure 52 shows that, in general, the  $\text{NO}_x$  concentrations are higher in front of the LBW than behind it, which demonstrates the potential to use LBWs as a PCS to control air pollution in the built environment.

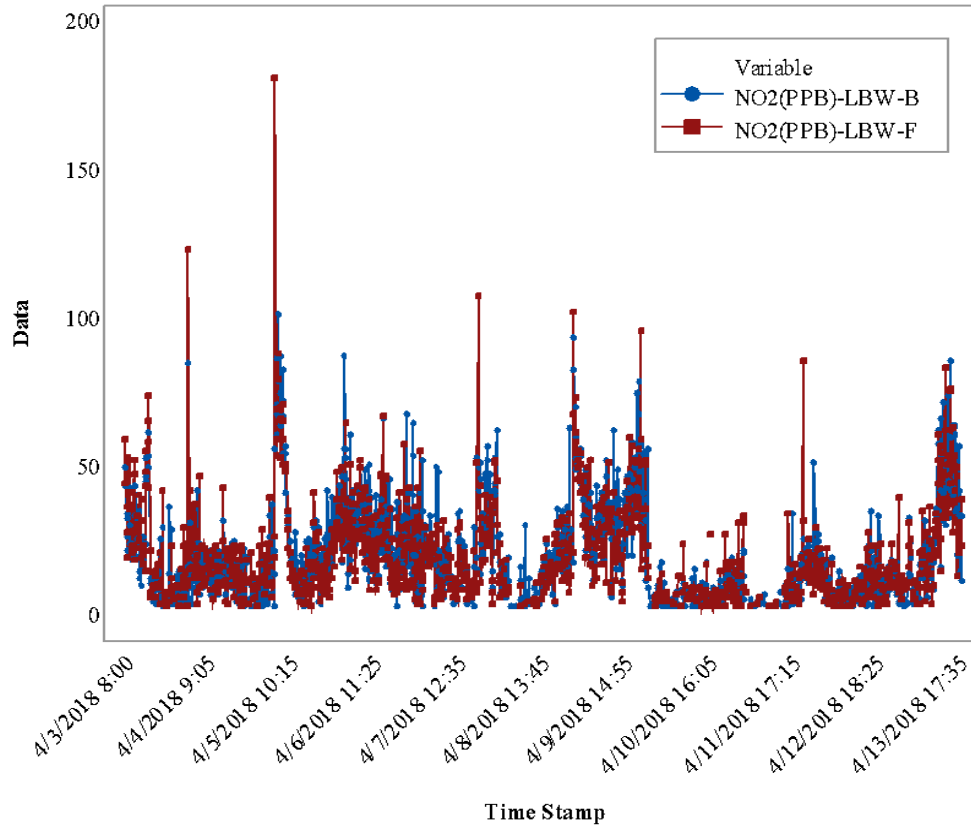


Figure 52: Time series plot for the NO<sub>x</sub> concentrations (ppb) recorded on both sides of the LBW.

From Phase 2 results, the percentage difference of the concentration of PM<sub>10</sub> on both sides of the walls was also calculated and represented in the form of the histogram for the presence of the wall (Figure 53C) and the absence of wall (Figure 53D). Histogram of Figure 53C indicates that when the walls were present, between -40% and 20%, the frequencies were higher. On the other hand, when the walls were absent, this range was between -40% and 60%. Therefore, in the presence of walls, an average increase of 23% was recorded behind the wall, whereas, in the absence of LBW there was only 2% increase in the pollutant on average. The maximum increase of the concentration of PM<sub>10</sub> in the presence of wall was 188 percentages while the maximum decrease in concentration was 59 percentages. Conversely, without any wall, the maximum increase and decrease were 190 and 58% respectively. For PM<sub>2.5</sub>, the first histogram (Figure 53A) shows that the frequency is higher in the range of -60% to -20% and therefore, in the presence of LBW, the concentration behind the wall was on an average 32.25% higher than that behind the wall. The maximum increase recorded behind the wall was 127% whereas, the maximum decrement behind the wall was 33%.

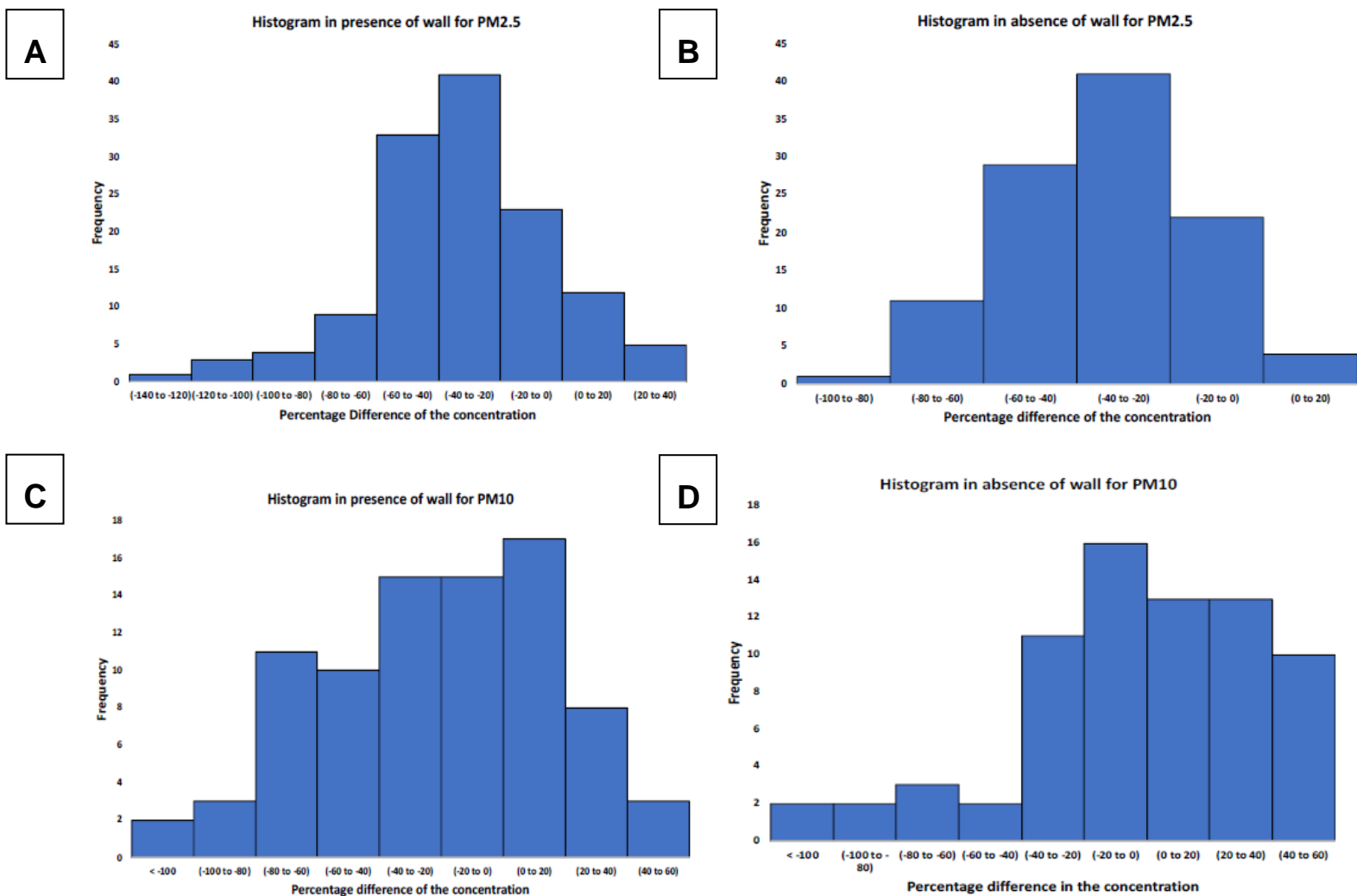


Figure 53: (A) Histogram representing the frequency of different percentage change for PM<sub>2.5</sub> in presence of LBW (B)Histogram representing the frequency of different percentage change for PM<sub>2.5</sub> in absence of LBW (C) Histogram representing the frequency of different percentage change for PM<sub>10</sub> in presence of LBW (D)Histogram representing the frequency of different percentage change for PM<sub>10</sub> in absence of LBW.



## 4.2.2 Meteorology and air pollution: preliminary results

This section presents the preliminary results and an outlook from the Dublin LBW field experiment. Figure 54 shows the distribution of the calculated reduction in the  $\text{NO}_x$  concentration between the front of the LBW and the back of it, which can be very different depending on the different wind directions categories.

Figure 54 and Figure 55 show that LBW may also produce negative effects in some occasions. Figure 54 and Figure 55 clearly demonstrate that LBWs, in the current experimental setup, work for most of the wind direction categories except for the East, North-east and North directions.

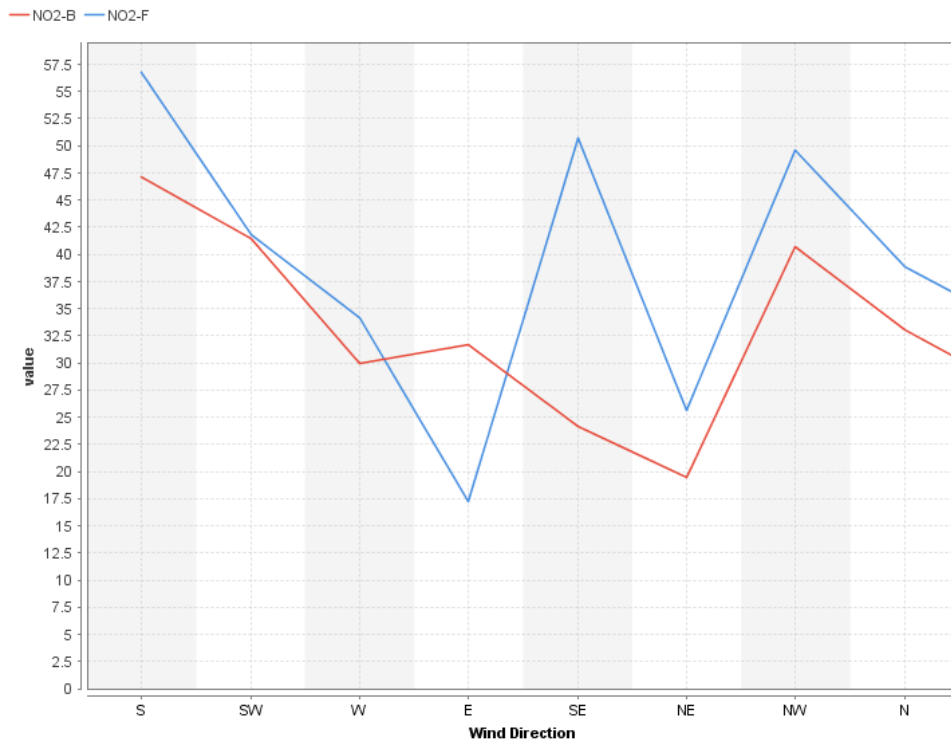


Figure 54:  $\text{NO}_x$  concentration (ppb) in (F) & (B) of the LBW per wind direction.

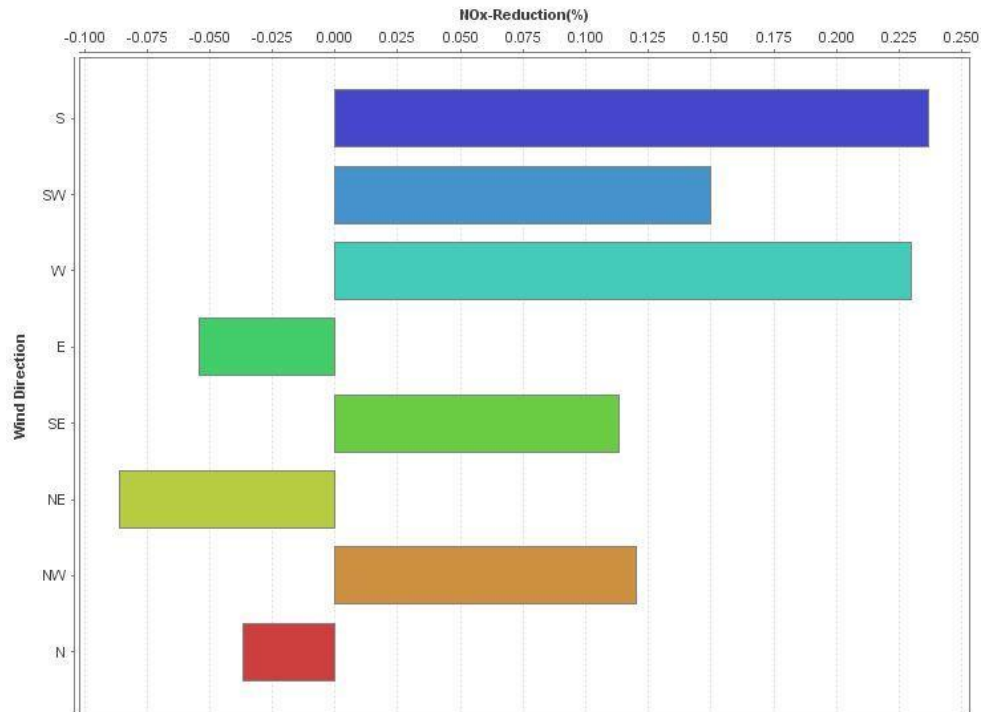


Figure 55: Median NO<sub>x</sub> (ppb) reduction behind LBW.

Figure 56 provides the standard deviations of the reduction in the NO<sub>x</sub> concentrations per wind direction categories: as can be observed, standard deviation percentages are greater than 5% in most of the cases except under the north-east direction, which has a negative impact on NO<sub>x</sub> concentrations and for which the LBW effect is reversed. In particular, as for the North direction, the absence of a clear impact of LBW clearly depends from the fact that this direction was seldom observed, which contributes to the very high variations linked to this direction which can be noticed in Figure 56.

The outlooks from the presented preliminary results can be outlined as follows: LBWs act as a baffle at street level and increase the distance between the pollutant source and human receptor.

LBWs can provide a solution to enhance localized dispersion and improve air pollution in distinct street canyons settings. However, depending on the wind direction, street geometry and position of the LBW, may cause air pollutant concentrations to increase behind the LBW, having the opposite effect of increasing pollutant concentrations instead of decreasing them. Since wind direction is very variable, LBW may produce both positive and adverse effects, which makes the designing process and their use in urban city planning very hard and ambitious. As a result of these preliminary observations, it is important to carefully plan and analyze where LBWs are placed so that they work in the desired direction to improve air pollution.

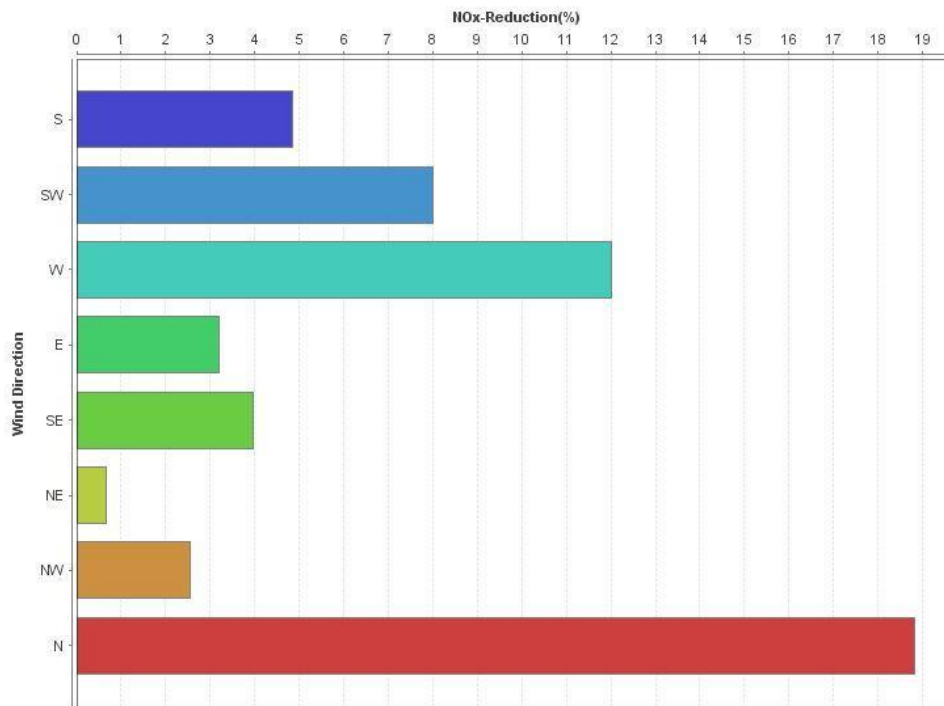


Figure 56: Standard deviation of NO<sub>x</sub> (ppb) reduction behind LBW.

For PM<sub>10</sub> Figure 57 and Figure 58 indicate the possibility of both higher and lower concentrations behind than in front of the wall both in the presence and absence of the walls.

The results indicate that for PM<sub>2.5</sub> the LBWs were not having an effect on the dispersion of the pollutant and the average percentage difference between both the sides of the walls was almost similar for both the case when LBWs were present or not. Therefore, the walls were not effective in altering the concentration of PM<sub>2.5</sub> behind the walls. However, for PM<sub>10</sub>, the results show that the walls modify the dispersion of the pollutant, as the maximum decrease in concentration was 59% in presence of the LBW. Conversely, without any wall, the maximum increase was 190%.

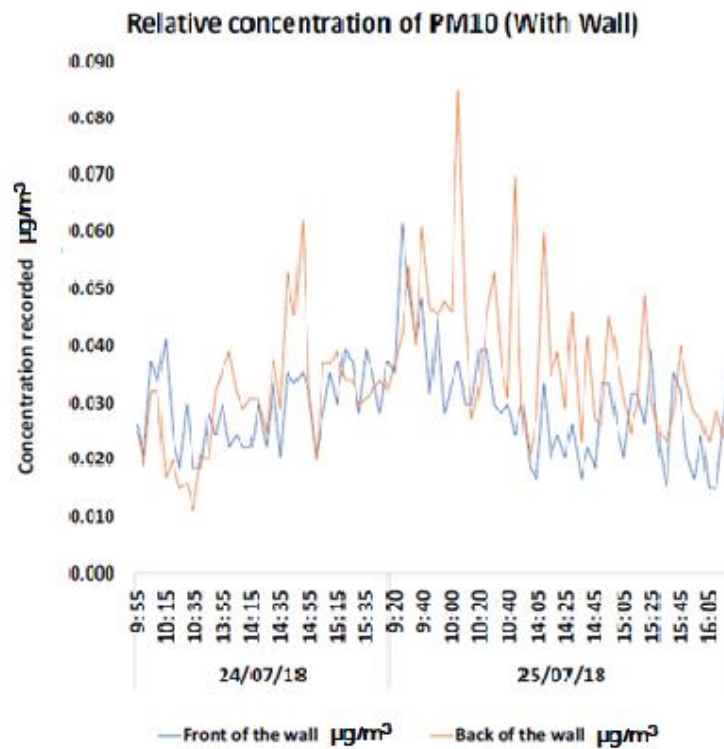


Figure 57: Relative concentration of PM<sub>10</sub> in front and back of the wall in the presence of the LBW.

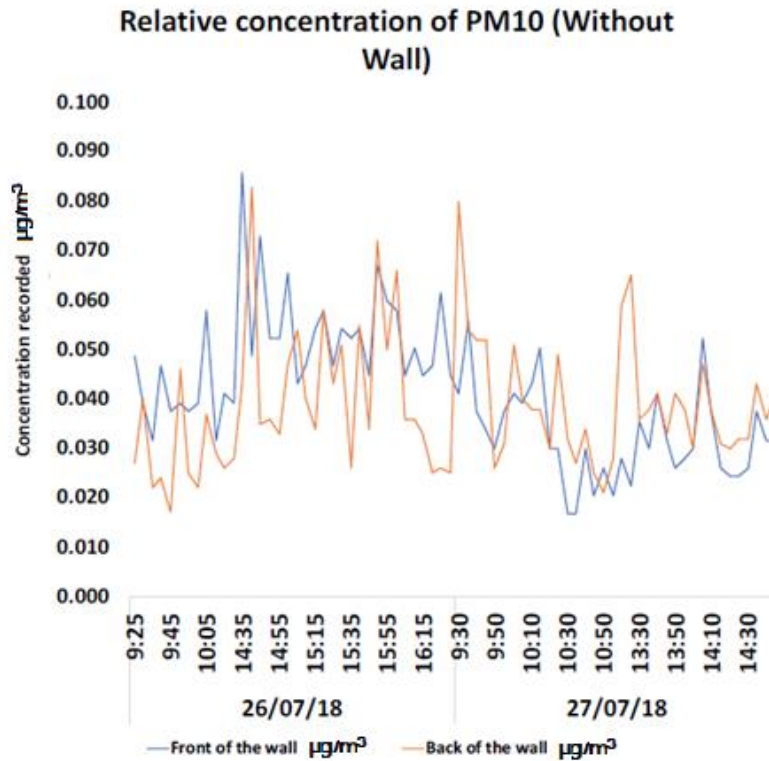


Figure 58: Relative concentration of PM<sub>10</sub> in front and back of the wall in the absence of the LBW.

## 4.3 Guildford

### 4.3.1 Data processing methods for low-cost sensors

#### Quality control

An example of the quality control procedure for SO<sub>2</sub> is shown in Figure 59. In this case, SO<sub>2</sub> is chosen since it has a large proportion of four out of five quality control categories. As can be seen, the Less Than Lower Limit classifies a substantial part of the data below -14 µg m<sup>-3</sup>. The sensor reports negative concentrations, which are retained since removing them in an automatic fashion is part of the ongoing work on data cleaning. As the concentrations increase, the fraction classified as error increases until all the high values are classified as errors. This is a result of the classification method, where changes in variance are classified as erroneous regardless of the actual values. As can be seen, the category rebasing is only attached to a small number of measurements. The sensor does not record data while the status is set to stabilizing, but for this data series, this amounts to 347 data points corresponding to 1% of the data.

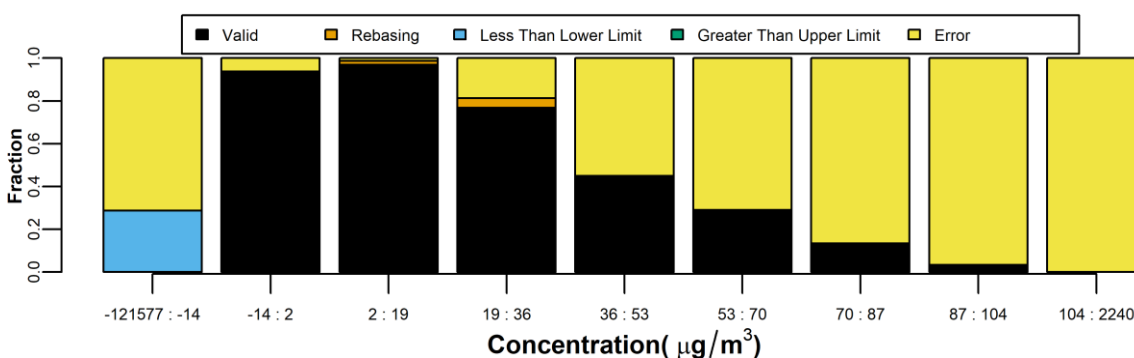


Figure 59: Stacked bar chart of the status tag for the SO<sub>2</sub> concentration measurements as a function of concentrations. The two numbers under each bar represent the interval. The intervals are chosen to highlight the interval covered by data with a Valid status tag.

#### Outlier detection

Examples of the mechanism of the two outlier detection methodologies are provided in Figure 60 and Figure 61. Here, we show the NO concentration for a period in 2018 containing high concentrations, some classified as outliers. It is evident from Figure 60 that especially high concentrations and spikes in the data are classified as outliers. However, not all high concentrations are classified as outliers, since the classification of a measurement is classified as an outlier depends on the distance to the neighbouring points. A large number of points are classified as outliers towards the end of the period, but given the values on the y-axis, many of these data points are still in the order of magnitude of 100 µg/m<sup>3</sup> away from their neighbouring points.

Figure 61 shows that the ARIMA model reasonably accurately resembles the temporal development of the time series. For this method, it is even more evident that both upwards and downwards spikes are classified as outliers. It is natural that a sensor mounted on a bus stop will show a certain amount of 'spikiness' due to the binary nature of the source, a result also found by Velasco and Tan (2016). One could thus argue that the ARIMA model amounts to a smoothing of the data, and it is thus removing part of the bus stop signal. The lack of urban background measurements in the present study makes it challenging to separate the contribution to the total



concentration from the bus stop from the contribution to the total concentration from the urban background concentration.

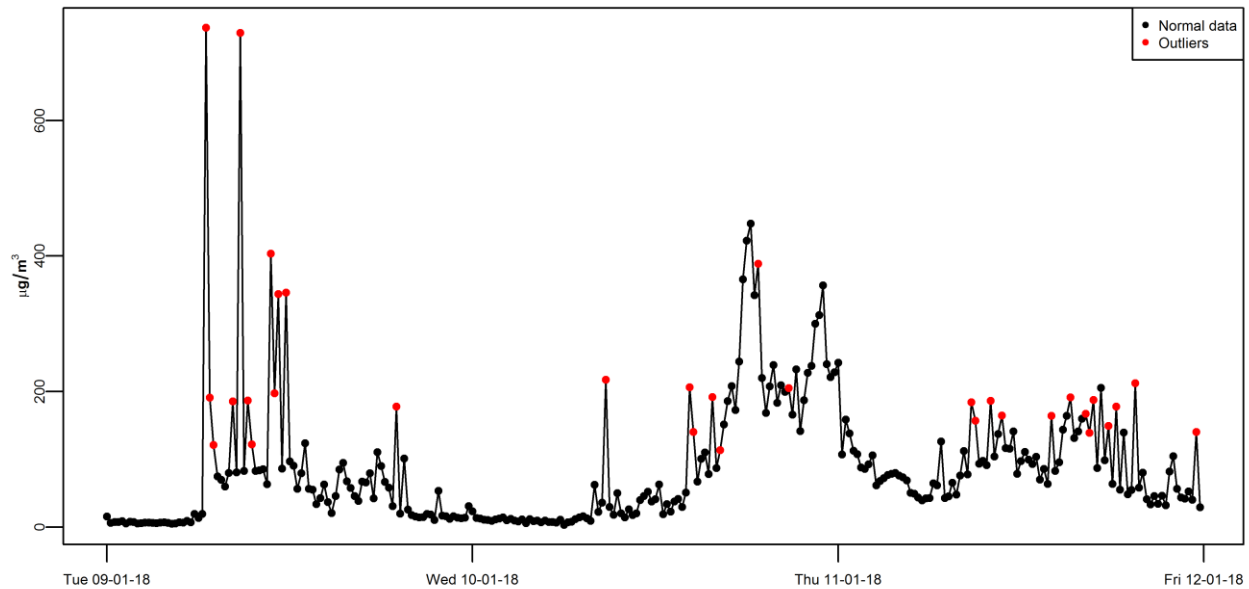


Figure 60: A short section of the AQMesh time series for NO. Outliers are detected using the k-NN method.

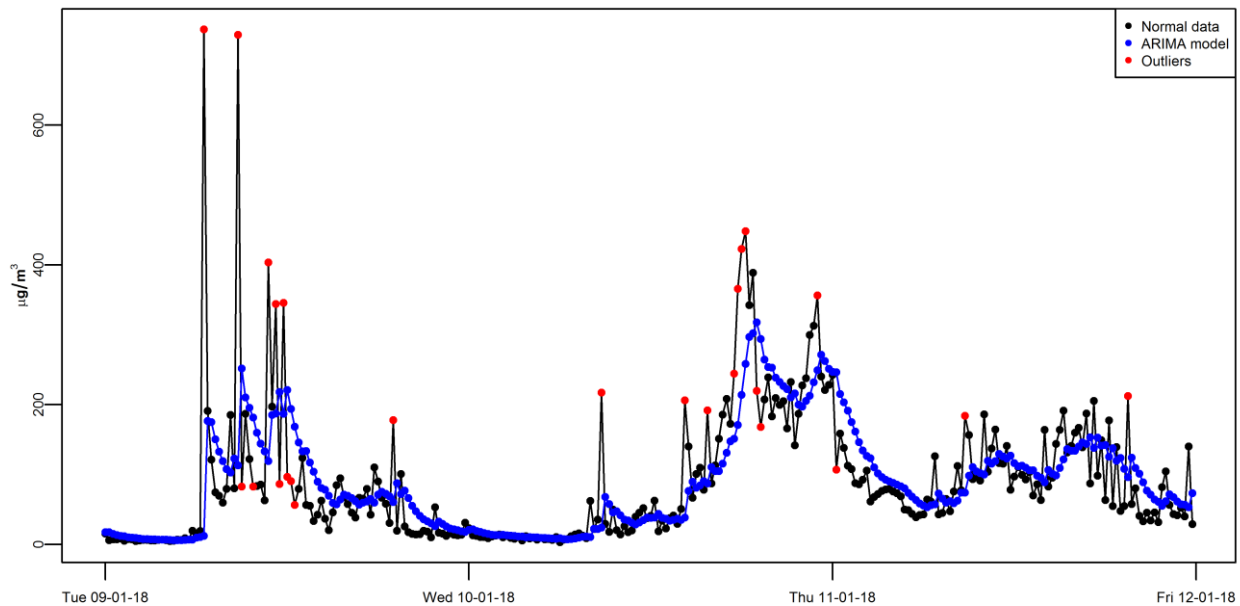


Figure 61: A short section of the AQMesh time series for NO. Outliers are detected using the ARIMA method. The blue points represent the ARIMA model fitted to data.

## Gap filling

Figure 62 shows a gap in the time series for NO represented in the figure as a grey dotted line. As can be seen, on this day the measured concentration was measured to be roughly  $50 \mu\text{g m}^{-3}$  for most of the day until close to 7 PM in the evening, when the concentration rapidly increased to approximately  $100 \mu\text{g m}^{-3}$ . This example clearly illustrates the gap filling challenges in air quality time series without excess information, and all three gap filling methods show poor performance.

The challenge is that the jump in concentrations can occur anywhere in the missing interval, and without excess information, there is no way to predict the exact location of the jump. Future research should thus be directed towards developing gap filling methods for this type of challenging situations.

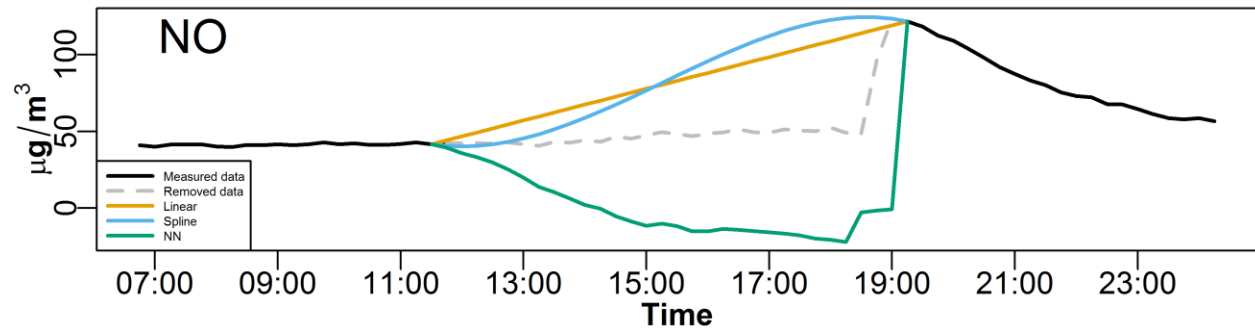


Figure 62: Example of a gap in the time series being filled by the three univariate methods in the present study.

### 4.3.2 Long-term time series measurements on a hedge

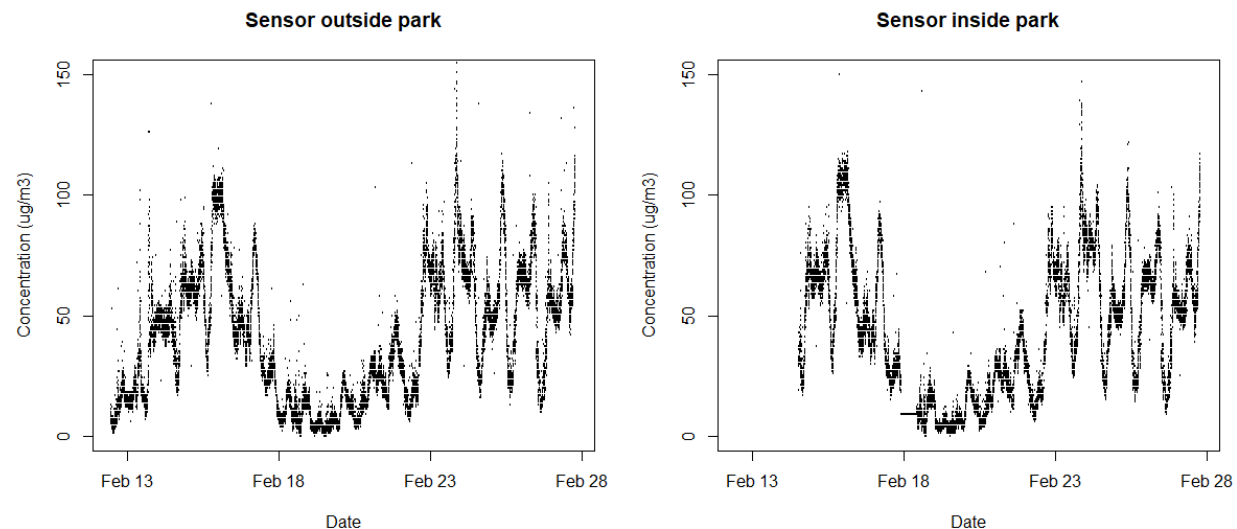


Figure 63:  $PM_{2.5}$  from respectively the sensor outside the park and the sensor inside the park. The horizontal “stripes” are caused by the measurements being rounded to integer values by the sensor.

The measurements on the hedge in Stoke Park are ongoing at the time of writing, and measurements will continue until the end of the project. The key findings will appear in Deliverable 5.4 ‘Strategic Portfolio Choice’ while the results will be generalized in Deliverable 7.2 ‘Generalised Solutions/Recommendations/Suggestions of Passive Control Systems’. As an example of the data collected from the hedge location in Guildford, Figure 63 shows the  $PM_{2.5}$  concentration for the two stations. The time series for the station inside the park is shorter than that for the station outside the park since it was deployed two days later. As can be seen, the two stations show good agreement in the measurements. The two time series show a clear diurnal pattern corresponding

to the traffic pattern. The period from 18 to 23 of February is half term in the UK and therefore characterized by lower concentrations compared to before and after. In the future, the data will be analysed in greater detail to quantify the effect of the hedge.

### ***4.3.3 Field experiments evaluating air pollution reduction of various GI – extended results***

The following section consists of the analysis and results obtained after the submission of the previous version of this Deliverable. While in the previous version we discussed overall changes in the pollutant concentration in the presence of different GI, here we provide in-depth analysis of the data we collected as part of the field measurements. The following results and discussions reported in Sections 4.3.3 and 4.3.4 are published in Abhijith and Kumar (2019).

#### **Effects on wind direction on pollutant concentration**

In order to understand the influence of wind direction on the concentrations behind the GI, we categorized the wind conditions into three main categories, i.e., along-road, cross-road and cross-vegetation. For some sites, like, for example, during cross-road winds at  $TH_{IB}$  and cross-vegetation winds at both  $T_{CB}$  and  $H_{IB}$  sites, we did not have enough data points available (Figure 64). In summary, the magnitude of percentage differences followed the following trend:  $\Delta PM_{2.5} < \Delta PM_{10} < \Delta PM_1 < \Delta PNC < \Delta BC$ . Usually, higher percentage changes were reported during along-road due to sweeping effects, followed by upwind of cross-road and cross-vegetation winds.  $TH_{CB}$  in close-road sites and  $H_{IB}$  in away-road sites reported the highest reduction in pollutant concentrations, mainly during along-road and cross-road wind conditions. These observations clearly indicate that a due consideration of local wind directions during the urban planning of new built-up areas could help in reducing exposure to roadside users. In cross-vegetation winds,  $TH_{CB}$  and  $TH_{IB}$  cases showed high percentage reduction among all GI.  $H_{CB}$  showed an increase in all pollutants (mainly PM) except for BC in cross-vegetation winds indicating upwind source of pollutants other than the road (maybe from houses as traffic correlated BC is absent). Similarly, increases in other cross-vegetation cases pointed towards emissions from background residential areas since no increase in BC concentrations were noticed. Most of the increase in pollutant concentrations behind GI was found in  $H_{CB}$  and  $T_{CB}$  sites and was strongly correlated with their physical dimensions. Hedge height at  $H_{CB}$  was lower (~1 m), whereas the width of single tree row present in  $T_{CB}$  was narrow (<6 m), which may have assisted in the accumulation of pollutants by failing to create a significant barrier effect (Hagler et al., 2012).

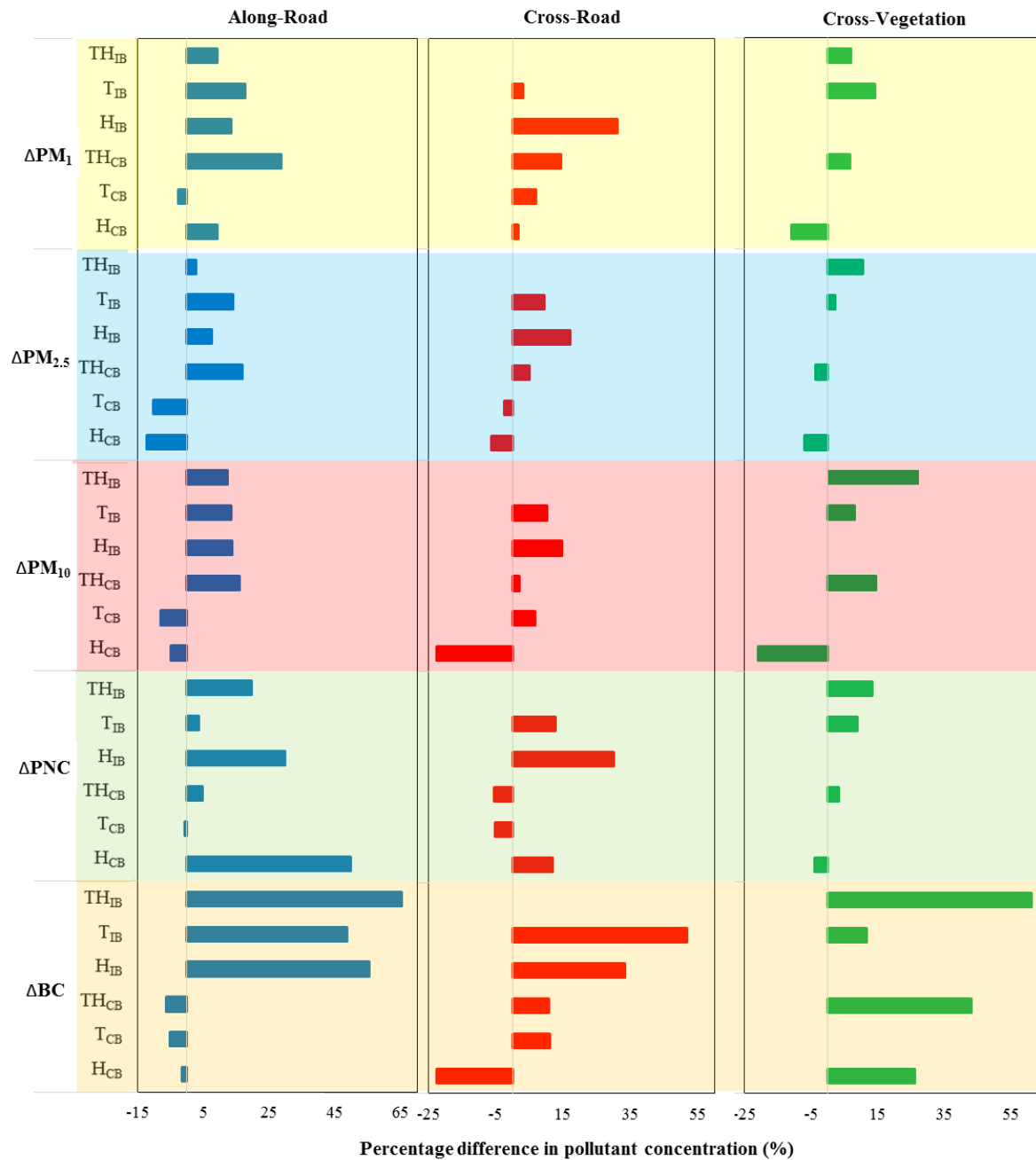


Figure 64: The percentage differences in various pollutants under along-road, cross-road and cross-vegetation wind conditions. The positive and negative differences indicated reduced and increased concentrations behind the GI at the close- and away-road sites (Abhijith and Kumar, 2019).

### Influence of GI on PM fractions

Figure 65 shows the differences in the percentage of PM fractions behind GI and in clear area or in-front of GI for the studied GI configurations. At most GI sites,  $PM_1$  fraction of fine particles in clear area and in-front of GI dominated the total PM fractions compared to  $PM_1$  behind the GI. This indicated the presence of fresh emissions from traffic in in-front/clear areas and reduction of corresponding  $PM_1$  fine fraction behind GI after passing through the barrier. While considering

overall PM fractions in hedges, both  $H_{CB}$  and  $H_{IB}$  displayed a reduction in fine particles ( $PM_1$  and  $PM_{1-2.5}$ ) behind GI and  $H_{CB}$  reported relatively higher reduction among them (Figure 65). Hedges with leaves close to ground assisted in reducing traffic originated fine fraction of PM ( $PM_1$  and  $PM_{1-2.5}$ ) by providing barrier effect and surfaces for deposition at breathing level. This PM removal mechanism of hedges is pronounced when emissions transported from the road to GI in cross-road wind direction and the higher reduction was observed in corresponding wind conditions (Figure 65).

No significant changes in all PM fractions were observed during cross-vegetation winds. Both the tree only sites (i.e.,  $T_{IB}$  and  $T_{CB}$ ) displayed no significant changes in PM fractions under overall and studied wind directions. This was expected as there was only the main trunk or stem of the tree between the bottom of the tree canopy and ground resulting absence of barrier effect and surfaces for deposition in the breathing zone. The changes in PM fractions behind GI in a combination of trees with hedges ( $TH_{IB}$  and  $TH_{CB}$ ) were influenced by either hedges or trees depending on wind directions. During along-road winds, fine ( $PM_1$  and  $PM_{1-2.5}$ ) and coarse ( $PM_{2.5-10}$ ) particle fractions have no considerable variations behind the GI at all sites. Parallel airflow along GI limited penetration of particles into the body of GI and hence minimizing the effect of GI on PM fractions. During cross-wind conditions,  $TH_{CB}$  sites showed a reduction in fine particle fractions behind the GI, indicating filtration of these traffic-originated particles by the hedges at breathing height similar to hedge only sites. While in cross-vegetation winds,  $TH_{IB}$  and  $TH_{CB}$  resulted in a large reduction of coarse particles behind the GI compared to in the front/clear area. The reason could be fresh emissions from neighboring houses or other activities.

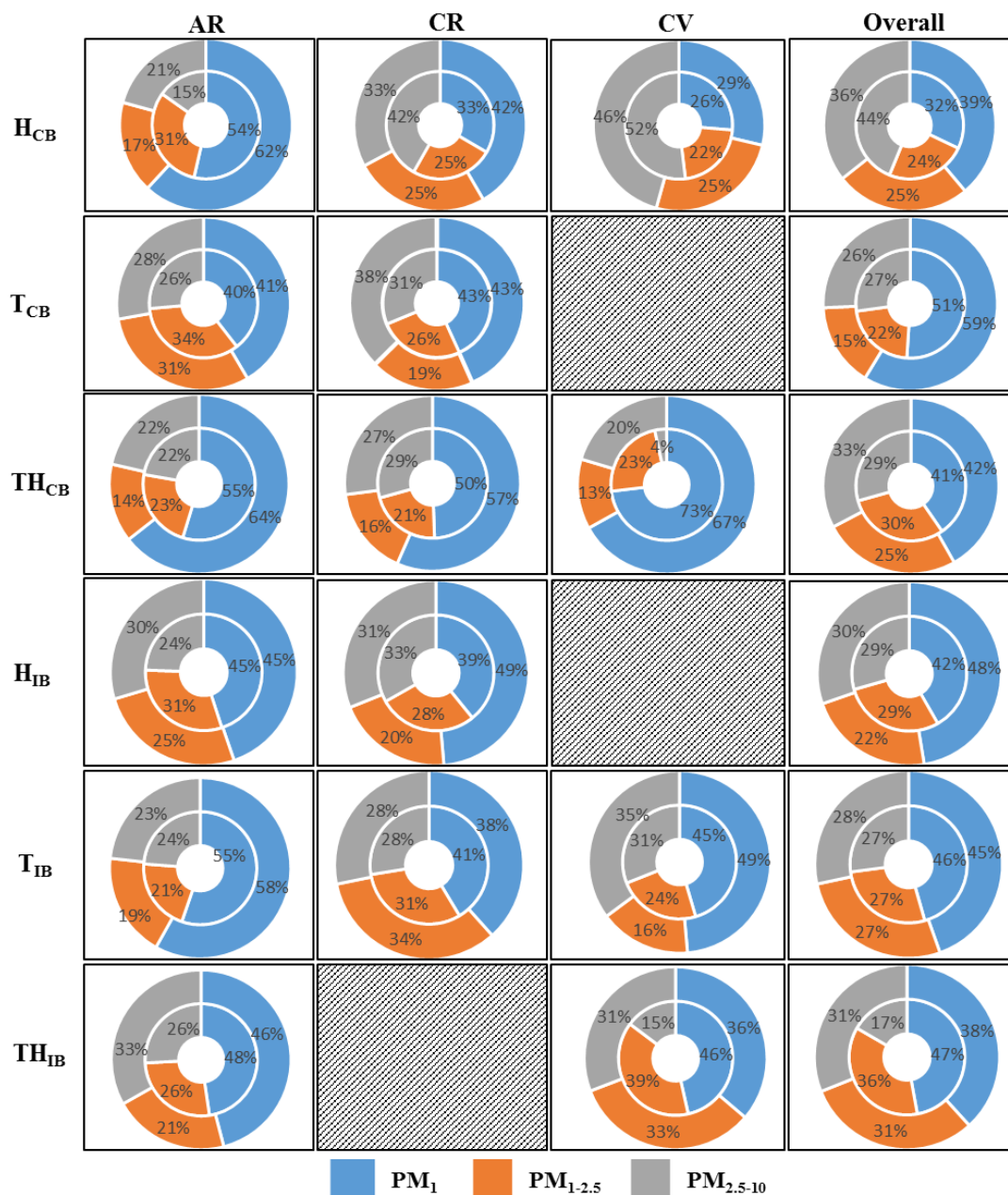


Figure 65: The fraction of various PM types at all the six sites under different wind directions. The inner circle shows PM fractions behind the GI; the outer circle shows PM fractions in-front/clear areas. Blue, orange and grey colours denote PM<sub>1</sub>, PM<sub>1-2.5</sub> and PM<sub>2.5-10</sub>, respectively. Line shading represents a lack of data available in particular situations (Abhijith and Kumar, 2019).

## Elemental composition of individual particles

A total of 10,491 particles at in-front/clear and 9819 particles from behind the GI were identified for analysis. Based on their elemental composition, we classified the particles as natural, vehicle, salt and unclassified. The particles in the natural category were dominated by commonly found earth elements such as Si, Ca, Al, Mg, Fe, K, S and P. Previous studies have identified these elements arising from sources such as road dust and soil (Jancsek-Turóczi et al., 2013; Panda and Shiva Nagendra, 2018). Vehicle particles have either 70% of iron and its oxides or at least



60% of elemental weight compositions of Ba, Cr, Mn, Cu, V and Ti. Vehicle category elements (Fe, Ba, Cr, Mn, Cu, V and Ti) are tracers of vehicular exhaust and non-exhaust emissions (González et al., 2017; Mazziotti Tagliani et al., 2017; Weerakkody et al., 2018). Of these, Ba, Zn, and Cu have been identified as brake lining emissions previous studies (Hays et al., 2011; Moreno et al., 2015). The salt is used on the road for gritting and NaCl crystals were clearly noticeable as perfect cuboids in the collected particles. The rest of the particles were agglomerates of above-mentioned particles and their elemental composition was evenly distributed among them.

While comparing identified particles from behind GI and clear/in-front of GI, natural (+7%) and NaCl (+5%) particles were higher behind GI than those in-front/clear of GI (Figure 66a and b). Conversely, significantly lower percentage of vehicle (−7%) particles were found behind GI than at the other monitoring locations. In terms of particle count, 725 particles out of a total of 9819 particles collected from behind the GI were from vehicular origin as opposed to 1419 from 10,491 particles collected from in-front/clear of GI. This difference indicates the effect of GI in reducing traffic-related emissions. In addition, the fraction of unclassified group, which includes a part of traffic-originated particles, was found to be lower by about 5% behind the GI compared with in-front/clear of GI, further substantiating the potential removal of harmful particles by GI through deposition.

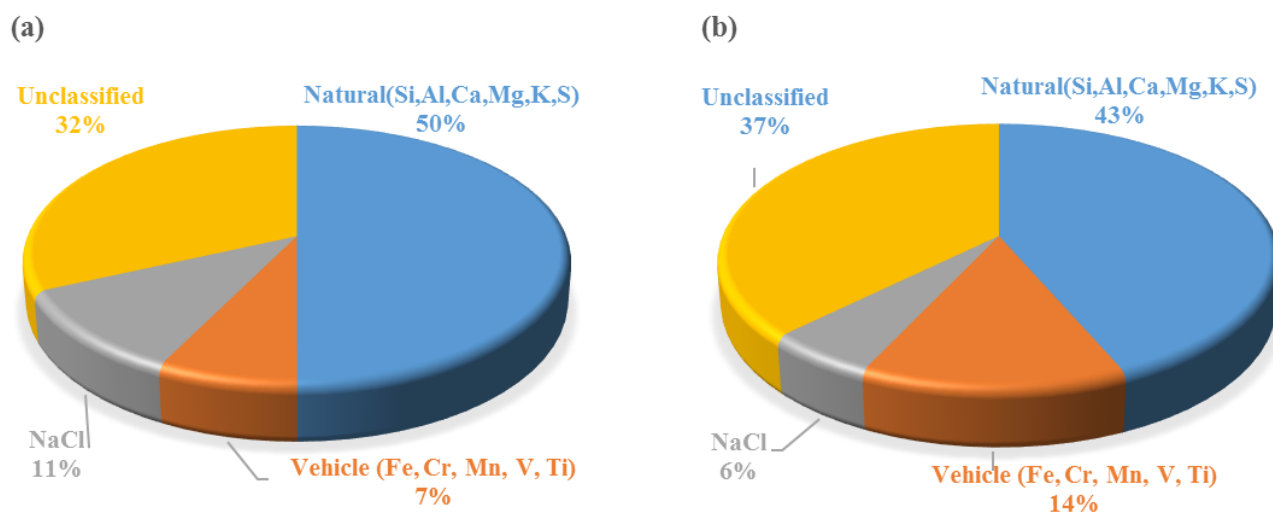


Figure 66: Percentage of samples identified in each elemental composition group in total particles on the PTFE filters (a) behind, and (b) in-front/clear of GI (Abhijith and Kumar, 2019).

#### 4.3.4 Field investigation of apportionment of deposition and dispersion components of air pollution reduction by GI

The following section describes the preliminary results obtained in the recent field experiments aiming at the apportionment of deposition and dispersion components of air pollution reduction by GI. The data analysis is still in progress and we are able to document only preliminary results from the study. Extended results and discussions will be published in Abhijith and Kumar (in prep.) and will feature in D5.4 and D7.2. The summary statistics showing the available number of one-minute averaged data points (N), median, mean and standard deviation of pollutant concentration behind and in-front/clear measurement points at both monitoring sites are listed in Table 7. In most cases, the PM concentration remains almost equal in front and behind locations at clear area site. Whereas the GI site displayed a considerable reduction in all three PM (PM<sub>10</sub>, PM<sub>2.5</sub> and PM<sub>1</sub>) concentrations. Figure 67 shows boxplots of PM<sub>10</sub>, PM<sub>2.5</sub> and PM<sub>1</sub> concentration behind (red) and

in front (green) measurement points at GI site and clear area. In the clear area, the behind (BHD) and in front (BHD) measurement point displayed no significant changes. On the other hand,  $PM_{10}$  recorded maximum reduction in pollutant concentration behind GI compared to in front measurement point and least reduction was observed with  $PM_{2.5}$ . A similar trend in PM concentrations change was observed in a previous field campaign (Abhijith and Kumar, 2019).

	$PM_{10}$				$PM_{2.5}$				$PM_1$			
	GI		Clear area		GI		Clear area		GI		Clear area	
	INF	BHD	INF	BHD	INF	BHD	INF	BHD	INF	BHD	INF	BHD
<b>n</b>	2398	2404	2084	1989	2398	2404	2084	1989	2398	2404	2084	1989
<b>Mean</b>	28.12	25.96	32.64	32.68	20.61	20.07	22.56	23.48	15.64	14.08	16.81	16.46
<b>SD</b>	11.61	9.86	13.57	12.47	8.98	9.89	11.56	12.65	8.63	9.16	9.81	10.44
<b>Median</b>	25.86	23.67	31.05	30.57	19.13	17.86	19.30	19.67	14.56	12.25	13.82	13.38
<b>Min</b>	11.13	10.89	7.42	9.72	7.10	7.74	5.10	6.41	3.02	3.93	2.75	3.08
<b>Max</b>	88.22	68.52	87.47	94.58	59.65	65.51	68.88	63.64	53.42	57.23	55.61	48.44

Table 7: Summary statistics showing total available data from the field campaign. Statistical parameters such as mean, median, standard deviation, minimum and maximum pollutant concentration are tabulated.

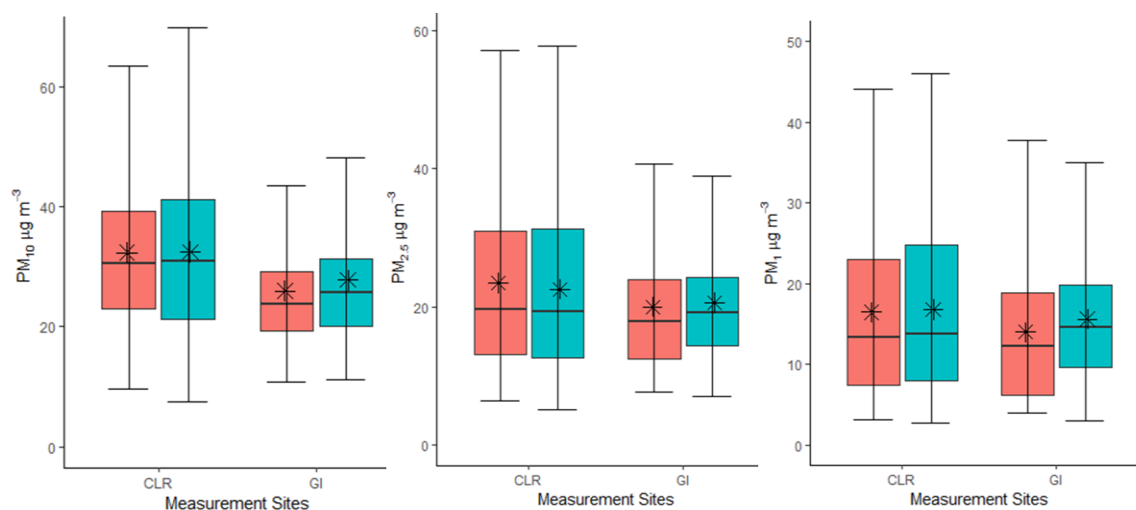


Figure 67: Boxplots of PM concentration behind (red) and in front (green) measurement points at GI site and clear area.  $PM_{10}$ ,  $PM_{2.5}$  and  $PM_1$  are shown from left to right. CLR and GI denote clear area and GI sites, respectively.

Percentage change in pollutant concentration with respect to in front measurement point at clear area and GI site is shown in Figure 68. Presence of GI resulted in a reduction of concentration in all three PM concentrations. Maximum reductions of 10% were observed with  $PM_1$ , followed by 8% with  $PM_{10}$  minimum reported in  $PM_{2.5}$  (3%) in the GI site. Whereas in the clear area, no changes in  $PM_{10}$ , and slight improvement of 2% with  $PM_1$  were reported. In addition, an increase in  $PM_{2.5}$  concentration was observed at behind measuring point in the clear area. We also investigated the

PM fraction in the clear area and GI site, showed in Figure 69. The  $PM_1/PM_{2.5}$  and  $PM_{2.5}/PM_{10}$  ratios were similar in both GI and clear area sites. Further analysis of data will provide a better understanding of differences in dispersion in the GI site and clear area. These will be reported in the article in preparation by Abhijith and Kumar (in prep.) and key recommendations based on those findings will be reported in D7.2.

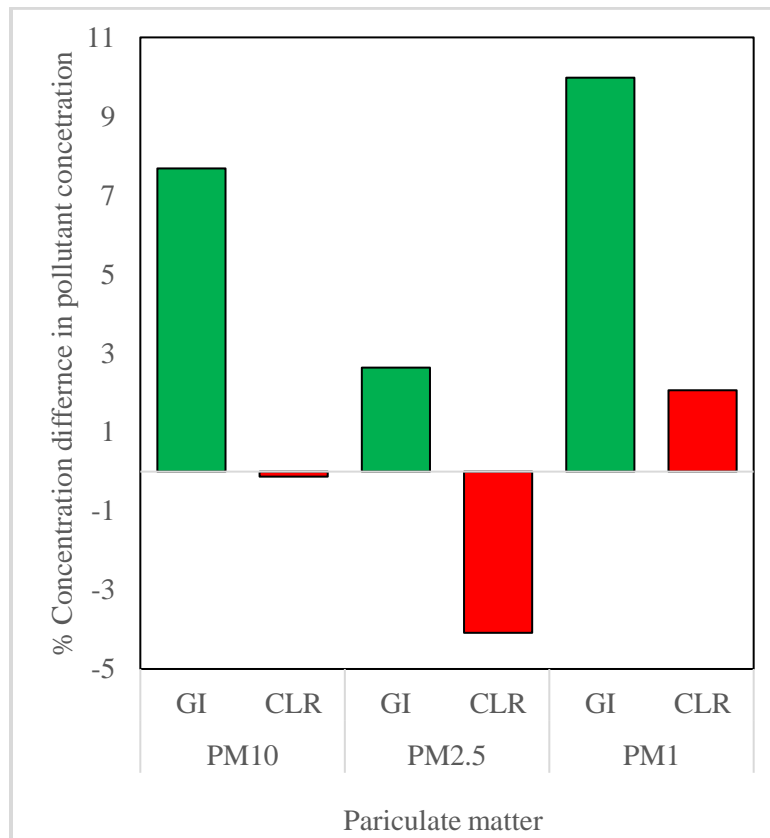


Figure 68: Percentage change in concertation of PM at behind measurement point compared to that of in front, at clear area and GI site  $\{[PM_{INF}-PM_{BHD}] \times 100/ PM_{INF}\}$ .

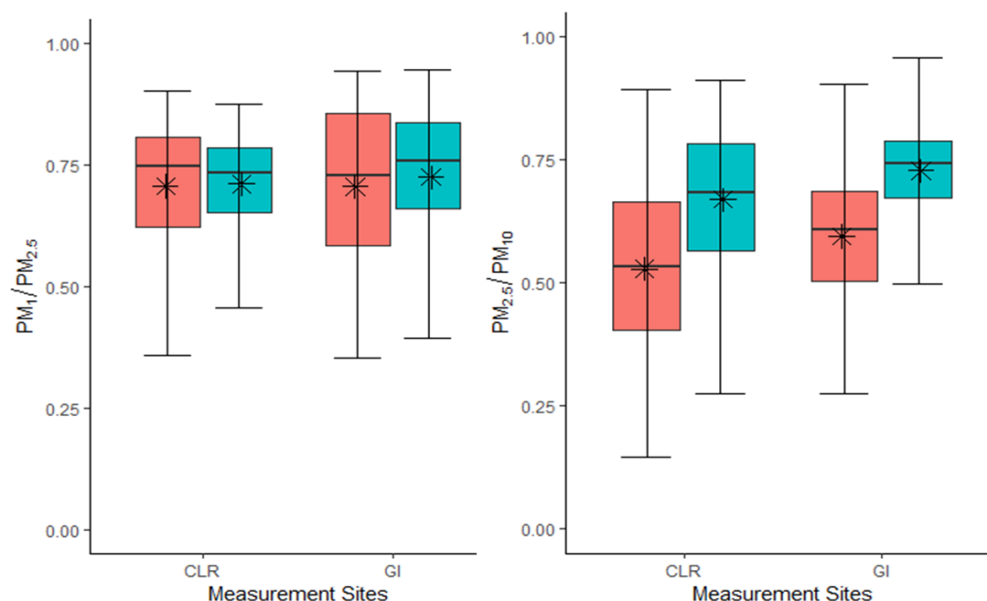


Figure 69: The ratios of (left)  $PM_1/PM_{2.5}$  and (right)  $PM_{2.5}/PM_{10}$  at the studied GI and Clear area sites.

### 4.3.5 Results and observation from citizen sensors quality control measures

This section gives details about the results of the field study. The summary statistics showing the median, mean and standard deviation of pollutant concentration for GRIMM and ten SC kits is shown in Table 8. The results are very similar for  $PM_1$  and  $PM_{10}$ , as can also be further observed in the correlation plots (Figure 70 and Figure 71).

		GRIMM	S1	S2	S3	S4	S5	S6	S7	S8	S9	S10
$PM_1$	Mean	3.59	3.12	2.86	3.09	2.68	2.76	3.6	2.58	2.56	3.26	2.67
	Median	2.94	2.5	2	2	1.5	2	2.5	1.5	1.5	2	2
	SD	1.80	2.67	2.51	2.66	2.53	2.61	3.18	2.49	2.57	2.79	2.50
$PM_{2.5}$	Mean	6.74	4.60	3.93	4.63	4.22	3.77	4.62	4.22	4.11	4.31	3.79
	Median	6.03	3.5	2.5	3.5	3	2.5	3.5	3	2.5	3	2.5
	SD	2.55	3.47	3.32	3.50	3.50	3.31	3.85	3.48	3.42	3.52	3.23
$PM_{10}$	Mean	20.73	5.04	4.10	5.37	4.67	4.13	4.93	5.54	4.78	4.62	4.23
	Median	18.91	4	3	4	3	3	3.5	4	3.5	3.5	3
	SD	9.18	3.75	3.31	3.98	3.79	3.45	4.01	4.22	3.81	3.65	3.42

Table 8: Summary statistics showing the statistical parameters such as mean, median and standard deviation (SD) for  $PM_1$ ,  $PM_{2.5}$  and  $PM_{10}$ .

The correlation plot (Figure 70) shows a good correlation between the GRIMM measurements and SC kit measurements. Results show that the correlation was between 0.76 and 0.82 for  $PM_{2.5}$  measurement. The correlation was also observed for  $PM_1$  and  $PM_{10}$ . For  $PM_1$ , the results showed a correlation between 0.82 and 0.89 (Figure 71 (a)) whereas for  $PM_{10}$  the correlation was between 0.51 and 0.56 (Figure 71 (b)).

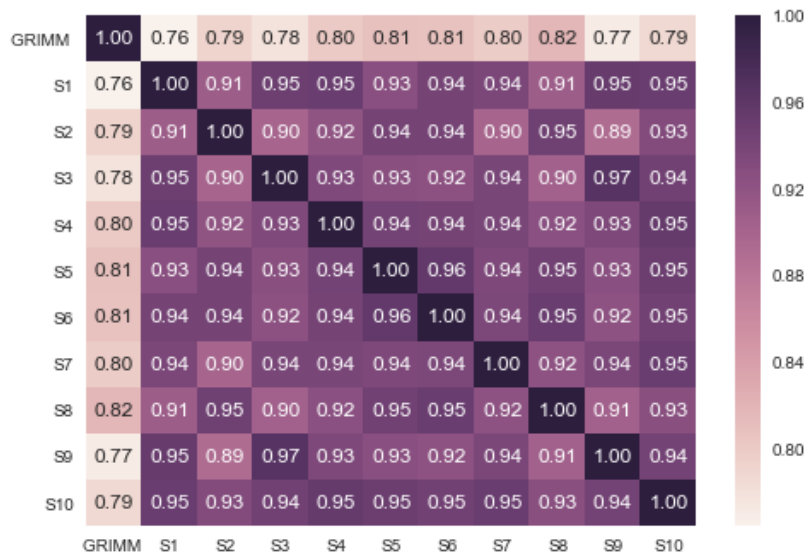


Figure 70: Correlation plot between the GRIMM and ten SC kits for  $PM_{2.5}$  measurement.

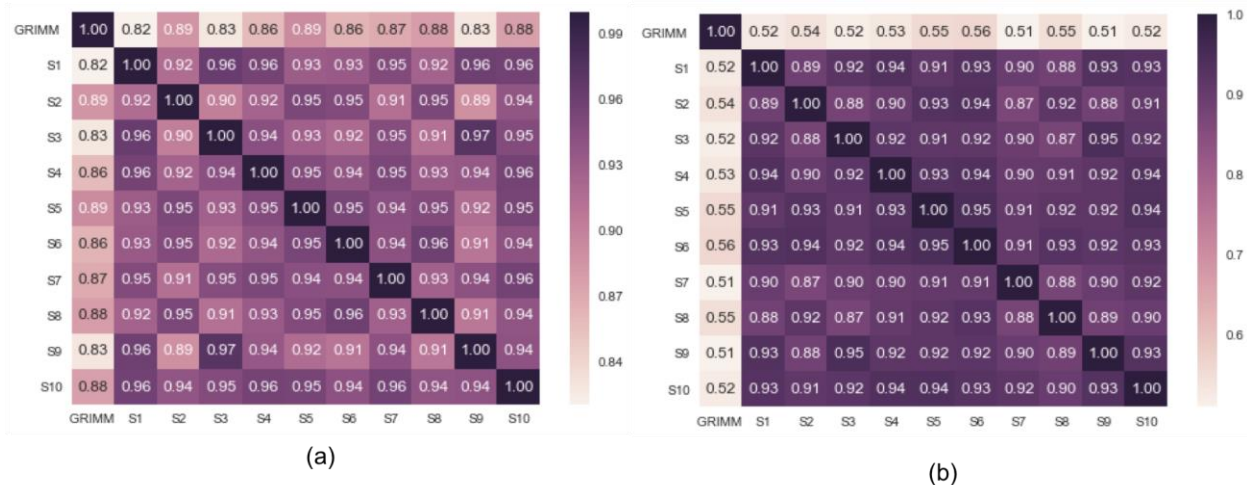


Figure 71: Correlation plot between the GRIMM and ten SC kits for (a)  $PM_1$  measurement and (b)  $PM_{10}$  measurement

During the whole measurement period, the trends of outputs from SC kits were very similar to GRIMM data for  $PM_1$  and  $PM_{2.5}$ . An interesting observation is that the occurrence of episodes of higher  $PM_{2.5}$  concentrations could be monitored by the SC kits and the error was significantly low. In Figure 72 it can be observed that all the ten SC kits show very similar behavior to the GRIMM for  $PM_{2.5}$  and that the measurements follow a similar trend for all the sensors.

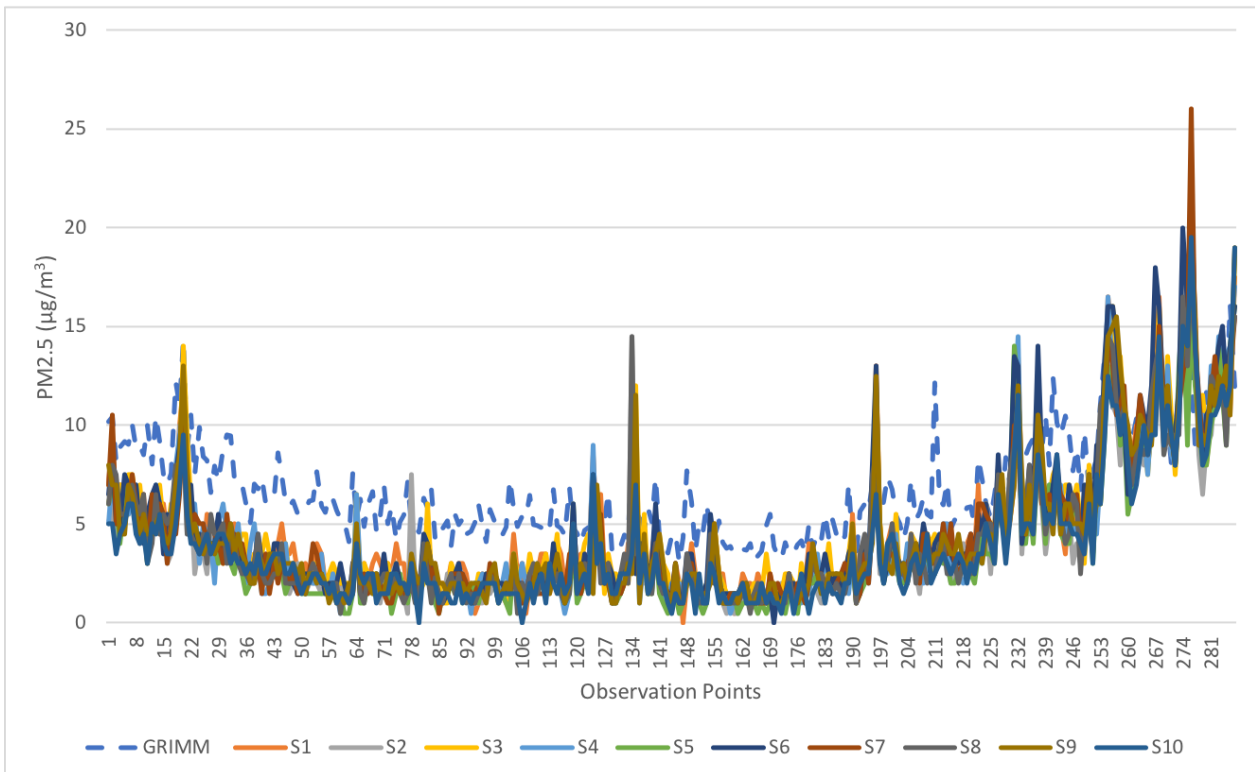


Figure 72: Plot showing  $PM_{2.5}$  measurement by the GRIMM and ten SC kits. Almost similar trends in the  $PM_{2.5}$  level fluctuations can be observed from the figure.

This campaign was performed before the Citizen Science workshops (D4.7 ‘*Citizen science communities report*’). A similar campaign is underway for the same sensors and the results would provide an insight into SC kits performance after almost fifty hours of usage. The results of this work combined with the ongoing campaign will be reported in D7.8 (‘*Sensor monitoring experience and technological innovations*’).

## 4.4 Vantaa

### 4.4.1 Meteorological and air quality data

At both iSCAPE - monitoring station Malminiitty and Heureka high quality meteorological data was collected with one second time resolution. This means that our data collection process was over 100-times denser than the official procedure of FMI. This can cause differences in data averaging and extreme values. To avoid this problem the near-by synoptic weather station (see Figure 17 in section 3.5.1) at the airport Helsinki-Vantaa was used as a reference station. The comparison between the datasets is shown in Figure 73. Due to the shortness of the data series no statistical test was used.



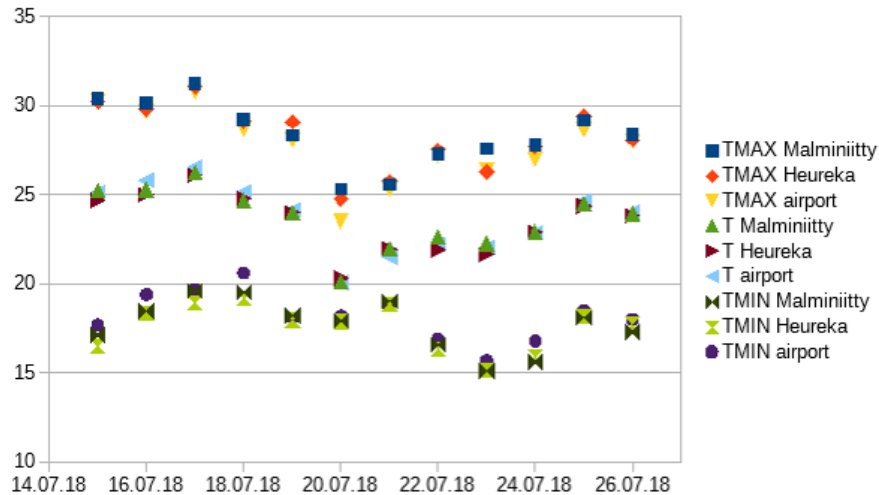


Figure 73: Comparison of daily air temperature averages (T), highest air temperatures (TMAX), and lowest air temperatures (TMIN) of the stations Malminiitty, Heureka, and Helsinki-Vantaa airport (airport) for the period July 14th - 26th 2018.

Another parameter presenting a very similar distribution to the air temperature is the incoming solar radiation (Figure 74). The final amount of solar radiation received depends on the exposition of the instrument, cloudiness and atmospheric composition. Normally the instrument is exposed unlimited to the sky. This is the case at Heureka, where the instrument is mounted at 10 meters height. For Malminiitty we took an intended restriction by mounting the instrument at 20 meters height facing it into the courtyard. In summertime after approximately 16:00 the instrument is shaded by the building where the monitoring station is located.

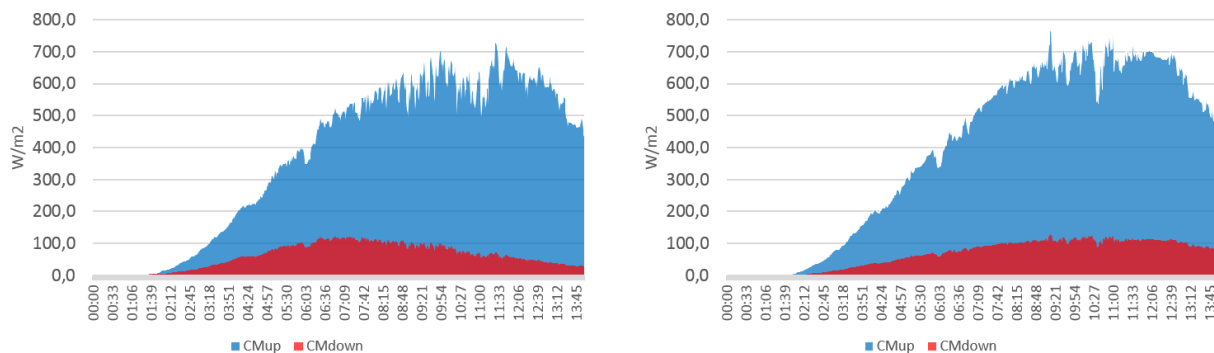


Figure 74: 1-minute average of solar incoming shortwave radiation (blue) and reflected shortwave radiation (red) at iSCAPE monitoring station Malminiitty (left) and Heureka (right) for the period July 14th - 26th 2018.

The shift of the reflected shortwave radiation to an earlier maximum at Malminiitty is due the orientation of the instrument.

Another very typical phenomenon of meteorological parameters is the behavior of average wind speed and wind extremes (Figure 75). On one hand in build-up areas the wind speed decreases due to the roughness of the surface, on the other hand buildings force the wind through narrower street canyons.

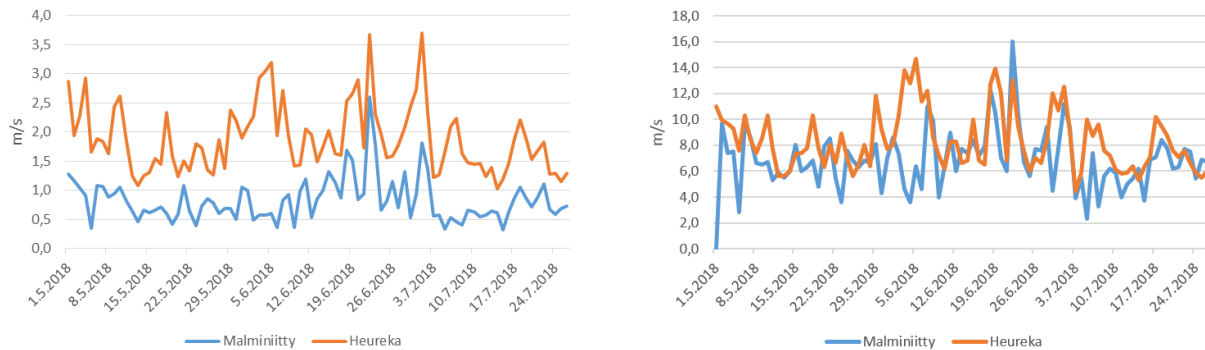


Figure 75: Mean wind speed (left) and daily maximum wind speed (right) at iSCAPE monitoring station Malmiiniitty (blue) and Heureka (red) for the period May 1st - July 26<sup>th</sup> 2018.

During the summertime, normally, there are no air pollution issues in Finland. In the cities, the traffic emissions are reduced due to the long vacation period from June to August. Problems might occur during hot and dry summers, when forest fires, both local as well as distant, may add huge amounts of small particles into the lower atmosphere. In the worst cases, the visibility can be reduced. In the Helsinki metropolitan area, a network with seven permanent and four temporal stations is operated by HSY (see section 3.5.2). As previously reported, the stations are equipped with different sensors to monitor several traffic-related pollutants and particulate matter in different sizes. The following figures present the measurements collected during the experimental campaign.

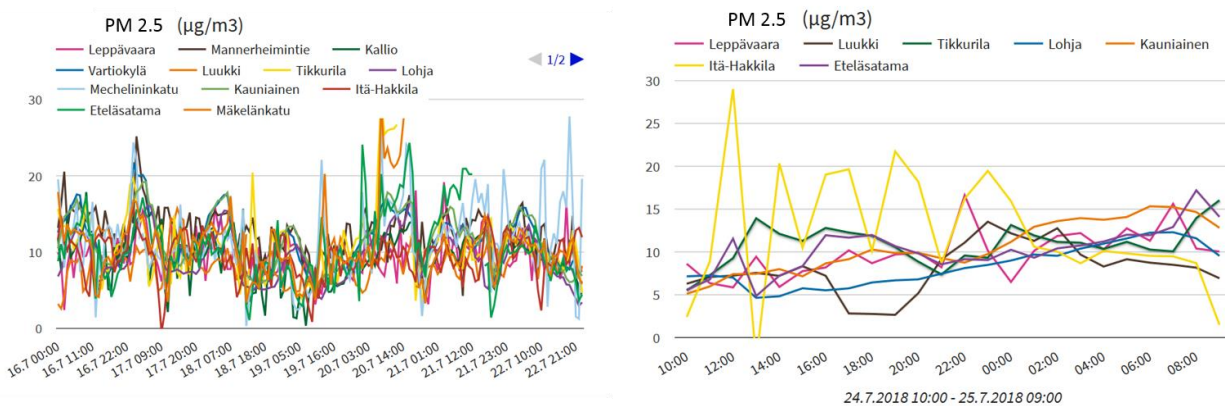


Figure 76: Results from the HSY air pollution network monitoring stations, left: weekly  $PM_{2.5}$  measurements from 12 air pollution stations (HSY and Lohja), July 16<sup>th</sup> - 22<sup>nd</sup> 2018; right: detail of 24-hour  $PM_{2.5}$  measurements from 7 stations in the metropolitan area, July, 25<sup>th</sup> 2018 (source: HSY).

The daily  $PM_{2.5}$  concentrations show a distinguished distribution between traffic and residential areas, where in some cases the concentrations can be twice as high as in traffic areas (Figure 76). This is obvious for detached houses areas where it is common in Finland to have wood-fired saunas and furnaces.

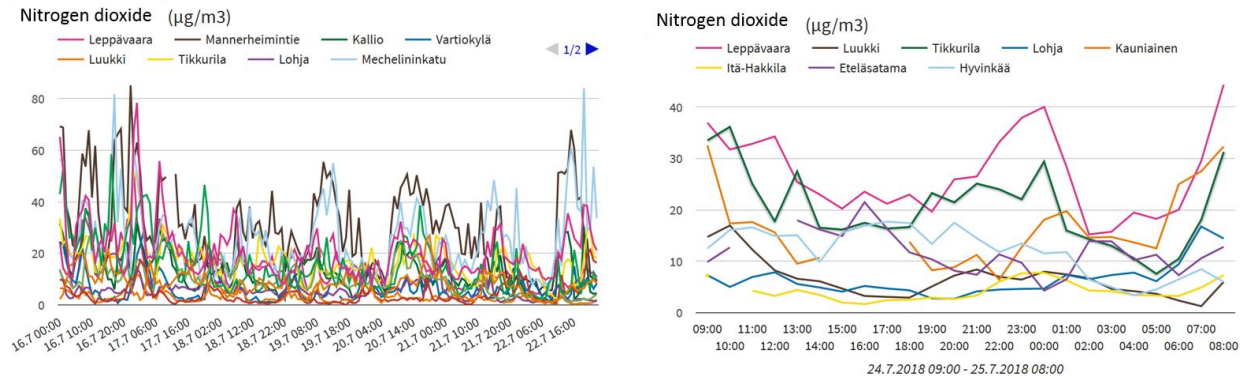


Figure 77: Results from the HSY air pollution network monitoring, left: weekly nitrogen dioxide measurements from 12 air pollution stations (HSY and Lohja), July 16th - 22nd 2018; right: detail of 24-hour nitrogen dioxide measurements from 8 stations in the larger metropolitan area, July 25th 2018 (source: HSY).

The amount of nitrogen dioxide in the air is directly related to the amount of traffic in the area. Areas with intense traffic like Mannerheimintie and Mechelininkatu in the downtown area of Helsinki measured concentrations almost always twice as high as the other measuring points (Figure 77, left). In detached houses areas like Itä-Hakkila the measured values dropped down to one third or one fourth (Figure 77, right).

In the following, we describe the overall and mean statistics of meteorological and air quality data in Vantaa in 2018 (a full year of iSCAPE measurements). We examine the city center and rural Vantaa (VantaaCentre and VantaaEast in the figures), but for comparison purposes we show also air quality from the Helsinki city center (HelsinkiCentre), which is known to be the area of the worst air quality in the capital Finland. The hourly measurements are shown in Figure 78 and the monthly and hourly means in Figure 79 and Figure 80, respectively. The largest NO<sub>2</sub> concentrations are observed mainly in early year (Jan-May) in 2018. PM<sub>2.5</sub> concentration peaks in July in all examined areas.

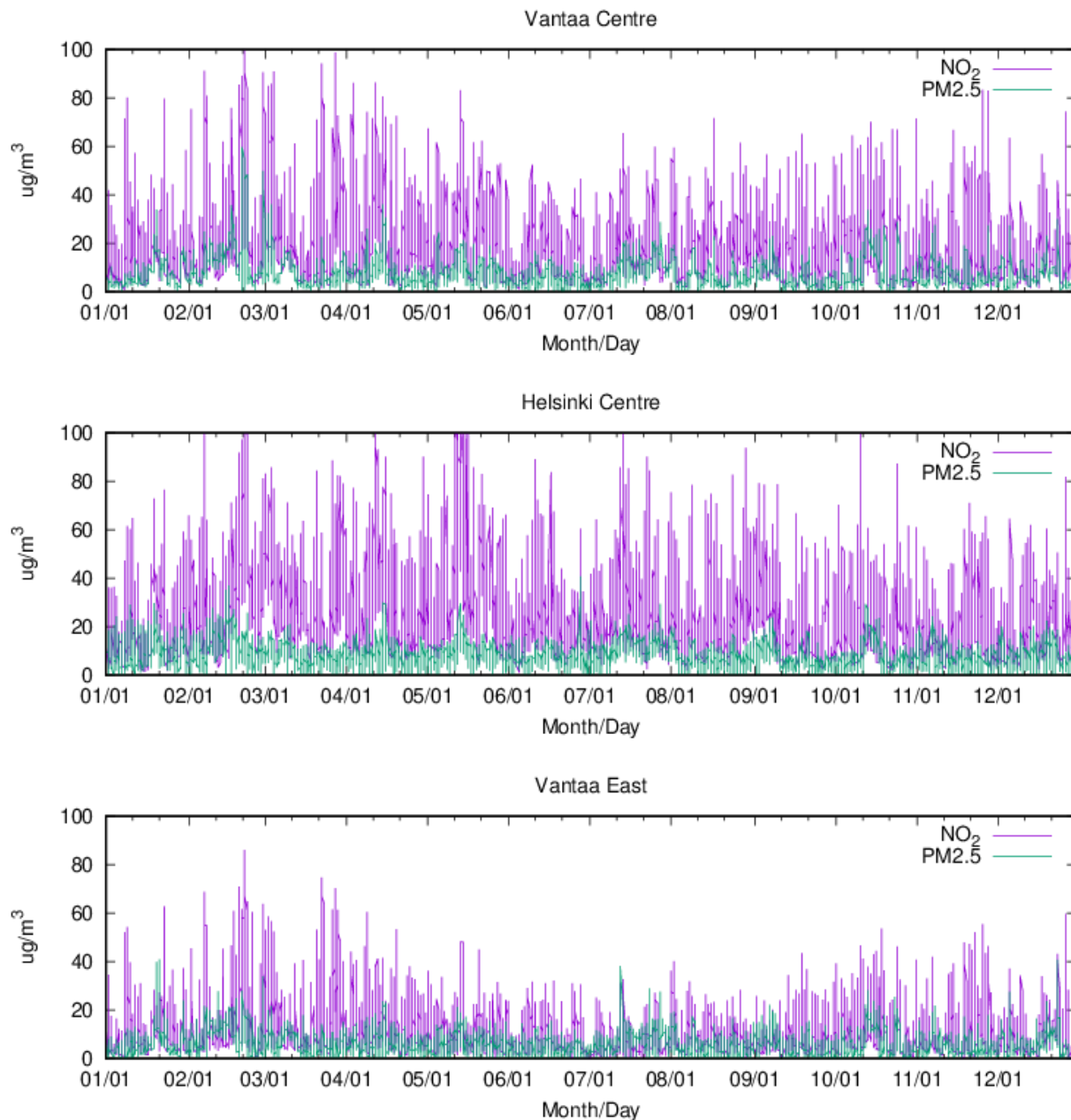


Figure 78: Hourly NO<sub>2</sub> and PM<sub>2.5</sub> concentrations in Vantaa (city center, uppermost; rural, lowermost) and in the center of Helsinki (middle) in the period 01/01-31/12/2018.

The mean diurnal distribution of NO<sub>2</sub> concentration (Figure 80) shows that the peak in Vantaa is observed in the morning hours (8 to 10 am local time) and lowest values during the night. In Helsinki, the morning peak is two hours later. Regarding PM<sub>2.5</sub> (Figure 58), the diurnal mean distribution shows a small peak in the Vantaa center in the morning, and a small drop in the same time in the rural Vantaa and Helsinki center. Towards the evening and midnight, the concentrations slowly increase in all three areas. The role of low temperatures and low wind speeds are clearly observed also in case of NO<sub>2</sub> and PM<sub>2.5</sub> concentrations (Figure 82): the largest hourly concentrations occur in low temperature and low wind speed situations generally caused by nighttime inversions.

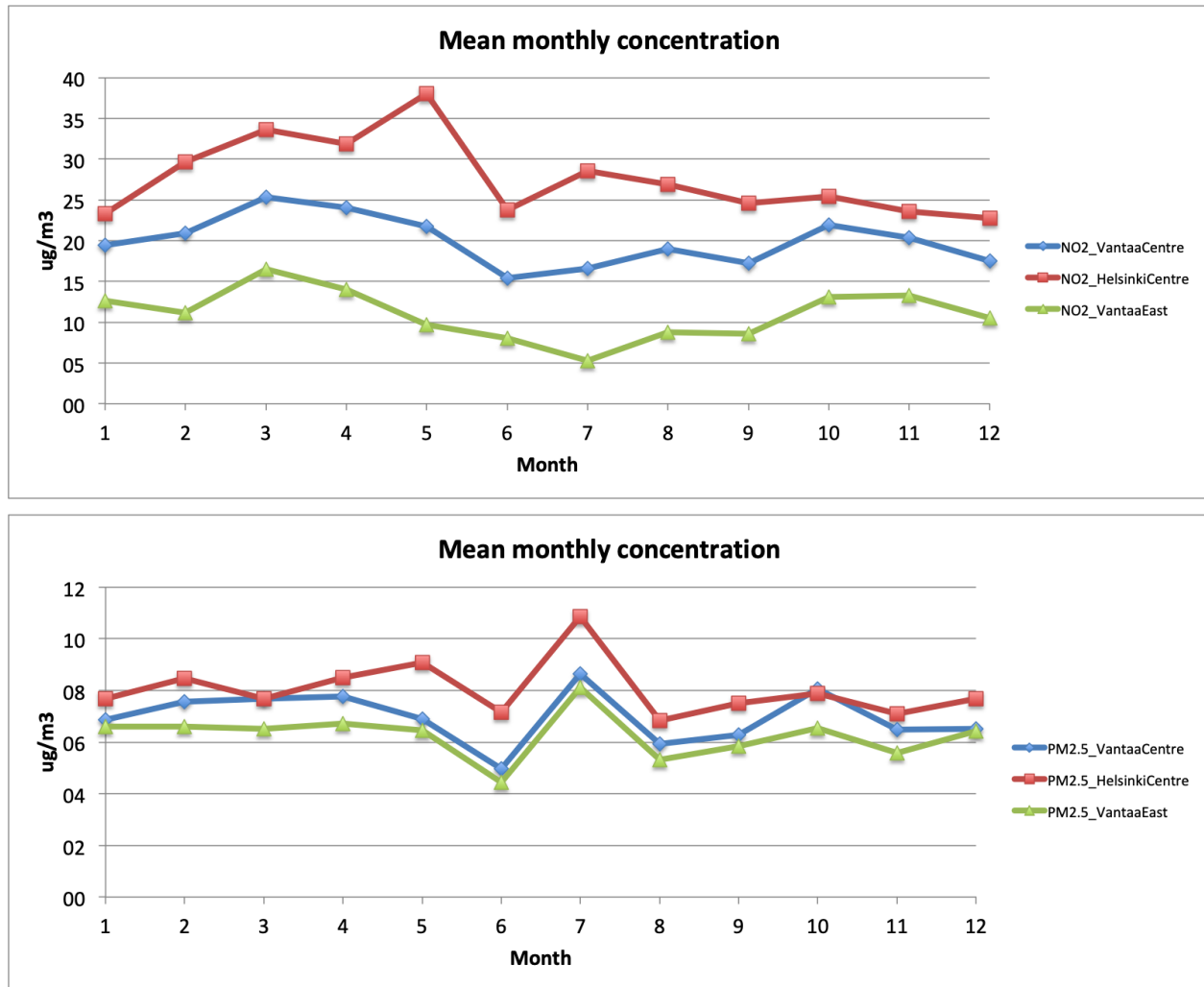


Figure 79: The monthly mean NO<sub>2</sub> (upper) and PM<sub>2.5</sub> concentrations in Vantaa and Helsinki in 2018.

In 2018, the largest NO<sub>2</sub> and PM<sub>2.5</sub> concentration values were observed on 22 Feb (Figure 81). The 2m-temperature evolution in Figure 81 indicates low temperatures during the night and morning hours (about -20°C), followed by midday and afternoon warming (about -8°C at maximum) and cooling towards the evening. To the opposite, the NO<sub>2</sub> and PM<sub>2.5</sub> concentrations are high in the night and morning hours with a sharp drop coinciding with the increasing temperature.

The pattern described above is typical for Finland and represents a routinely occurring episode during the winter. The nighttime temperature inversion efficiently caps the air pollutants in the boundary layer, while the midday warming (or increasing winds/turbulence) rapidly breaks the inversion leading to drop in the air pollutant concentrations. Furthermore, in cities like Vantaa, fireplaces are in heavy use under this kind of cold situations, leading to increased pollutant concentrations.

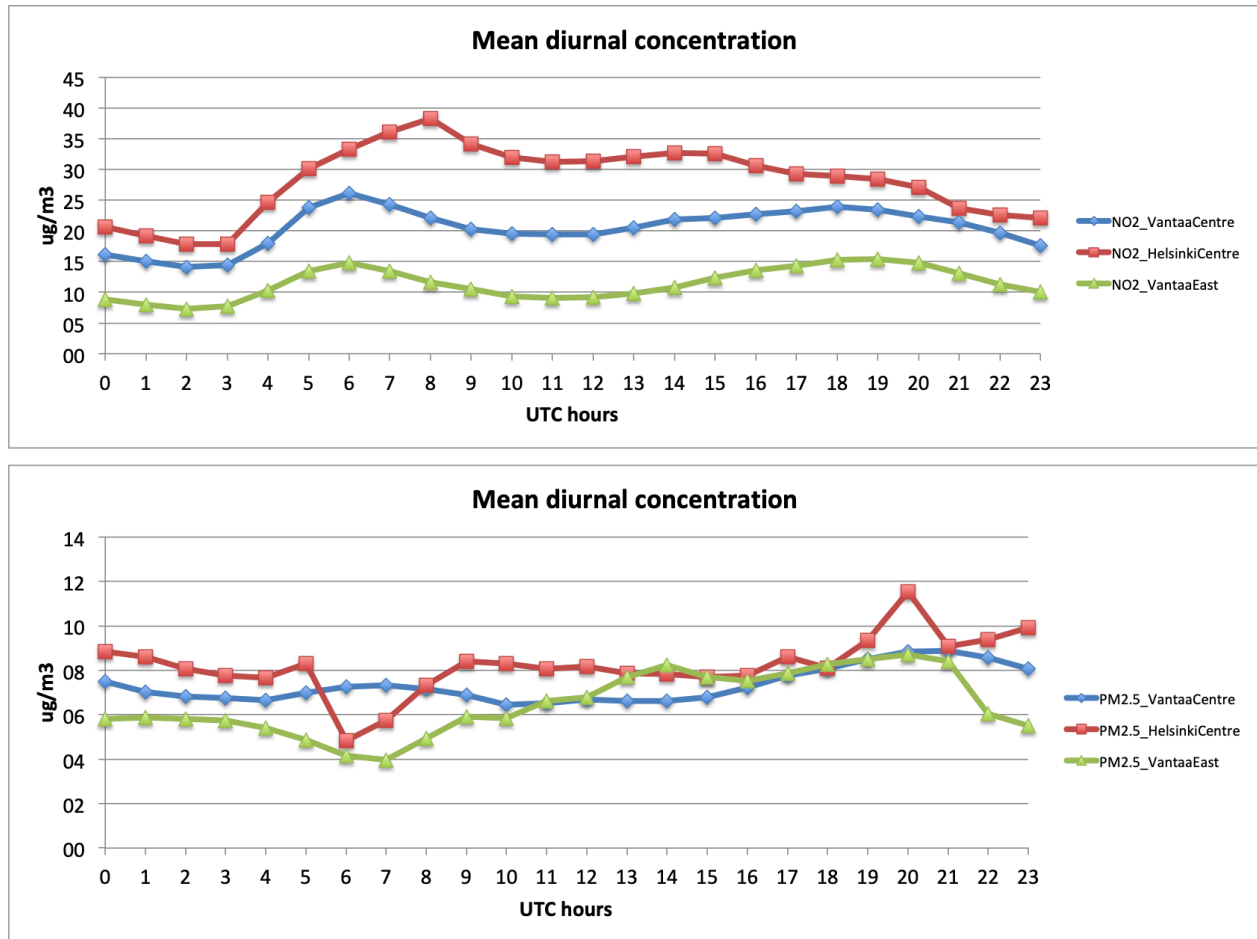


Figure 80: The mean hourly NO<sub>2</sub> (upper) and PM<sub>2.5</sub> (lower) concentrations in Vantaa and Helsinki in 2018.

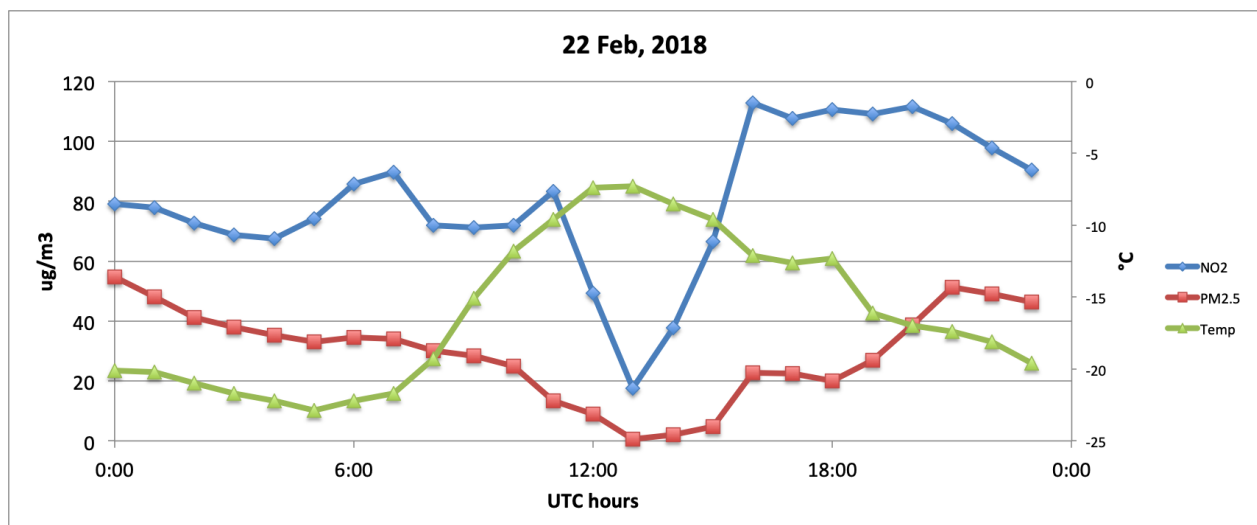


Figure 81: Hourly distribution of NO<sub>2</sub> and PM<sub>2.5</sub> concentrations and 2m-temperature in the Vantaa Centre on 22 Feb 2018. This day presented the highest hourly NO<sub>2</sub> and PM<sub>2.5</sub> concentrations in 2018. Local time is UTC+2 in winter.



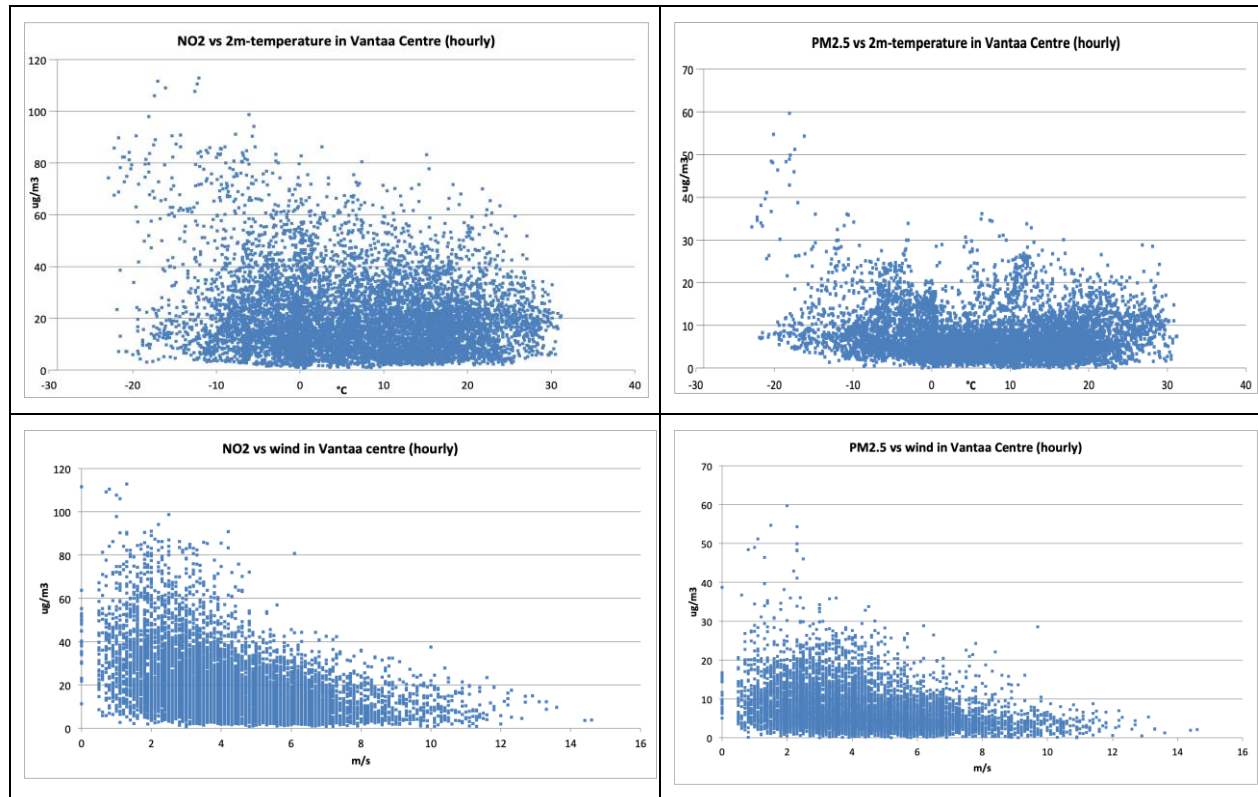


Figure 82: Hourly concentrations of NO<sub>2</sub> and PM<sub>2.5</sub> in 2018 with respect to 2m-temperature (upper row) and wind speed (lower row).

## 5. Conclusions

Within the iSCAPE project, various experimental campaigns were setup in the pilot cities with the aim to analyze meteorological and air pollution levels, for further use to verify and calibrate simulations run as part of other tasks and in WP4 and WP6 to evaluate the effect of policy and infrastructural interventions, but also with the aim evaluate the efficacy of PCSs to improve air quality and urban thermal comfort at local level. In addition, those campaigns served also as means to calibrate low-cost sensors developed within the project both with the aim to support and integrate measuring campaigns as well as to organize local citizen science initiatives, which will be the objective of D4.7 (*'Citizen science communities report'*).

As such, the two versions of this Deliverable intend to illustrate the instrumental setup adopted within the experimental field campaigns, to document the data gathered and to present the results obtained in terms of air pollution and meteorological monitoring in four iSCAPE cities, namely Bologna, Dublin, Guildford and Vantaa.

In Bologna, the monitoring of meteorological and air pollution levels was conducted during two intensive experimental field campaigns, one in summer 2017 and one in winter 2018. The campaigns were conducted at two urban street canyons characterized by the same orientation, but different presence of vegetation. As shown in the first version, the monitoring involved the measurement of various meteorological and turbulence parameters, measured at high time resolution, in addition to various air pollution pollutants. Two intensive thermographic campaigns were also carried out, in order to analyze and characterize the temperature distribution and the UHI effect at the city scale. While the first version, besides presenting comparison between the

meteorological, turbulence and air pollution levels observed in the two street canyons, documented the positive effect of trees in improving thermal comfort at neighborhood level in the summer period, in the updated version we presented further analyses aimed to better document all the work carried out with the dedicated instrumental setup. In particular, data gathered with the ceilometer installed on the rooftop of the Department of Physics and Astronomy of the University of Bologna allows for the evaluation of the boundary layer height at urban level, a parameter of fundamental importance when analyzing air pollution. Our results show in fact that the diurnal pattern of gaseous pollutants observed at all the air quality stations in Bologna comprising also the two mobile stations in the two urban street canyons is governed by the boundary layer height dynamics; conversely, the diurnal pattern of particulate matter concentrations, reconstructed from the observations carried out with two optical particle counters, is different and evidences local specific patterns and singularities driven by other factors.

As in the first version of the Deliverable it was noted that the differences in air pollution levels observed in the two urban street canyons are linked not only to the differences in vegetation but also to different traffic volumes, fleet composition and the different geometry of the two canyons, an algorithm was developed to remove the effect of other confounding factors. The comparison of normalized  $\text{NO}_x$ , CO and estimated  $\text{PM}_{2.5}$  (for winter only) concentrations shows in general lower concentrations in Laura Bassi, possibly depending on the effect of trees, while the existence of contemporary spikes at the two sites reveal again the existence of common forcings independent on the traffic source. Reductions in normalized concentrations at Laura Bassi street canyon, attributed to the pollutant removal efficiency of trees, were calculated for two different periods, one in summer 2017 and one in winter 2018: results show larger reductions (-23% for  $\text{NO}_x$  and -10% for CO) for gaseous pollutants in the warm period when deciduous trees are covered with leaves, while important reductions for particle pollution are also observed during wintertime. Dependence on wind configurations was analyzed as well, indicating larger reductions under katabatic and downwind conditions.

Finally, in this version, vertical mass exchanges in two street canyons in Lazzaretto were analyzed. Indeed, while the campaign at Lazzaretto site in the outskirts of Bologna was primarily aimed at testing the efficacy of photocatalytic coatings in removing  $\text{NO}_x$  pollutants in a real environment, as thoroughly documented in D3.8 (*'Report on deployment of neighborhood level interventions'*) and D3.6 (*'Report on photocatalytic coatings'*), the particular configuration of Lazzaretto similar to an open-air laboratory gives the opportunity to test different atmospheric processes in a controlled environment. Air mass exchange processes were evaluated by means of the coupling of an open-path  $\text{CO}_2$  and  $\text{H}_2\text{O}$  gas analyzer with the sonic anemometer located on the rooftop of one of the two canyons in Lazzaretto. The impact of turbulent ventilation on  $\text{CO}_2$  removal, which can be extended to all pollutants with atmospheric lifetime much larger than the turbulent timescales, was analyzed with the quadrant analysis, which documented the largest ejection phenomena under downwind conditions, while in the anabatic cases sweep and ejection have almost equal efficacies.

The assessment and evaluation of the Dublin LBW intervention is built upon two evaluation methods, which are being implemented as part of iSCAPE project. Firstly, a measuring study for the real-world LBW application in Dublin (which is partially presented in this report) and, secondly, a CFD modelling study of the street canyon before and after the LWB intervention, which will be presented as part of WP6. For the purpose of evaluating the potential of using LBW, changes in nitrogen oxides were monitored at two monitoring points on each side of the LBW, during two experimental campaigns, one in winter and one in summer. This report provides results related to the effects of the LBWs on the dispersion of  $\text{NO}_x$  gases based on different sets of wind directions in a street canyon geometry. Based on the results presented in this report, one can conclude that LBWs act as a baffle at street level and increase the distance between the pollutant source and human receptor. LBWs can provide a solution to enhance localized dispersion and improve air

pollution in distinct street canyons settings. However, depending on the wind direction, street geometry and position of the LBW, they may also cause air pollutant concentrations to increase behind the LBW, having the opposite effect of increasing pollutant concentrations instead of decreasing them. The results indicate that for  $PM_{2.5}$  the LBWs were not having an effect on the dispersion of the pollutant and the average percentage difference between both the sides of the walls was almost similar for both the case when LBWs were present or not. Therefore, the walls were not effective in altering the concentration of  $PM_{2.5}$  behind the walls. However, for  $PM_{10}$ , the results show that the walls modify the dispersion of the pollutant. As the maximum decrease in concentration was 59 % in presence of the LBW. Conversely, without any wall, the maximum increase was 190%.

Guildford field campaign investigated various pollutant concentration differences in the presences of three vegetation types such as Hedges, Trees and their combination. While in the first version of the Deliverable changes in pollutant concentrations due to the presence of PCSs were estimated by comparing measurements of behind vegetation with a monitoring point at a clear area or in front of vegetation, this updated version mainly contains new results obtained analyzing the data from low-cost sensors with advanced statistical algorithms to detect erroneous data and to fill the gaps, in colocation experiments of low-cost sensors with reference instrumentation, and analyzing the differences in particles' size distribution and composition behind, in front and in the absence of GI. The main new conclusions of the Guildford field campaigns are:

- Erroneous data in low-cost air quality sensors can be detected in a fully automated way (QC) and contextual outlier detection can be applied to low-cost air quality data and yield meaningful results. Gap filling for air quality time series is challenging and still requires more research. Two Living Lab stations have been mounted on each side of a hedge in Guildford, and the initial results show a good association for particles between the two stations.
- The assessments based on wind directions revealed a maximum reduction in pollutant concentration during along-road wind conditions, followed by cross-road wind conditions, showing up to a 52, 30, 15, 17 and 31% reduction for BC, PNC,  $PM_{10}$ ,  $PM_{2.5}$  and  $PM_1$ , respectively. No change in PM fractional composition was observed behind the GI in the presence of trees. However, both the hedge-only and trees with hedges scenarios resulted in lower fractions of sub-micron particles. The SEM single particle analysis showed a reduction in traffic-related particles (vehicle; -7%) in samples taken from behind the GI compared to those taken in front of or clear area adjacent to GI. In addition, naturally occurring particles were dominant behind the GI (7%) and agglomerates of particles originating from natural and vehicular sources were lower (-5%) behind the GI. Ongoing data analysis of second field investigation revealed effectiveness in reducing particulate matter in presence of GI compared to clear area.
- Low-cost sensors like the SC kits can provide reliable air quality data which can actually help in sensing air quality data and a finer spatio-temporal resolution. The initial results after colocation experiments show good results for  $PM_{2.5}$  and  $PM_1$ . These low-cost sensors may catch sudden variations in the concentration levels which have been highlighted in case of  $PM_{2.5}$  during peak and off-peak hours.

Vantaa field campaign investigated the effect of different PCSs such as trees and bushes to support urban high-resolution modeling (ENVI-MET). Two experimental sites were equipped with the same instrumental setup in order to collect meteorological data (wind speed and direction, rain intensity and duration, air pressure, and the four components of the energy radiation spectrum) with a high time resolution at two sites characterized by the presence of different PCSs nearby. Additionally, air pollution data were available from HSY stations located nearby. While the

meteorological and air pollution data are being used as an input to the ENVI-MET simulation, the cross-comparison between the data collected at the two sites enables for studying the effect of PCSs and of mounting conditions on the measurements. The analysis of meteorological and air quality data for 2018 show that in general the air pollution levels in Vantaa are relatively low compared to other iSCAPE cities. However, poor air quality conditions occur during the wintertime in low temperature and wind speed conditions due to nighttime inversion. With this respect, policy interventions could help in mitigating the poor air quality by, for example, regulating the car traffic and use of fireplaces in these situations.

Data collected in-situ were further used to complement and validate the simulations conducted as part of WP4 and WP6 with the purpose to evaluate the effects of different policy scenarios and PCSs in terms of air pollution and climate change. The simulations will thus project the in-situ knowledge derived from the results of the campaigns herein presented to larger scales, in order to extend the impact of the interventions. Besides the monitoring of the interventions as in this report, WP5 also addresses their evaluation and the optimization, in particular through D5.3 (*'Evaluation of the interventions'*) and D5.4 (*'Strategic portfolio choice'*) which will report detailed evaluation of the interventions and their optimal use and impacts, also under a socio-economic perspective. These results will also provide input to WP7 by making available data about the costs and benefits of the interventions so as to help the development of the sustainability and exploitation strategy of iSCAPE. Finally, WP5 will also ensure the continuity of the Living Labs (D5.5 *'Plan for extending the life of Living Labs beyond iSCAPE'*).

## 6. References / Bibliography

- ABHIJITH, K. V. & KUMAR, P. 2019. Field investigations for evaluating green infrastructure effects on air quality in open-road conditions. *Atmospheric Environment*, 201, 132-147.
- ABHIJITH, K. V. & KUMAR, P., in prep. Field experiments investigating Deposition and Dispersion Components of Air Pollution Reduction by Green Infrastructure. *Atmospheric Environment*.
- ALAVI-SHOSHTARI, M., SALMOND, J. A., GIURCĂNEANU, C. D., MISKELL, G., WEISSERT, L. & WILLIAMS, D. E. 2018. Automated data scanning for dense networks of low-cost air quality instruments: Detection and differentiation of instrumental error and local to regional scale environmental abnormalities. *Environmental Modelling & Software*, 101, 34-50.
- BARBANO, F., BRATTICH, E., & DI SABATINO, S., submitted. Characteristic scales for turbulent exchange processes in a real urban canopy. *Boundary-Layer Meteorology*.
- BECKETT, K.P., FREER-SMITH, P.H., & TAYLOR, G., 2012. The capture of particulate pollution by trees at five contrasting urban sites. *Arboricultural Journal*, 24, 2-3, 209-230.
- BEELEN, R., STAFOGGIA, M., RAASCHOU-NIELSEN, O., ANDERSEN, Z.J., XUN, W.W., KATSOUYANNI, DIMAKOPOULOU, K., BRUNEKREEF, B., WEINMAYR, G., & HOFFMANN, B., 2014. Long-term exposure to air pollution and cardiovascular mortality: an analysis of 22 European cohorts. *Epidemiology*, 25, 368-378.
- BELL, M.L., ZANOBETTI, A., & DOMINICI, F., 2013. Evidence on vulnerability and susceptibility to health risks associated with short-term exposure to particulate matter: a systematic review and meta-analysis. *American Journal of Epidemiology*, 143-149.
- BRANTLEY, H.L., HAGLER, G.S.W., DESHMUKH, J., & BALDAUF, R.W., 2014. Field assessment of the effects of roadside vegetation on near-road black carbon and particulate matter. *Science of the Total Environment*, 468-469, 120-129.

- BRITTER, R. E., & HANNA, S. R., 2003. Flow and dispersion in urban areas. *Annual review of fluid mechanics*, 35(1), 469-496.
- BUCCOLIERI, R., SALIZZONI, P., SOULHAC, L., GARBERO, V., & DI SABATINO, S., 2015. The breathability of compact cities. *Urban Climates*, 13,73-93.
- CAMPBELL, J. L., RUSTAD, L. E., PORTER, J. H., TAYLOR, J. R., DERESZYNSKI, E. W., SHANLEY, J. B., GRIES, C., HENSHAW, D. L., MARTIN, M. E., SHELDON, W. M. & BOOSE, E. R., 2013. Quantity is Nothing without Quality: Automated QA/QC for Streaming Environmental Sensor Data. *BioScience*, 63, 574-585.
- CAMPRODON, G., BARBERÁN, V., GONZÁLEZ, O. & SMÁRI, V. 2019. iSCAPE environmental sensing platform documentation (Version v1.0). Zenodo.
- CHENG, W. C., LIU, C. H., & LEUNG D. Y. C., 2009. On the comparison of the ventilation performance of street canyons of different aspect ratios and Richardson number. *Building Environment*, 2(1), 53-61.
- DI BERNARDINO, A., MONTI, P., LEUZZI, G., & QUERZOLI, G., 2018. Pollutant fluxes in two-dimensional street canyons. *Urban Climates*, 24, 80-93.
- EEA (European Environment Agency), 2017. EMEP/EEA air pollutant emission inventory guidebook 2016. Last update June 2017.
- ENVI-met, version 4. <http://www.envi-met.com> (last accessed on 27/03/2019)
- Finnish Science Centre HEUREKA. <https://www.heureka.fi/?lang=en> (last accessed on 27/03/2019)
- GALLAGHER, J., GILL, L. W., & MCNABOLA, A., 2012. Numerical modelling of the passive control of air pollution in asymmetrical urban street canyons using refined mesh discretization schemes. *Building and Environment*, 56, 232-240, doi:10.1016/j.buildenv.2012.03.013
- GONZÁLEZ, L.T., LONGORIA RODRÍGUEZ, F.E., SÁNCHEZ-DOMÍNGUEZ, M., CAVAZOS, A., LEYVA- PORRAS, C., SILVA-VIDAURRI, L.G., ASKAR, K.A., KHARISOV, B.I., VILLARREAL CHIU, J.F., & ALFARO BARBOSA, J.M., 2017. Determination of trace metals in TSP and PM2.5 materials collected in the Metropolitan Area of Monterrey, Mexico: a characterization study by XPS, ICP-AES and SEM-EDS. *Atmos. Res.* 196, 8–22.
- GRIMMOND, C. S. B., & OKE, T. R., 2002. Turbulent heat fluxes in urban areas: Observations and a local-scale urban meteorological parameterization scheme (LUMPS). *Journal of Applied Meteorology*, 41(1), 792-810.
- HAGLER, G.S.W., YELVERTON, T.L.B., VEDANTHAM, R., HANSEN, A.D.A., & TURNER, J.R., 2011. Post- processing method to reduce noise while preserving high time resolution in aethalometer real-time black carbon data. *Aerosol and Air Quality Research*, 11, 539–546.
- HAGLER, G.S.W., LIN, M.Y., KHLYSTOV, A., BALDAUF, R.W., ISAKOV, V., FAIRCLOTH, J., & JACKSON, L.E., 2012. Field investigation of roadside vegetative and structural barrier impact on near-road ultrafine particle concentrations under a variety of wind conditions. *Science of the Total Environment*, 419, 7–15.
- HAYS, M.D., CHO, S.H., BALDAUF, R., SCHAUER, J.J., & SHAFER, M., 2011. Particle size distributions of metal and non-metal elements in an urban near-highway environment. *Atmospheric Environment*, 45, 925–934.



- HUTTNER, S. & BRUSE, M., 2009. Numerical modelling of the urban climate - A preview on ENVI-met 4.0. Presented at: The seventh International Conference on Urban Climate, 29 June – 3 July 2009, Yokohama, Japan. Available online at: [http://www.envi-met.net/documents/papers/ICUC7\\_ModellingV4.pdf](http://www.envi-met.net/documents/papers/ICUC7_ModellingV4.pdf) (last accessed 27/03/2019)
- JANCSEK-TURÓCZI, B., HOFFER, A., NYÍRÖ-KÓSA, I., & GELENCSE, A., 2013. Sampling and characterization of resuspended and respirable road dust. *Journal of Aerosol Science*, 65, 69–76.
- JUNNINEN, H., NISKA, H., TUPPURAINEN, K., RUUSKANEN, J. & KOLEHMAINEN, M. 2004. Methods for imputation of missing values in air quality data sets. *Atmospheric Environment*, 38, 2895-2907.
- KELLNEROVA, R., FUKA, V., KUKACKA, L., URUBA, V., & JANOUR, Z., 2013. On the quadrant analysis of the flow in the street canyon. In: EPJ Web of Conferences Vol. 45, p. 01132. EDP Science.
- KILLICK, R., FEARNHEAD, P. & ECKLEY, I. A. 2012. Optimal Detection of Changepoints With a Linear Computational Cost. *Journal of the American Statistical Association*, 107, 1590-1598.
- KING, E. A., MURPHY, E. & McNABOLA, A., 2009. Reducing pedestrian exposure to environmental pollutants: A combined noise exposure and air pollution analysis approach. *Transportation Research Part D: Transport and Environment*, 14, 309-316
- KUBILAY, A., NEOPHYTOU, M. K.-A., MATSENTIDES, S., LOIZOU, M., & CARMELIET, J., 2017. The pollutant removal capacity of an urban street canyon and its link to the breathability and exchange velocity. *Procedia Engineering* 180, 443-451.
- KUMAR, P., MORAWSKA, L., MARTANI, C., BISKOS, G., NEOPHYTOU, M., DI SABATINO, S., BELL, M., NORFORD, L. & BRITTER, R. 2015. The rise of low-cost sensing for managing air pollution in cities. *Environment International*, 75, 199-205.
- JANHÄLL, S., 2015. Review on urban vegetation and particle air pollution – Deposition and dispersion. *Atmospheric Environment*, 105, 130-137.
- LIN, M.Y., HAGLER, G., BALDAUF, R., ISAKOV, V., LIN, H.Y., KHLYSTOV, A., 2016. The effects of vegetation barriers on near-road ultrafine particle number and carbon monoxide concentrations. *Science of the Total Environment*, 553, 372–379.
- LIU, C. H. & WONG, C. C., 2014. On the pollutant removal, dispersion, and entrainment over two-dimensional idealized street canyons. *Atmospheric Environment*, 135, 128-142.
- MAZZIOTTI TAGLIANI, S., CARNEVALE, M., ARMIENTO, G., MONTEREALI, M.R., NARDI, E., INGLESSIS, M., SACCO, F., PALLESCHI, S., ROSSI, B., SILVESTRONI, L., & GIANFAGNA, A., 2017. Content, mineral allocation and leaching behavior of heavy metals in urban PM<sub>2.5</sub>. *Atmospheric Environment* 153, 47–60.
- MCMILLEN, R., 1988. An eddy correlation technique with extended applicability to non-simple terrain. *Boundary-Layer Meteorology*, 43(3), 231-245.
- MCNABOLA, A., BRODERICK, B. M., & GILL, L. W., 2008. Reduced exposure to air pollution on the boardwalk in Dublin, Ireland. Measurement and prediction. *Environment International*, 34, 86-93, doi:10.1016/j.envint.2007.07.006
- MCNABOLA, A., BRODERICK, B. M., & GILL, L. W., 2009. A numerical investigation of the impact of low boundary walls on pedestrian exposure to air pollutants in urban street canyons. *Science of the Total Environment*, 407, 760-769, doi:10.1016/j.scitotenv.2008.09.036



- MORENO, T., MARTINS, V., QUEROL, X., JONES, T., BÉRUBÉ, K., MINGUILLÓN, M.C., AMATO, F., CAPDEVILA, M., DE MIGUEL, E., CENTELLES, S., & GIBBONS, W., 2015. A new look at inhal- able metalliferous airborne particles on rail subway platforms. *Science of the Total Environment*, 505, 367–375.
- NOWAK, D.J., CRANE, D.E., & STEVENS, J.C., 2006. Air pollution removal by urban trees and shrubs in the United States. *Urban Forestry & Urban Greening*, 4, 3-4, 15-123.
- OKE, T. R., 1997, Urban environments, in W. G. Bailey, T. R. Oke and W. R. Rouse (eds), *The Surface Climates of Canada*, McGill-Queen's University Press, Montréal, 303–327.
- OTTOSEN, T. B., KETZEL, M., SKOV, H., HERTEL, O., BRANDT, J. & KAKOSIMOS, K. E., 2016. A parameter estimation and identifiability analysis methodology applied to a street canyon air pollution model. *Environmental Modelling and Software*, 84.
- OTTOSEN, T.-B. & KUMAR, P., 2019. Outlier detection and gap filling methodologies for low-cost air quality measurements. *Environmental Science: Processes & Impacts*.
- PANDA, S., SHIVA NAGENDRA, S.M., 2018. Chemical and morphological characterization of respirable suspended particulate matter (PM10) and associated health risk at a criti- cally polluted industrial cluster. *Atmospheric Pollution Research*, 1–13.
- PIRINGER, M., GRIMMOND, C. S. B., JOFFRE, S. M., MESTAYER, P., MIDDLETON, D. R., ROTACH, M. W., BAKLANOV, A., DE RIDDER, K., FERREIRA, J., GUILLOTEAU, E., KARPPINEN, A., MARTILLI, A., MASSON, V., & TOMBROU, M., 2002. Investigating the surface energy balance in urban areas—recent advances and future needs. *Water, Air and Soil Pollution: Focus*, 2(5-6), 1-16.
- ROTACH, M.W., VOGT, R., BERNHOFER, C., BATCHVAROVA, E., CHRISTEN, A., CLAPPIER, A., FEDDERSEN, B., GRYNING S. E., MARTUCCI, G., MAYER, H., MITEV, V., OKE, T. R., PARLOW, E., RICHNER, H., ROTH, M., ROULET, Y. A., RUFFIEUX, D., SALMOND, J.A., SCHATZMANN M., & VOOGT, J. A., 2005. BUBBLE-an urban boundary layer meteorology project. *Theoretical and Applied Climatology*, 81(3-4), 231-261
- SHANG, Y., SUN, Z., CAO, J., WANG, X., ZHONG, L., BI, X., LI, H., LIU, W., ZHU, T., & HUANG, W., 2013. Systematic review of Chinese studies of short-term exposures to air pollution and daily mortality. *Environment International*, 54, 100-111.
- STULL, R. B., 1988. *An introduction to boundary layer meteorology*. Springer Netherlands, Kluwer Academic Publishers, ISBN: 978-9027727688, 670 pp
- VAN ZOEST, V. M., STEIN, A. & HOEK, G., 2018. Outlier Detection in Urban Air Quality Sensor Networks. *Water, Air, & Soil Pollution*, 229, 111.
- VELASCO, E. & TAN, S. H. 2016. Particles exposure while sitting at bus stops of hot and humid Singapore. *Atmospheric Environment*, 142, 251-263.
- WANG., M., BEELEN, R., STAFOGGIA, M., RAASCOU-NIELSEN, O., ANDERSEN, Z.J., HOFFMANN, B., FISCHER, P., HOUTHUIJIS, D., NIEUWENHUIJSEN, M., & WEINMAYR, G., 2014. Long-term exposure to elemental constituents of particulate matter and cardiovascular mortality in 19 European cohorts: results from the ESCAPE and TRANSFORMS projects. *Environment International*, 66, 97-106.
- WEERAKKODY, U., DOVER, J.W., MITCHELL, P., & REILING, K., 2018. Quantification of the traffic- generated particulate matter capture by plant species in a living wall and evaluation of the important leaf characteristics. *Science of the Total Environment*, 635, 1012–1024.
- WILLMARTH, W.W., 1975. Structure of turbulence in boundary layers. *Advances in Applied Mechanics*, 15, 159–254.